Radiation Effects in Interfaces and Thin Films

By

Alexander Mairov

A dissertation submitted in partial fulfillment of the requirements for the degree of

Doctor of Philosophy

(Nuclear Engineering and Engineering Physics)

at the

UNIVERSITY OF WISCONSIN-MADISON

2016

Date of Final Oral Examination: 11/16/2016

The dissertation is approved by the following members of the Final Oral Committee:

Kumar Sridharan, Distinguished Research Professor, Engineering Physics
Todd Allen, Associate Professor, Engineering Physics
Michael Corradini, Professor, Engineering Physics
James P. Blanchard, Professor, Engineering Physics
Chang Beom Eom, Professor, Materials Science and Engineering

ACKNOWLEDGEMENTS

This work has been completed using funding received from the DOE Office of Nuclear Energy's University Programs (NEUP), and was partly completed using the facilities of the Microscopy and Characterization Suite at the Center for Advanced Energy Studies located in Idaho Falls, the irradiation facility of the Environmental and Molecular Sciences Laboratory (EMSL) in the Pacific Northwest National Laboratory (PNNL) located in Pasco, WA. I would like also to acknowledge instrument support by the UW MRSEC (DMR-1121288) and the UW NSEC (DMR-0832760).

I would like to thank my thesis committee for their help and support, Dr. Todd Allen for his initial support and scientific discussion and Dr. Kumar Sridharan for his constant support during this long journey.

I would like to thank some of my colleagues/friends from work: Kevin, Janne, Jianchao, Lingfeng, and Alex Kvit for fruitful discussions and help with mastering some TEM techniques. A special thanks to Yina and Vahid for their help with whatever I needed: more than colleagues they are true friends. Finally special thanks also to Fabio and especially Francisco: he is a truly successful scientist and we’ve done a great work together on Al_2O_3 coatings.

This PhD has really been a hack of a life experience. In the downs and hills that characterize the life of every PhD student, I met so many people that marked my life in so many ways -good or bad- it would be impossible to acknowledge them all. Just some few honorable mentions: Giacomino, Giulio, Riccardo, Francesco, Davide, Stefano, Salih, Alvaro, Rebecca, Lucas, Diego, Kushal, Juliana, Diogo, Vahid, Yina, Mike, Fays and above all Julia, who constantly supported me and stayed by my side in the toughest times of this journey. Finally, I want to thank my wonderful family, Lina, Aharon, Elena, Maximilian and Carolina, whom are always in my mind.

Abstract and Executive Summary

The goal of this research is to advance the fundamental understanding of the stability of interfaces and thin films under radiation for materials' systems of interest to advanced nuclear reactor concepts. This is becoming an increasingly important area of research given that the materials for these reactors will be expected to operate to higher levels of radiation, at higher temperature, and in more corrosive coolants than light water reactors. Interfaces in materials act as sinks for point defects created during radiation, and one of the key strategies to imparting higher radiation damage tolerance is to increase the areal fraction of internal interfaces in materials. Work on nanograined materials, nanoscale multilayered materials, and oxide dispersion strengthened (ODS) steels has demonstrated the efficacy of this approach. Another significant challenge in advanced reactors is corrosion of materials in the high temperature coolant environments of these reactors. Given the limited number of ASME code certified alloys available for immediate use, thin films and coatings may have to be increasingly relied upon for providing corrosion resistance to these alloys. Here again, it is important to study the radiation damage effects on the thin films and thin film/substrate interfaces.

Based on the aforementioned challenges, this research investigates high temperature irradiation-induced phase transformations in thin films and thin film/substrate interfaces, accumulation of helium bubbles at interfaces, and structure-property relationships in irradiated nanoceramic thin films. Work on thin film/substrate interface irradiation effects was initiated with studies on Fe-12%Cr model binary alloy substrate coated with thin films of Ti and TiO_2. Irradiation was shown to have a more pronounced effect for Ti compared to TiO_2 in terms of spatial extent of mixing with the substrate. For the TiO_2 thin film system, the stoichiometry under irradiation shifted to a more oxygen deficient phase which influenced the diffusion profile of chromium from the substrate into the oxide film. For the Fe-12%Cr model alloy substrate coated with thin films of Y_2O_3 investigated next, chromium was observed to diffuse to the metal oxide interface at high temperatures, and radiation caused the formation of an extended amorphous layer at the metal oxide interface. The thin film materials in these studies also constitute the composition of nanoscale oxide particles in ODS steels and nanostructured ferritic alloys (NFAs). Thus, these studies provided fundamental understanding on irradiation stability of interfaces in nanoscale oxide precipitates in ODS steels (and NFAs) which would otherwise be extremely challenging due to the fine size scale of these precipitate particles.

Another important challenge in advanced reactor concepts is the generation of helium transmutation product at high temperatures and radiation doses. This helium can accumulate as bubbles at high angle grain boundaries and cause severe embrittlement. Here again engineered interfaces in materials can be beneficial by way of becoming sites for helium accumulation and in effect diverting it from high angle grain boundaries where it can be detrimental to the mechanical properties. In this research a set of experiments was designed specifically to study the nucleation of helium bubbles at metal/oxide interfaces. To this end, Y_2O_3/Fe interfaces with different crystallographic orientations were synthesized and implanted with helium ions at room temperature. Results from these experiments clearly showed bubble nucleation and growth at semi-coherent and incoherent metal/oxide interfaces. Bubbles nucleated at random locations at the metal/oxide interface and were not in correspondence of misfit dislocations, which theoretical simulations predict to be preferential nucleation sites. Statistical analyses of bubble

size clearly showed that bubbles nucleating at the interface were significantly larger in size than those growing in the individual layers. Moreover, all of the bubbles imaged at the interface were located on the oxide side of the interface and only “wetted” a small area of the interface. In contrast, bubbles nucleating at gran boundaries in the iron layer were observed to symmetrically overlap across the boundaries, revealing the different character of metal/metal and metal/oxide interfaces.

Finally, the radiation effects (up to 150dpa) in nanoceramic Al_2O_3 thin films were investigated with the goal of correlating the effect of structural changes to mechanical property changes. The as-deposited film was amorphous (with a small fraction of nanocrystalline islands). At lower dpas, irradiation induced an amorphous-to-crystalline transformation resulting in a fully nano-grained structure, while extended irradiations induced grain growth and softening of the material in accordance with the Hall-Petch relationship. This softening is beneficial as radiation hardening (and associated embrittlement) is a concern in many materials. The ratio of hardness to Young’s modulus (H/E) increased with radiation dose which also suggests a potential improvement in the fracture toughness in radiation environment. The crystalline-to-amorphous transition leads to new energy dissipation mechanisms available upon impact loading, such as lattice plasticity and localized amorphization, as conclusively demonstrated by high resolution TEM. These transformations also suggest self-healing qualities of the nanoceramic Al_2O_3 thin films.

The research also provided a platform for on-site experimental collaborations with Pacific Northwest National Laboratory (PNNL), Idaho National Laboratory (INL), University of California, Berkeley (UCB), and the Istituto Italiano di Tecnologia (IIT), Milan, Italy.

TABLE OF CONTENTS

LIST OF FIGURES

LIST OF TABLES

LIST OF ABBREVIATIONS

ADF	Annular Dark Field
AFM	Atomic Force Microscopy
Al	Aluminum
Al_2O_3	Aluminum Oxide
APT	Atom Probe Tomography
ATR	Advanced Test Reactor
Au	Gold
BCC	Body Centered Cubic
BL	Bonding Layer
C	Carbon
C-TEM	Conventional TEM
CAES	Centre for Advanced Energy Studies
CBM	Critical Bubble Model
Cr	Chromium
Cs	Spherical Aberration
CTE	Coefficient of Thermal Expansion
DFT	Density Functional Theory
DOE	Department of Energy
DP	Diffraction Pattern
E	Young Modulus
EDS	Energy Dispersive Spectroscopy
EELS	Electron Energy Loss Spectroscopy
EMSL	Environmental Molecular Sciences Laboratory
FCC	Face Centered Cubic
Fe	Iron
FFT	Fast Fourier Transform
FIB	Focused Ion Beam
FM - growth mode	Frank–van der
GB	Grain Boundaries
GFR	Gas Fast Reactor
GIF	Generation IV International Forum

H	Hardness
HAADF	High Angle Annular Dark Field
He	Helium
HR	High Resolution
IBM	Ion Beam Mixing
iFFT	Inverse Fourier Transform
IIT	Istituto Italiano di Tecnologia
INL	Idaho National Laboratory
LEAP	Local Electrode Atom Probe
LFR	Lead Fast Reactor
LWR	Light Water Reactor
MBE	Molecular Beam Epitaxy
MD	Molecular Dynamics
MDs	Misfit Dislocations
MSC	Materials Science Center
MSR	Molten Salt Reactor
NEC	National Electrostatics Corporation
NFA	Nanostructured Ferritic Alloy
O	Oxygen
ODS	Oxide Dispersion Strengthen
ORs	Orientation Relationships
PIE	Post-Irradiation Examination
PKA	Primary Knock on Atom
PLD	Pulsed Laser Deposition
PNNL	Pacific Northwest National Laboratory
Pt	Platinum
RED	Radiation Enhanced Diffusion
RHEED	Reflection High Energy Electron Diffraction
RIS	Radiation Induced Segregation
SADP	Selected Area Diffraction Pattern
SCWR	Super-Critical Water Reactor
SEM	Scanning Electron Microscope
SFR	Sodium Fast Reactor
SIA	Self-Interstitial Atom
SiC	Silicon Carbide
SRIM	Stopping Range of Ion in Matter
STEM	Scanning Transmission Electron Microscope
T	Temperature
TBC	Thermal Barrier Coatings
TEM	Transmission Electron Microscope
Ti	Titanium
TIA	TEM Imaging and Analysis (software)
TiO_2	Titanium Dioxide
UHV	Ultra-High Vacuum
UW-Madison	University of Wisconsin-Madison
VHTR	Very-High Temperature Reactor

VW - growth mode	Volmer–Weber
XRD	X-Ray Diffraction
Y_2O_3	Yttrium Oxide
YSZ	Yttria Stabilized Zirconia
Z	Mean Atomic Number

CHAPTER 1

Introduction and Background

1.1 Introduction

The United Nations has estimated that the world population will grow to about 9.6 billion in 2050 [1], with a concomitant increase in global energy demand coupled to an increase of the living standards in developing countries [2]. With fossil fuels still largely dominating energy production and consumption (67% of the total energy produced in the US in 2014 came from fossil fuels) concerns regarding global warming from CO_2 emissions have been raised by the scientific community [3]. In this context, a decisive role can be played by nuclear energy - in the words of leading climate researchers, “there is no credible path to climate stabilization that does not include… nuclear power” [4]. Among the most attractive features of fission nuclear reactors is the high power densities of about 50-75 $MWthm^{-3}$, which is nearly two orders of magnitude higher than the average power density in the boiler furnace of a large-scale coal power plant [5] and of course, the low CO_2 emission [6]. However, the controversial aspects of nuclear energy such as nuclear proliferation, radioactive waste management and storage and accident scenarios, still continue to shadow most of its appealing features in the eyes of the society.

To address the aforementioned issues the United States Department of Energy (DOE) and the Generation IV (Gen IV) International Forum (GIF) identified six advanced fission reactor concepts as potential next-generation (Generation IV) nuclear power systems [7,8]. These concepts were selected from hundreds of ideas submitted to the US-DOE by scientists and engineers world-wide, during the first phase of the Gen IV program in 2002 [7]. The six concepts finally selected by the GIF for further investigation and development were supercritical water-cooled reactor (SCWR), sodium fast reactor (SFR), lead fast reactor (LFR), very-high-temperature reactor (VHTR), gas fast reactor (GFR) and molten salt reactor (MSR). It is anticipated that these next generation nuclear reactor systems will outperform current generation nuclear reactors (light water reactors, LWR) in the critical areas of non-proliferation, fuel cycle efficiency, radioactive waste management, and safety. However, these new reactor concepts will impose significantly higher demands on materials that will be used for their constructions in regards to temperature, radiation fields, and corrosion due to the coolant environment.

Figure 1-1 shows the expected temperature and radiation damage levels, expressed in dpa[1], for the six Gen IV concepts. Operational temperature and radiation damage levels of current nuclear reactors (Gen II and Gen III) are also shown for reference. As can be seen from this figure, materials for Gen IV reactors will be expected to operate in high temperature and high radiation dose regimes and over long periods of time [9]. To allow operation at high temperatures (i.e. in the range 400°C-1000°C) coolants other than water will be utilized – namely, supercritical water, high temperature helium gas, molten salts or liquid metals like sodium, lead, and lead-bismuth eutectic alloy. These coolants can be very corrosive to the materials used for in-core components, and their corrosive effects are augmented by radiation damage and high temperature [10]. Even in LWR high temperatures (i.e. exceeding 1000°C) can be reached during severe accident conditions, and advanced materials concepts are being

---

[1] dpa is the accepted unit of radiation damage, and expresses the average number of times that each atom in the material has been knocked out of its lattice position due to radiation from neutrons or charged particles

investigated (surface modification and/or replacement of zirconium-alloy cladding) to avoid 2011 Fukushima-Daiichi type accidents.

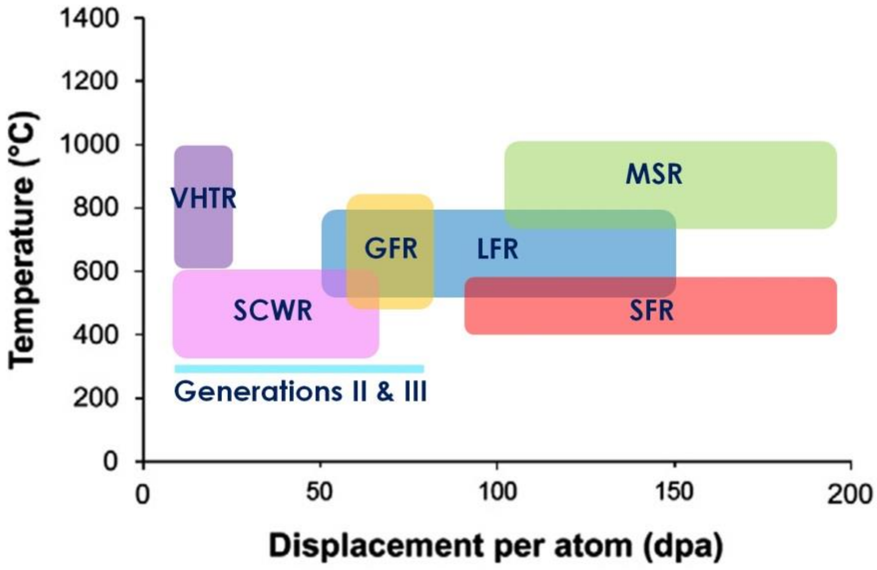

Figure 1-1: Temperature and dose regimes for in core structural components of the six proposed Gen IV advanced reactor concepts. Gen II represents current LWR (adapted from Ref. [11]).

The aggressive conditions imposed in the Gen IV concepts compared to currently operating LWR will exacerbate all the potential failure mechanisms in engineering materials and systems (e.g., thermal creep, fatigue, irradiation-induced radiation, void swelling, high-temperature helium embrittlement) [5,12,13]. Therefore, the successful fruition of advanced Gen IV nuclear systems is inextricably related to the development of materials that can withstand their aggressive operating conditions. Since radiation damage is rather unique to nuclear reactor applications (as opposed to, for example, aerospace and other energy systems), it is reasonable to argue that the quest for high-performance materials should be, at the first level, driven by the requirement of radiation tolerance in intense neutron radiation fields. One fundamental limitation here has been that the face centered cubic (FCC) austenitic alloys which are known for their high temperature strength swell significantly in high radiation environments. This has largely precluded the use of high temperature resistant Ni-based alloys or cobalt-containing alloys (the latter mainly for radioactivity reasons), and to a great extent limited the use of metallic alloys to body centered cubic (BCC) ferritic steels which swell less, but have lower high temperature strength. Ceramic materials, on account of their inherent brittleness, can be used as structural materials only in their composite forms. In this regards, SiC-SiC and C-C composites are gaining favor, but much investigation is needed for these composites, particularly in the areas of large-scale manufacturability and joining.

Several approaches are being investigated to develop radiation damage tolerant materials. One approach that is showing considerable promise is to increase the amount of internal interfaces in materials. Interfaces are known to act as sites for recombination of defects and sinks for helium produced under irradiation. One of the most interesting advances in this area has been oxide dispersion strengthened (ODS) steel and nanostructured ferritic alloys (NFA) where a fine dispersion of nanometer scale oxide particles in a ferritic matrix, have been shown to impart superior radiation resistance in addition to creep strength. The particle-matrix (metal/oxide) interfaces act as sinks for radiation generated point defects and also as a nucleation sites for bubbles of helium. Dispersing helium as a larger number of smaller bubbles can limit the amount of helium forming bubbles at grain boundaries. A fundamental understanding of the physical and compositional stability of these interfaces as well as interfacial effects under radiation is of utmost importance for predicting the in-service behavior of these alloys.

1.2 Thesis Objectives

The goal of this research is to advance the fundamental understanding of the radiation response of interfaces and thin films in the context of nuclear materials. To this end, this work has focused on the synthesis, heavy ion irradiation, and structural characterization of interfaces and thin films of materials of interest to Gen IV reactors such as, Ti, Y, TiO_2 and Y_2O_3 thin films on ferritic steel substrates (to simulate matrix and nanoparticles in ODS steels), and novel Al_2O_3 nanostructured ceramic films with immediate potential applications as coatings for corrosion protection in many of the harsh high temperature Gen IV reactor environments.

The stability of oxide nanoparticles in ODS steel under radiation depends on the physical and compositional stability of their interfaces with the surrounding matrix. Knowledge of the interface stability is therefore crucially important to determine the applicability of these alloys as in-core materials for Gen IV nuclear reactors. However, the metal/oxide interface is often challenging to study in great detail because the interfacial reactions are complicated in their chemistry and can occur at sub-nanometer length scales [14]. Therefore, the study of the stability of such interfaces was performed by synthesis of model interfaces by the use of thin film deposition techniques. This approach is advantageous as it allows working with an emulation of the actual interfaces on a larger length scale and with a controlled, simplified but realistic chemistry. As the small particles in ODS steels are typically (Y,Ti)-oxide surrounded by a ferritic steel matrix, bi-layered systems of these constituents were prepared by depositing thin films (~270 nm) of titanium, titanium-dioxide (TiO_2) and yttrium-oxide (Y_2O_3) on a Fe-12%Cr binary ferritic alloy. These thin film-substrate systems were used to evaluate chemical intermixing between the film material and the ferritic alloy substrate after irradiation with 5 MeV Ni^{++} ions at 300°C, 500°C, and 700°C. These experiments were also useful in evaluating the irradiation stability of the films themselves – for example, titanium-oxide (deposited as TiO_2) at high temperature transformed to oxygen-deficient TiO_{2-x} which in turn promoted chromium diffusion from the substrate into the film. Other interface-related phenomena accruing from irradiation were also observed and investigated in detail.

Helium bubble nucleation in materials at high temperatures and radiation doses is a concern as these bubbles can migrate to grain boundaries and cause decohesion of the boundaries, material embrittlement, and swelling. Once again, the presence of engineered interfaces in the material can be beneficial as they can act as preferential sites for helium bubble nucleation and migration, thereby minimizing and preventing them from accumulating at grain boundaries where they can be detrimental to the properties. In the case of ODS steels for example, it is hypothesized that the interfaces between the nanoscale oxide particles and the matrix could act as "trapping sites" for such helium bubbles and retard embrittlement and swelling. Differently oriented interfaces are expected to possess different interfacial energies which dictate the efficacy of interfaces as sinks for radiation-induced defects and helium. This hypothesis has been tested in this research by synthesizing nanoscale bi-layered systems consisting of Y_2O_3 and Fe films for controlled experimental study. Epitaxial and non-epitaxial Y_2O_3/Fe interfaces were created on single crystal substrates of yttria-stabilized zirconia (YSZ) oriented along the <100>, the <110> and the <111> directions. Once these model systems were synthesized, they were irradiated with helium ions at room temperature and the nucleation of bubbles was studied using transmission electron microscopy (TEM) and high resolution scanning transmission electron microscopy HR-STEM.

The radiation effects observed in interfaces and thin films led to the study of the radiation damage response of Al_2O_3 thin film, deposited at room temperature by Pulsed Laser Deposition

(PLD) [15]. The film was a fully dense, metastable film of alumina with a homogeneous dispersion of a low volume fraction of randomly oriented nanocrystalline Al_2O_3 domains in an amorphous Al_2O_3 matrix. The response of this nanostructured thin film was evaluated after heavy ion irradiation (up to 150dpa) at high temperature, and the microstructural changes induced by the radiation were correlated to changes observed in the mechanical properties. Irradiation led to the complete crystallization of the amorphous/crystalline Al_2O_3 film with grain growth occurring monotonically with radiation dose. Mechanical properties measured by nanoindentation technique showed that upon irradiation the hardness first increases and then decreases according to the Hall-Petch relationship, indicating that the normally embrittling effect of radiation may be offset by the softening effect of increasing grain size. The improvement seems to be manifest in the onset of such energy dissipation mechanisms as twinning (during grain growth), lattice plasticity and localized crystalline-to-amorphous transformations (under impact loading). These energy dissipation mechanisms are present at both extremes of the damage levels studied.

CHAPTER 2

Radiation Effects on Materials

2.1 Overview of Theory of Radiation Damage

The core of a nuclear reactor is an exceptionally aggressive environment, where materials are exposed to intense radiation fields at high temperatures and corrosive coolant environments for extended periods of time at varying levels of stresses [16]. When exposed to radiation in the nuclear reactor, materials undergo damage at an atomic level caused by the transfer of kinetic energy of an incident particle and its redistribution to the atoms within the material. The radiation damage process is composed of many events [12], which are briefly outlined below:

1. Collision of the incident particle with a lattice atom
2. Transfer of kinetic energy to the lattice atom resulting in the Primary Knock on Atom (PKA)
3. Displacement of the atom from its lattice site
4. Transfer of the PKA energy to other atoms of the lattice
5. Production of a displacement cascade

As the PKA travels into the material it usually interacts with several other atoms, displacing them from their respective lattice sites. These displaced atoms in turn will displace other atoms and if this sequence continues, a so called collision cascade is created [13]. The result of the processes described above is the creation of a collection of point defects (interstitials and vacancies) which survive in the lattice. It is worth noting that only a fraction of the created defects will survive in the material. For example, in BCC iron this fraction is only about 30% [17].

To develop a simple model that will describe the evolution and sustenance of the radiation-induced defects, the approach developed in reference [16] is outlined below. A simple expression for the rate of defect annihilation and accumulation at sinks is given by:

$$r = D_{i,v} X_{i,v} Z_{ti/v} \qquad \text{Equation 2-1}$$

where $D_{i,v}$ is the diffusion coefficient of the vacancy/interstitial, $X_{i,v}$ is the atomic vacancy/interstitial defect fraction and $Z_{ti/v}$ is the total defect strength for vacancy/interstitial. Point defect sinks are typically dislocations Z_d, interfaces (e.g., grain boundary) Z_i, and cavities (either bubbles or voids) Z_c. The individual sink strengths are derived by solving the diffusion equation. It must be noted that biases for defect-sink interactions do exist - for example self-interstitials atoms (SIA) preferentially annihilate at dislocations owing to long-range strain field interactions. This bias causes the net irradiation-induced vacancy flux, $J_v = {(D_v X_v - D_i X_i - D_{sd})}\big/{\Omega_a l}$, to be generally positive (Ω_a is the atomic volume and l is a length gradient associated with a specified sink). Excess defects and solute fluxes can typically cause:

- Voids swelling when $(D_v X_v - D_i X_i - D_{sd}) Z_{vv}$ is positive at unbiased void sinks.
- Growing interstitial dislocation loops, dislocation climb, and overall evolution of the dislocation structure when $(D_v X_v - D_i X_i - D_{sd}) Z_{di}$ is positive, resulting from the dislocation bias for SIA. The loop structures typically saturate at high doses and can evolve into network dislocations.

- Radiation-enhanced diffusion (RED) and radiation-enhanced precipitation (REP) of substitutional solutes due to $D_v X_v \gg D_{sd}$.
- Radiation-induced solute segregation (RIS) and radiation-induced precipitation (RIP) of non-equilibrium phases in solute-enriched regions.

Figure 2-1 illustrates some scenarios of defect creation and evolution.

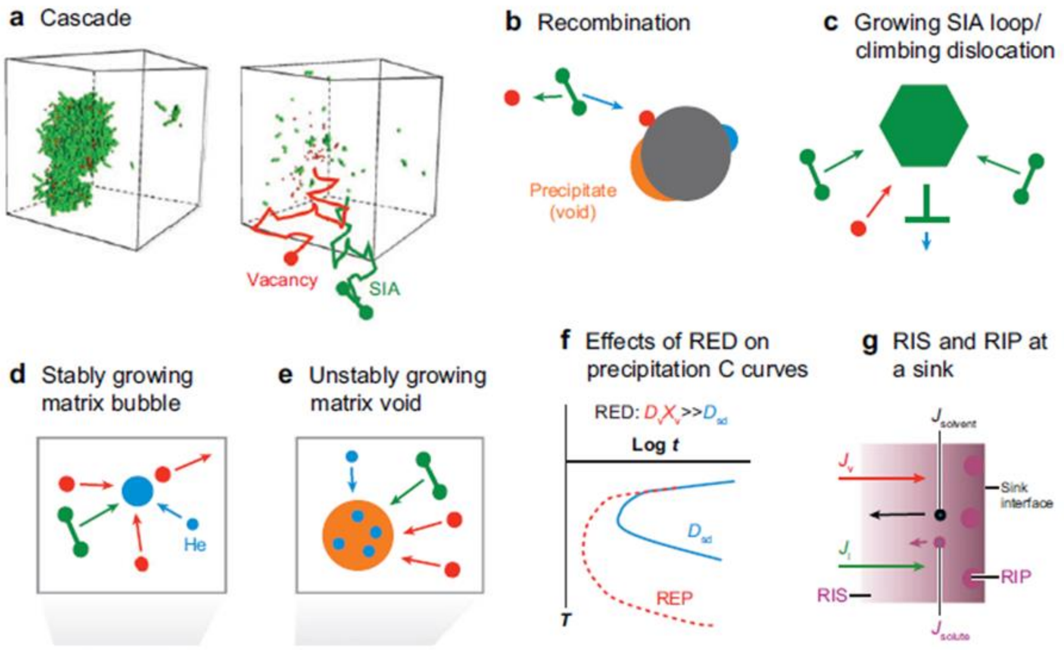

Figure 2-1: Schematic illustration of mechanisms of radiation-induced defects in materials after (a) production of vacancies and SIA, (b) SIA recombination with diffusing and trapped vacancies, (c) growth of SIA loops and climb of edge dislocations due to a bias-driven excess flux of SIA, (d) annihilation of defects at bubbles that grow in a stable manner with the addition of He, (e) excess flux of vacancies producing unstable growth of voids due to dislocation SIA bias, (f) time -temperature curves schematically illustrating the effects of radiation-enhanced diffusion (RED) on radiation-enhanced precipitation (REP) kinetics (g) radiation-induced solute segregation (RIS) due to the inverse Kirkendall effect leading to radiation-induced precipitation (RIP) in solute-enriched regions near sinks (adapted from Ref. [16]).

To evaluate the response of a material to radiation damage due to neutrons, irradiation experiments in a nuclear reactor (or a test reactor) has to be performed. These experiments, though extremely valuable (and required before introduction of a material into a reactor), are time consuming, expensive and induce residual radioactivity in the test samples which requires long cool-down periods before post-irradiation examinations (PIE) can be performed. Most of these limitations can be overcome by using charged particle irradiation as surrogate to neutron irradiation. A characteristic advantage of charged-particle irradiation experiments is precise and individual control over most of the important irradiation conditions such as dose, dose rate, and temperature. Additional benefits are the absence (or very low) induced radioactivity of the samples and a greatly reduced irradiation time of a few hours to days vs. years for neutron irradiation to achieve equivalent microstructural damage levels. An acknowledged limitation of charged particle irradiation is that the irradiated depths are quite small (fractions of a micron to a few tens of microns depending on irradiation species and energy), requiring sophisticated electron microscopy techniques for examination of radiation damage.

More fundamentally, atomic displacements caused from charged particles are different from those caused by neutrons. Charged particles, while travelling into the material, lose energy not only by elastic collisions but also by electronic excitation. Radiation damage in this case can be quantified by solving the damage rate equation:

$$R_D = N \int_{\check{E}}^{\hat{E}} \phi(E_i) \sigma_D(E_i) dE_i \qquad \text{Equation 2-2}$$

where N is the lattice atom density, $\phi(E_i)$ is the energy dependent particle flux, and $\sigma_D(E_i)$ is the energy dependent displacement cross section. The displacement cross-section is the probability of the displacement of lattice atoms by incident particles and is defined by:

$$\sigma_D(E_i) = N \int_{\check{T}}^{\hat{T}} \phi(E_i, T) \upsilon(T) dT \qquad \text{Equation 2-3}$$

where $\phi(E_i, T)$ is the probability that a particle of energy E_i will impart a recoil energy T to a lattice atom, and $\upsilon(T)$ is the number of displaced atoms resulting from this type of collision [18]. The end result of collisional events caused by radiation is a significant rearrangement of atoms in the material. The energy transfer cross-section, and hence the damage rate, is dependent on the type of incident particle and its incident energy.

In their simplest approximation (the *hard-sphere* approximation), the collisions can be treated as a purely ballistic processes, which is quite appropriate for neutron collisions. But for ion-atom or atom-atom collisions, this model is invalid due to electron and nuclear interactions in ion-atom or atom-atom collisions. To overcome this limitation, depending on the minimum separation distance between particles during a collision, a Coulomb-, a screened Coulomb-, or a Born-Mayer potential can be utilized. The expressions for these three potentials are, respectively:

1. Coulomb potential: $U_{i,j} = {}^{q_i q_j}\!/_{r_{ij}}$,
2. Screened Coulomb potential: $U_{i,j} = {}^{q_i q_j}\!/_{r_{ij}}\, e^{-r_{ij}}$
3. Born-Mayer: $U_{i,j} = A_{ij} e^{{}^{-r_{ij}}\!/_{\rho_{ij}}}$

As a result, different ion types and energies lead to different cascade physics. Neutrons and heavy ions tend to produce large-scale, dense damage cascades that result in significant recombination during the cascade quench process. Protons, on the other hand, tend to produce more localized and widely spaced cascades resulting in a higher number of freely migrating point defects.

Quantification of the damage caused by particle irradiation is needed to evaluate the ability of a material to resist radiation. For charged particle species, the numerical values used to quantify the damage imparted to the material can be derived from software based on Kinetic

Monte Carlo simulation, known as Stopping Range of Ions in Matter (SRIM) [19]. SRIM calculates the stopping and range of ions (up to 2 GeV/amu) into matter using a quantum mechanical treatment of ion-atom collisions. This calculation is made by the use of statistical algorithms which allow the ions to make jumps between calculated collisions and then averaging the collision results over the intervening gap. During collisions, the ion and atom experience screened Coulomb potentials, including exchange and correlation interactions between the overlapping electron shells.

The inputs that must be given to the SRIM are the material composition, the displacement energy of each of the elements in the material, the density of each layer, the incident ion type and its energy. The limitations of this program are that they do not include time dependence, temperature dependence, and crystal structure of the material. Moreover, only homogenous materials can be studied (other than layered compounds). Once a simulation is completed, the total dpa can be calculated as [20]:

$$dpa = 0.8 \cdot T_{dam}(E_{PKA})/2E_d \qquad \text{Equation 2-4}$$

where T_{dam} is called the *damage energy*. It is calculated as

$$T_{dam}(E_{PKA}) = \frac{\phi \cdot (E_i^p + E_t^p)}{N} \qquad \text{Equation 2-5}$$

where N is the atomic density of the target, ϕ is the fluence, E_i^p is the Beam energy lost to phonons, E_t^p is the target atom energy lost to ionization. $T_{dam}(E_{PKA})$ represents the portion of the PKA energy that is dissipated in elastic collisions with atoms in the lattice.

2.2 Ion Beam Mixing (IBM)

2.2.1. Theory and Background

During energetic ion irradiation, the ions penetrate the solid and in doing so they slow down and deposit their energy via interaction with the atoms and electrons of the material, before ultimately coming to rest if the target material is of sufficient thickness [21]. When these interactions occur across interfaces of thin bilayers composed of two materials, the radiation damage cascades can cause significant compositional redistribution across the interface, leading in effect to the intermixing of the different elements composing the bilayer structure (**Figure 2-2**). This phenomenon is known as ion beam mixing (IBM). IBM is therefore defined as the atomic intermixing and alloying that can occur at the interface of the two different materials during ion irradiation [22].

Many studies were conducted in the area of ion beam mixing during the 1980s-90s and the principal parameters governing this phenomenon have been outlined. A variety of physical processes occur simultaneously and must be taken into account to describe this physical phenomena [22]. These include (i) ballistic mixing (which includes recoil implantation and cascade mixing), (ii) thermodynamic effects and (iii) temperature effects. These effects are briefly discussed in the following sections.

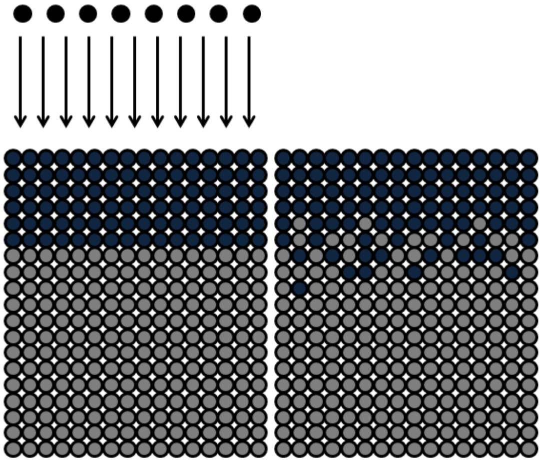

Figure 2-2: Irradiation by energetic charged particles or neutrons can cause atomic rearrangement of atoms across the interface in a bilayer system composed of two materials causing atomic intermixing.

2.2.2. Recoil Implantation and Cascade Mixing

Ballistic mixing results from displacement of atoms from their lattice sites and their relocation, a process known as recoil implantation or recoil mixing [22]. Using a two body collision model, the maximum amount of kinetic energy that can be lost in a single collision is expressed by the following equation [19]:

$$T = \frac{4M_1M_2}{(M_1+M_2)^2}Ecos^2(\theta) \qquad \text{Equation 2-6}$$

Where M_1 and M_2 are the masses of the incoming particles and the target, E is the energy of the incoming particle and θ the collision angle. The maximum energy transfer occurs for an angle of incidence θ equal to zero (i.e., a head-on-collision), however low angle collisions are far more probable and therefore in most of the collisions just a small fraction of the incident ion energy is transferred to the target [23]. Typically the energetic ion displaces several atoms as it traverses the material and these displaced atoms will in turn displace other atoms, before coming to rest. Physical insight of this process (*cascade mixing*) has come from heavy ions irradiations at low temperatures (up to 300K) and from studies using thin layer markers inserted between two layers of a matrix [24]. When these systems are irradiated, the resulting isotropic spreading of the markers with a characteristic Gaussian profile, as shown in **Figure 2-3**, suggests a contribution from radiation-enhanced diffusional processes [25].

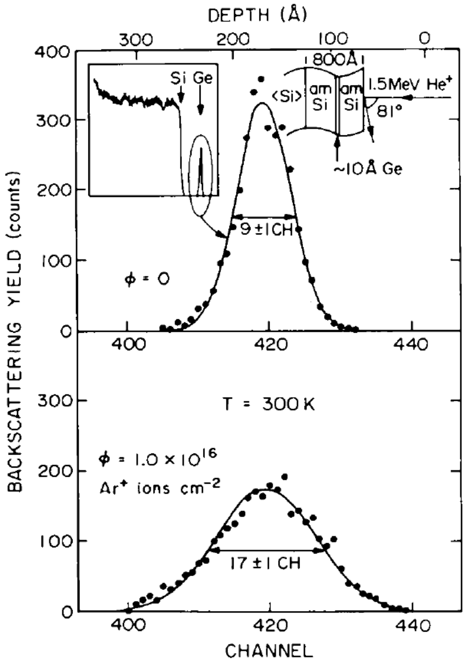

Figure 2-3: Backscattering signals obtained from the Sn marker embedded in amorphous Si before irradiation (top) after 3x10^{16} ions/cm^2 Ar$^+$ irradiation (bottom) (from Ref. [24]).

Of particular importance is the concept of *mixing parameter* $^{Dt}/_{\phi}$ [21], where *D* is an effective diffusion coefficient, t is the duration of the cascade and ϕ is the dose of irradiation. The value of Dt can be deduced from Ω^2 where Ω the energy variance in the Gaussian distribution. For the 80-300 K temperature range the Dt value has been found to be temperature independent as determined by using several marker materials (Ni, Ge, Sn, Sb, Pt and Au) buried in Si targets [21,24].

2.2.3. Thermodynamic effects in ion beam mixing

Thermodynamic effects play an important role in IBM phenomenon and in fact the enthalpy of mixing and the cohesive energy can dictate the intermixing behavior of bilayers [26–28]. The enthalpy of mixing is an indicator of the attraction between the atoms of different elements relative to the attraction between atoms of the same element. When enthalpy value is positive, mixing is endothermic and not favored and conversely when its value is negative, mixing is exothermic and favored. According to regular solutions theory the enthalpy of mixing is given by [29]:

$$\Delta H_{mix} = X_A X_B \Omega_H \qquad \text{Equation 2-7}$$

where X_A and X_B are the molar fraction of the elements A and B and Ω_H can be approximated by:

$$\Omega_H \sim Z_c N_a \left[H_{AB} - {}^{1}\!/_{2}\,(H_{AA} + H_{BB})\right] \qquad \text{Equation 2-8}$$

where Z_c is the coordination number of the lattice cell, N_a is the Avogadro's number and H_{ij} is the mean potential between atom pairs. Intermixing is thus favored in a layered system with negative enthalpy of mixing and, conversely, the de-mixing driving force can even overwhelm ballistic effects for systems with positive heat of mixing [30]. In many systems with similar ballistic properties but different ΔH_{mix} (Pt or Au with a 3d valence metals such as Ti, V, Cr, Mn, Co, Ni), a linear relationship was found between the mixing parameters and ΔH_{mix} as shown in **Figure 2-4** [31].

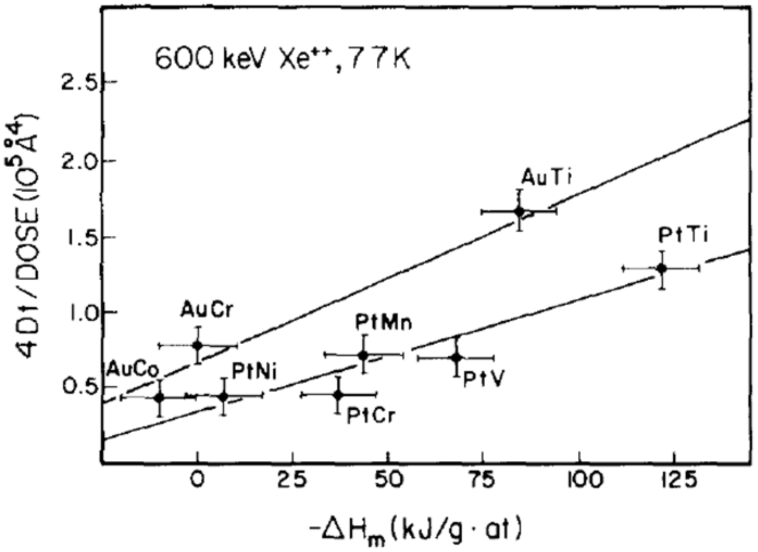

Figure 2-4: Correlation between the mixing parameter and the heat of mixing for various bilayers irradiated with 600 KeV Xe^{++} at 77K (from Ref. [31]).

Taking into account the role of the enthalpy of mixing, the interdiffusion coefficient can be expressed by the following equation developed by Darken [25]:

$$\widetilde{D} = \widetilde{D}_0 \left(1 - \frac{2\Delta H_{mix}}{K_B T}\right) \quad \text{Equation 2-9}$$

where $\widetilde{D}_0$ can be determined from the expression $\widetilde{D}_0 t = 0.067 \frac{F_d \langle r^2 \rangle}{N_0 E_d} \phi$, an expression for the mixing parameter [32] in which F_d is the damage energy per unit length, r is the range of the displaced target atoms, N_o is the is the atomic density, E_d is the displacement energy of the target and ϕ is the ion dose.

Other systems, with similar ballistic properties, have been shown behave differently when intermixed even for $\Delta H_{mix} = 0$. By forming several bi-layers belonging to the 5d-4d valence metals which form ideal solutions, the mixing rate was observed to be influenced by the average cohesive energy [33]. The cohesive energy is defined as the difference between the energy of a material as compared to the energy of the same material when all the atoms separated by an infinite distance. Generally, materials with high cohesive energy have high melting points and vice versa [22]. Therefore, it is reasonable to argue that in materials with high cohesive energy the cascade induced by the ion bombardment will be quenched sooner than materials with a lower cohesive energy, leading to the conclusion that low cohesive energy will favor intermixing. **Figure 2-5** shows the correlation between the mixing parameter and the cohesive energy.

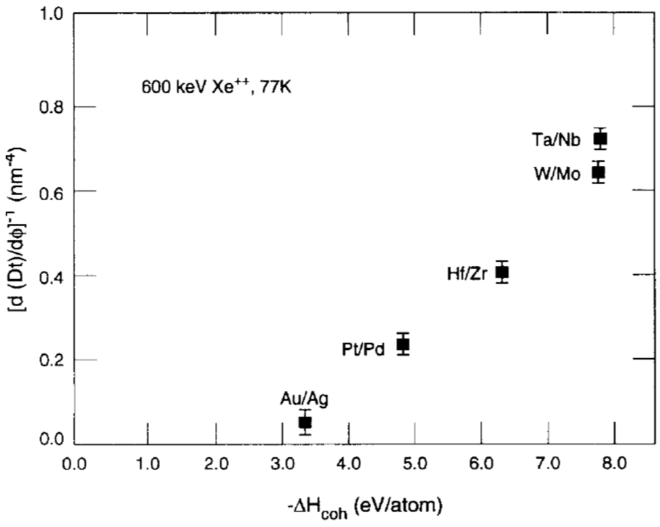

Figure 2-5: Relationship between ion irradiation induced mixing and cohesive energy for different bi-layered systems (from Ref. [33]).

2.2.4. Temperature effects in ion beam mixing

IBM is strongly influenced by temperature, as shown **Figure 2-6**. Two different regimes can be identified, a temperature independent regime at low temperatures and a temperature dependent regime at higher temperatures.

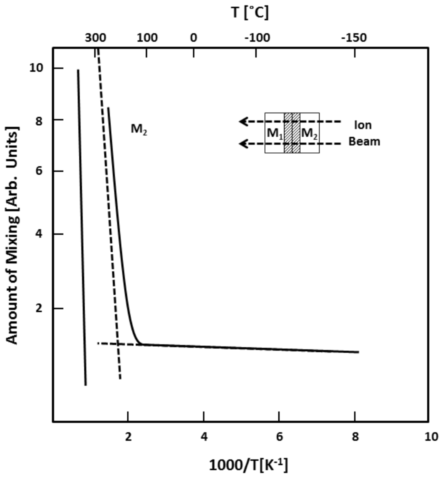

Figure 2-6: Effect of temperature on ion beam mixing. Increasing the temperature above a certain value causes the degree of mixing to change rapidly with temperature (adapted from Ref. [34]).

On the left side of the graph, the vertical curve represents the mixing induced just by thermal effects. Its behavior is described by an Arrhenius type curve, whose slope is determined by the activation energy of the process. The elbow-shaped curve represents ion mixing of a metallic bilayer in the presence of an irradiating species. Two different regimes can be identified: a temperature independent regime, at the low temperatures, in which the mixing of the system is not sensitive to a change in temperature, and a temperature dependent mixing regime, where temperature has a major effect on mixing. Again, the temperature dependent regime of the curve can be described with an Arrhenius type plot -therefore the difference between the two Arrhenius type plots can be attributed to radiation enhanced diffusion. It must be noted that the low temperature mixing is due to ballistic mixing rather than a diffusion enhancement due to radiation [13]. The critical temperature T_c sets the difference between the temperature dependent and the temperature independent mixing, and can be determined by the following effective diffusion coefficient equation [35]:

$$D = D_{ballistic} + D_{rad} e^{-Q/_{KT}} \qquad \text{Equation 2-10}$$

where $D_{ballistic}$ is the temperature independent term due to ballistic mixing, $D_{rad} e^{-Q/_{KT}}$ is the temperature dependent term due to enhancement of diffusion by radiation and Q is the activation energy. Assuming Q to be proportional to the cohesive energy, the temperature at which the two contributions are equal can be calculated as follows:

$$T_c = Q\Big/K \left[ln\left({D_{rad}}/{D_{ballistic}} \right) \right] \qquad \text{Equation 2-11}$$

A linear relationship is indeed found between the critical temperature and the cohesive energy, as shown in **Figure 2-7**.

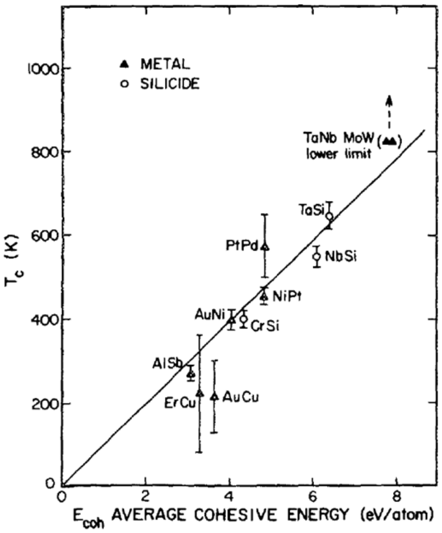

Figure 2-7: Correlation between the average cohesive energy and the critical temperature that marks the transition between ballistic mixing and regime of radiation-enhanced of diffusion (from Ref. [35]).

The data shown in **Figure 2-7** are taken from different sources in which different ion species, energies, doses, and dose rates were used and therefore these parameters can be safely assumed as less important than the cohesive energy's effect on the value of the critical temperature of the irradiated system.

2.3 Materials Challenges in a Nuclear Reactor Environment

2.3.1. Effect of Radiation and Temperature on Microstructure

Figure 2-8 shows examples of typical temperature-dependent microstructures, formed in irradiated materials as imaged by TEM [36]. These microstructural changes induce a variety of property changes which can severely affect the performance of materials in nuclear reactor systems. As can be seen in this figure, the microstructural evolution is strongly dependent on the irradiation temperature [37]. Five major defect recovery stages which dictate the types of microstructural changes can be identified. Stage I represents the onset of long-range SIA migration while Stage II represents the onset of small SIA clusters and SIA-impurity complexes migration. Stage III marks the onset of vacancy motion and Stage IV marks the onset of vacancy–impurity clusters migration. Finally, in Stage V thermal dissociation of sessile vacancy clusters is initiated. It must be noted that although there is a general correlation of the defect recovery temperatures with melting temperature of a material, significant exceptions exist [37]. Elements like platinum for example, although having a very high melting temperature has one of the lowest Stage I temperature among FCC metals. Chromium on the other side, although having a lower melting temperature than vanadium or niobium, has a much higher Stage III temperature.

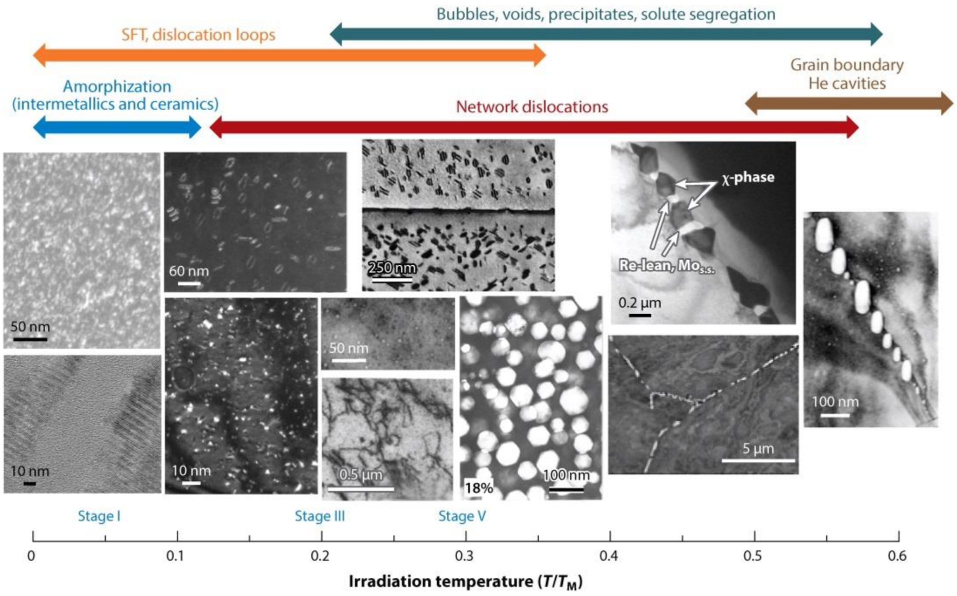

Figure 2-8: Examples of representative microstructures in irradiated materials as a function of irradiation temperature materials as imaged by TEM. Description of stages I,II, III, IV and V are given in the main text. SFT stands for stacking fault tetrahedral (from Ref. [36]).

To date five important radiation-induced property degradation effects have been identified [5]. At low temperature irradiations ($T < 0.35T_m$), hardening and embrittlement, caused by the formation of dislocation loops and small helium clusters, are observed. The increase in hardness is caused by small defects clusters, as they impede dislocation motion, and is generally accompanied by a reduction of fracture toughness and tensile elongation [38,39]. This is also accompanied by a shift in the ductile-to-brittle transition temperature to higher values. At intermediate temperatures ($0.35T_m < T < 0.5T_m$), the most commonly observed degradation mechanisms are radiation-induced solute segregation and phase stability, swelling and anisotropic growth, and irradiation creep. Radiation-induced solute segregation can cause either the precipitation of second phases in materials, such as embrittling α’ phase in neutron irradiated FeCr alloys (for Cr levels > 7% atomic) [40] or the selective enrichment or depletion of certain elements at specific sites such as grain boundaries for ferritic-martensitic steels

[41,42]. Swelling is caused by the aggregation of vacancies to form voids which then accumulate to result in a macroscopic volume change of the material. Irradiation increases creep rate over the usually observed thermal creep, and furthermore it can also induce creep in temperatures where thermal creep is usually not observed [13]. Finally, at high temperatures (T~0.5T_m) where most of the radiation damage defects are expected to get efficiently annealed, helium produced by transmutation reactions (n,α) within the material can diffuse to grain boundaries and form bubbles, causing embrittlement and a reduction in the total elongation [43–46]. **Figure 2-9** shows a schematic illustration of some of the main bulk radiation damage effects on reactor materials.

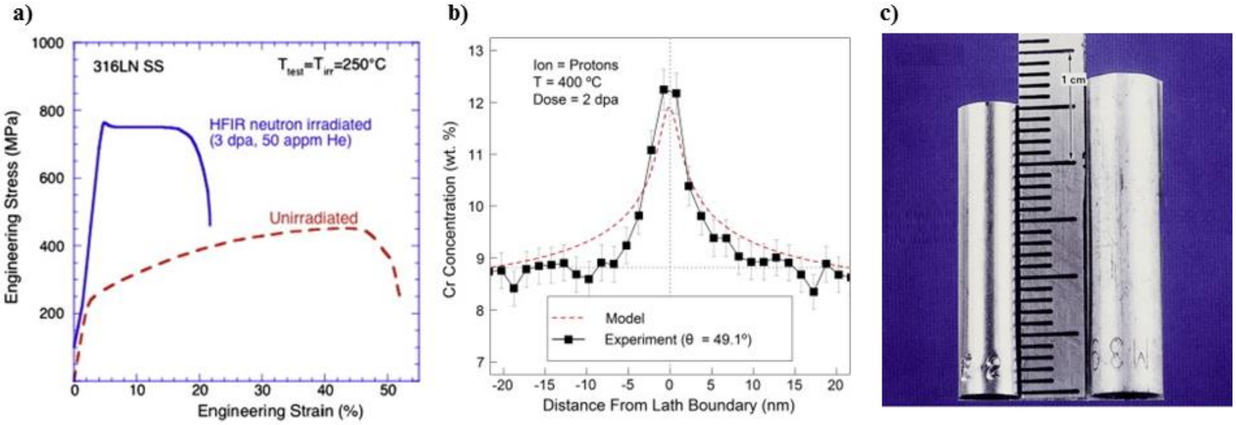

Figure 2-9: Representative examples of radiation effects on materials: (a) radiation-induced hardening in a 316LN stainless steel (from Ref. [39]), (b) radiation-induced segregation of Cr at grain boundaries in a 9%Cr ferritic steel (from Ref. [47]) (c) macroscopic ramifications of neutron induced void swelling (from Ref. [48]).

2.3.2. Helium behavior in alloys

One of the unavoidable consequences of the exposure of structural materials to an intense neutron radiation field is the formation of helium in the microstructure, by either neutron-induced (n,α) transmutation reactions or direct injection (in fusion devices). It is known that helium is mostly insoluble in metals [49,50] and forms bubbles at very low concentrations, degrading the mechanical properties over a range of temperatures. Helium bubbles can contribute to hardening at low and intermediate temperatures, while at high temperatures (~0.5 T_m), where most of the other radiation damage effects can potentially be annealed out, helium can diffuse to grain boundaries, particularly high angle grain boundaries, to form bubbles (**Figure 2-10**) that weaken the materials strength and reduce its ductility [5,45]. Generation II and III nuclear reactors are already showing evidence of helium embrittlement, prompting concerns in Generation IV nuclear reactor components where radiation doses and temperatures will be significantly higher.

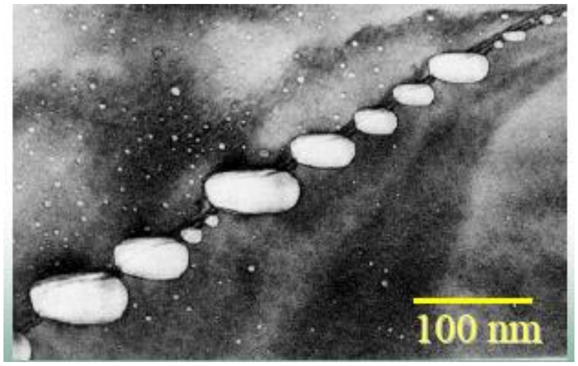

Figure 2-10: Helium bubbles accumulation at grain boundaries at temperatures > 0.5Tm and > 10dpa (from Ref. [51]).

It is necessary to effectively manage the helium generated in order to minimize the aforementioned deleterious effects on properties. An understanding of the macroscopic effects of helium bubble formation is very complex and requires a knowledge of the configuration of helium atoms in the alloy matrix, their mutual interaction and their interaction with the host alloy defects, the kinetics of bubble nucleation and growth, and establishing exact relationships between the changes in the microstructure and corresponding changes in the mechanical properties [45]. Void swelling is a degradation process that effectively illustrates how effects of radiation damage and helium production can combine to severely deteriorate the properties of irradiated materials. In fact, helium bubbles are usually a prerequisite for voids formation - without stabilization by a gas pressure, small vacancy clusters rapidly dissolve owing to the Gibbs-Thompson effect [16] and there is evidence that suggests that gas atoms are always involved in the void nucleation process [13]. Thus, helium stabilizes small vacancy clusters making them resistant to thermal annealing [52]. The vacancy clusters can then continue to grow by helium absorption until they reach a critical size [53], at which point they can, in theory, indefinitely grow by vacancy absorption without requiring the stabilizing gas [54].

The simplest model to describe helium bubble nucleation and growth, and eventual transition to unstably growing voids (responsible of void swelling) is the critical bubble model (CBM) [60]. In essence, the model uses of the simplest form of rate theory, ignoring the effects of cascade defect clustering and recombination, and considering only single mobile vacancies and SIA defects. It must be noted that CBM is very useful as it relies on a relatively modest number of parameters and parameter combination that are reasonably well known, such as the defect production, recombination, dislocation bias, sink strengths, interface energy, and self-diffusion coefficient. Based on these assumptions the growth rate of a cavity containing helium atoms can be expressed as:

$$ {}^{dr}\!/_{dt} = \frac{D_v X_v - D_i X_i - D_v X_{ve} e^{\frac{\left({}^{2\gamma}\!/_{r_c} - p\right)\Omega}{KT}}}{r} \qquad \text{Equation 2-12} $$

where the $D_v X_v - D_i X_i$ term represents the cavity radius increase due to the flow of excess vacancies and $-D_v X_{ve} e^{\frac{\left({}^{2\gamma}\!/_{r_c} - p\right)\Omega}{KT}}$ represents the emission of vacancies from the cavity at a rate under the capillarity approximation. Helium bubbles are usually stable and they grow via the addition of helium atoms, until the bubble reaches a critical size m*, where the bubble converts to an unstably growing void. Growth stability and instability conditions occur when ${}^{dr}/_{dt} = 0$. The solutions for this condition are $-{}^{2\gamma\Omega}/_{KTln(\Lambda)}$ and ${}^{3m\Omega}/_{4\pi\ln(\Lambda)}$, where $\Lambda = \frac{(D_V X_V - D_i X_i)}{D_{sd}}$ is an effective vacancy supersaturation coefficient. The smaller root of **Equation 2-12** represents the radius r_b of a stable (non-growing) bubble containing m He atoms and the larger one, r_v, corresponds to critical radius of a cavity that transforms to a growing void. **Figure 2-11**, shows a schematic plot ${}^{dr}/_{dt}$ as a function of the cavity radius for an ideal gas case.

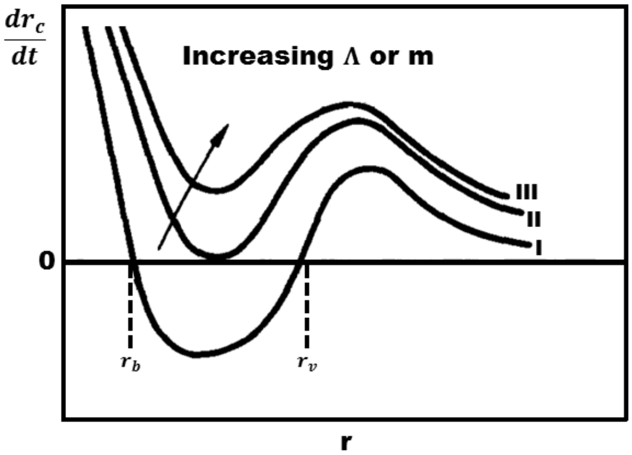

Figure 2-11: Schematic plot of the cavity radius growth rate as a function of the cavity radius (from Ref.[54]).

The three curves in **Figure 2-10** represent different limiting cases of a subcritical (I), critical (II) and supercritical (III) cavity. Mathematically, for case I **Equation 2-12** has three real and different roots, for case II **Equation 2-12** has three real roots of which 2 are equal, and for case III **Equation 2-12** has one real root and 2 imaginary conjugated ones. It must be noted that one solution is always negative. In curve I, the negative regions of the y-axis represent the barrier to void nucleation. If a cavity absorbs an excess of vacancies without an increase in the helium content, then the probability of vacancy emission increases and the cavity will tend to shrink in size. Of course, statistically, some cavities will reach a size r_v at which point they would be considered as voids. At this point no barrier to growth exists and cavity will continue growing unstably. In curve II instead, the condition $r_b = r_v = r^*$ and $m_{He} = m^*$ represents the bubble to void conversion by helium absorption which is believed to be the most likely mechanism of void formation as demonstrated for irradiated stainless steels [54]. Finally, curve III does not have physically realistic roots and it represents the case of either a cavity with $m_{He} > m^*$ or a situation of high vacancy supersaturation for which only void growth is possible. Voids can also form on critical bubbles located at precipitate interfaces at a smaller m* than in the matrix, a result of the surface–interface tension balances that are determined by the wetting angle between the bubble and precipitate interface [55].

In literature other models also exist to evaluate the critical bubble parameters and they either rely on the use of master correction curves for m* and r*, or more simply account for real gas behavior based on a Van der Waals equation of state, but yield very similar results [54]. The critical value m* is consistent with the observation of precipitate associated voids, bimodal bubble voids size distribution, and the incubation dose (*dpa_i*) needed for a population of N_b growing bubbles to reach m^* [16]:

$$dpa_i = \frac{10^6 \Omega_a m^* N_b R_D}{[\frac{He}{dpa}]} \qquad \text{Equation 2-13}$$

where N_b is the bubble number density and Ω_a is the atomic volume.The value of m* is proportional to $log(\Lambda)^{-2}$where $\Lambda\,(> 1)$ resulting from the preferential annihilation of SIA at dislocations which leaves an excess flux of irradiation induced vacancies at other sinks. Examining **Equation 2-13** it is clear how having a high population of bubbles (high N_b) increases the value of the incubation dose by a synergistic increase of the neutral sink strength, (decrease of Λ), and the partitioning of helium to more numerous bubble sites. Thus, on one hand helium is generally a necessary ingredient for void formation; on the other hand, a very high number density of bubbles can actually retard swelling [55,56].

2.4 Materials Development for Gen IV reactors

2.4.1 Brief Overview of the Generation IV reactor concepts

As shown earlier in **Figure 1-1**, the Gen IV designs would operate at higher temperatures and radiation doses as compared to Gen II and III, placing a significantly greater importance on the integrity of materials as compared to current nuclear reactors. **Table 1** summarizes the approximate temperature, dose conditions, and environmental conditions for these reactor concepts.

Table 1. Approximate operating environments for Generation IV systems [57].

Reactor type	**Coolant T_{in} [°C]**	**Coolant T_{out} [°C]**	**Maximum Dose [dpa]**	**Pressure**	**Coolant type**
SCWR	290	500	15-67	25	Water
VHTR	600	1000	1-10	7	Helium
SFR	370	550	200	0.1	Sodium
LFR	600	800	200	0.1	Lead
GFR	450	850	200	7	Helium/SC CO_2
MSR	700	1000	200	0.1	Molten Salt
LWR	290	320	100	16	Water

The six Gen IV concepts can be grouped into three general categories according to the temperature and radiation damage levels that would be experienced by structural components in these respective reactor concepts. SFR, LFR and MSR will operate at high temperatures and very high dose or damage levels, and will utilize either liquid metal or molten salt as the coolant. GFR and VHTR components will experience lower damage levels but extremely high temperatures, and will use the relatively inert helium as the coolant (although impurities in helium are known to cause corrosion). The SCWR will utilize water as coolant but at higher temperatures and pressures (than LWR) where corrosion and stress corrosion cracking (SCC) issues may become important, but at dose and damage levels comparable to current LWR [5].

Materials development strategies and selection cross-cut Gen IV reactor concepts in regards to irradiation effects [57]. The differences stem primarily from corrosion issues which can be mechanistically different depending on the coolant and the temperature. Therefore, given the diverse property requirements, coatings are being recently considered for enhancing corrosion resistance for alloys that may be deemed appropriate from the standpoints of radiation damage effects and high temperature creep strength.

BCC ferritic or ferritic-martensitic steels exhibit the very desirable trait of low swelling under radiation, but have low creep strength at high temperatures. FCC austenitic alloys have superior high temperature strength but are inherently prone to swelling under radiation. Extensive research is underway to enhance high temperature creep strength of ferritic steels so that a combination of high temperature strength and void swelling can be realized. A notable example in this regard is oxide dispersion strengthened steels (ODS) that contain nanoparticles (or nanoclusters) of (Y, Ti)-oxide in a ferritic matrix (discussed in detail in a later section).

High temperature creep strength and resistance to radiation damage at high dpa levels are key requirements for all Gen IV reactors. At these high damage levels, voids swelling and phase instability will most likely drive the degradation modes. Therefore, materials development efforts for these reactors and environments place increased emphasis on strength, creep and creep-fatigue behavior in addition to fracture toughness at low temperature. Void swelling exceeding 5% is generally considered unacceptable based on typical engineering considerations and furthermore irradiated austenitic steels have been observed to severely embrittle for swelling greater than 10% [58].

Alloys with BCC and hexagonal-closed packed (HCP) crystal structures exhibit lower residual defect production efficiency than alloys with face-centered cubic (FCC) structures [59–61], although the anisotropic growth observed in irradiated HCP materials generally excludes this class of materials for high dose applications [36]. The physical mechanisms responsible for the higher radiation damage resistance of BCC steels are not fully understood. It has been experimentally observed under TEM that BCC alloys are characterized by a more finely dispersed distribution of defect clusters compared to FCC alloys within energetic displacement cascades [61,62], which can lead to more efficient defect recombination during subsequent microstructural evolution. Similar differences in defect accumulation are observed in FCC and BCC steels irradiated at temperatures at which voids swelling occurs [36]. Years of research have succeeded in extending the low swelling transient regime in FCC steels, with the development of Ti-modified austenitic steels reinforced with a fine dispersion of TiC precipitates. An example of this is shown in **Figure 2-11**, where interfaces of fine carbide phase particles in austenitic stainless steel matrix can be directly observed to act as sites for helium bubble formation (and by extension for other types of morphological defects). However, the improvements obtained are still not sufficient to avoid unacceptable levels of voids swelling at very high doses, and steels with ferritic structure still continue to be deemed more suitable for such applications.

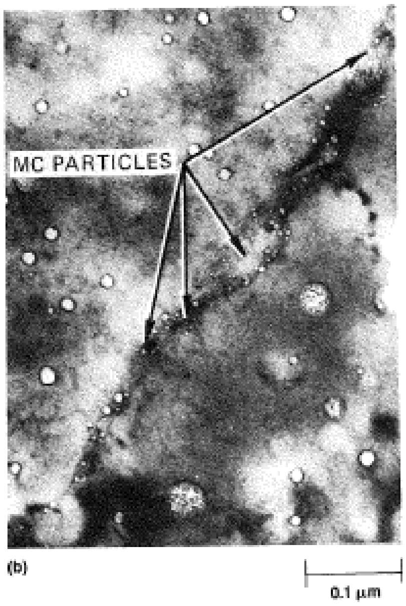

Figure 2-12: TEM image showing the interfaces between fine carbide phase particles and austenitic stainless steel matrix acting as sites for helium bubbles (from Ref. [63]).

A variety of approaches for developing radiation-resistant materials have been proposed and tested over the past 50 years [36] and the main strategies to increase radiation tolerance in materials are based on either the use of (i) radiation-resistant matrix phases – such as BCC materials (compared to FCC), (ii) creation of immobilized point defects, and (iii) engineered high-sink-strength microstructures. Approach (ii) is based on the introduction of point defect recombination sites, and can be achieved by selecting materials for which one or both of the radiation-induced point defects (interstitials and vacancies) are immobile at the anticipated operating temperatures. For this approach to be feasible, the temperature should be above recovery Stage I (to avoid amorphization in ceramics and formation of intermetallic compounds in alloys – which is typically accompanied by undesired volumetric changes (46)) and below

Stage III (to avoid the void-swelling regime). However, for most alloys the onset of vacancy motion occurs at too low of temperatures for this concept to be viable as a radiation-resistance mechanism in nuclear energy systems.

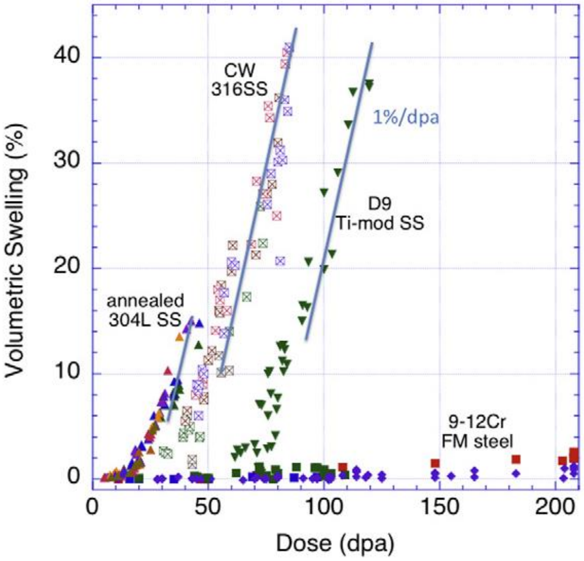

Figure 2-13: Comparison of the volumetric swelling resistance of 304L, 316, Ti modified (D9) FCC stainless steels and 9–12% Cr-tempered ferritic/martensitic steels after fast neutron irradiation at ~400-500ºC (from Ref. [5]).

Approach (iii) is based on the design of materials with a high density of point defect sinks. This approach is predicated on kinetic rate theory models [48,64,65] that have shown that high sink strengths can reduce point defect supersaturation values and related phenomena such as void swelling and radiation-induced solute segregation. Experimental studies have shown that high concentrations of dislocations [66] and finely dispersed precipitates [67] can play a fundamental role in void-swelling suppression, thus corroborating kinetic rate theories. Grain size can also be reduced via severe plastic deformation [68], thus increasing the density of grain boundaries which are paramount to healing radiation damage [69,70]. As discussed earlier, engineering the microstructure to have a fine distribution of precipitates such as TiC precipitates in stainless steel or (Y, Ti)-oxide nanoparticles in a ferritic matrix can dramatically enhance radiation damage resistance. **Table 2** shows some of the alloys that are being considered for Gen IV reactor applications.

Table 2. Nominal Compositions of alloys being investigated for nuclear reactor applications.

Alloy	**C**	**N**	**Al**	**Si**	**P**	**S**	**Ti**	**V**	**Cr**	**Mn**	**Fe**	**Co**	**Ni**	**Cu**	**Nb**	**Mo**	**Ta**	**W**
Ferritic																		
HCM12A	.11	.063	.001	.27	.016	.002	-	.19	10.83	.64	Bal.	-	.39	1.02	.054	.3	-	1.89
T91	.1	.048	.022	.28	.009	.003	-	.216	8.37	.45	Bal.	-	.21	.17	.076	.9	-	-
HT-9	.21	.005	<.01	.30	.013	.005	<.01	.3	11.94	.69	84.36	.03	.62	.02	-	1.03	-	.48
NF616	.109	-	.005	.102	.012	.003	-	.194	8.82	.45	Bal.	-	.174	-	.064	.468	-	1.87
9Cr ODS	.14	-	-	.048	<.05	.003	.21	-	8.6	.05	Bal.	-	.06	-	-	-	-	2
Austenitic																		
800H	.069	-	.5	.13	.014	.001	.57	-	12.42	.76	45.26	-	31.59	.42	-	-	-	-
D9	.039	.004	<.01	.8	.005	.003	.34	.01	13.7	2.03	Bal.	<.01	15.8	<.01	-	1.65	<.01	-
SS316	.017	.053	<.01	.55	.025	.002	<.01	.06	17.29	.91	Bal.	.11	10.9	.24	-	2	-	-
347	.08	-	-	1.0	.045	.03	-	-	17-19	2.	Bal.	-	9-13	-	-	-	-	-
Fe-Ni based																		
625	.01	-	.2	.11	-	.001	.21	.014	21.9	.08	4.39	.05	61.22	.19	-	8.43	.004	-
718	.031	-	.57	.1	-	.001	1.05	.017	18.11	.08	18.04	.04	53.85	.03	5.03	2.96	.008	.015
690	.032	-	.2	.03	-	.0007	.35	.013	29.58	.2	1.23	.009	59.32	.008	<.001	.011	.001	.002
Zr-alloys																		
Zr-1.32%Sn-0.18%Fe																		

Recently, ferritic Fe-Cr-Al alloys are also recently being considered as accident tolerant fuel cladding for LWRs (and can be potentially applied to Gen IV concepts) on account of their ability their ability to form Al-rich protective oxide layers at high temperatures. Nevertheless, despite exciting results from the corrosion standpoint, the applicability in the high temperature range is limited by thermal creep concerns [68].

Another class of potentially radiation resistant materials is ceramics, which are particularly appealing due to their chemical inertness. In particular, the radiation damage response of SiC has been extensively studied and documented and has been shown be acceptable [71]. The main issue with ceramics in general is their lack of plasticity at low homologous temperatures, lending skepticism to their utilization for structural components for which catastrophic failure is not an option [72]. For this reason, SiC-SiC and C-C composites on account of their excellent high strength are being considered for use for all Gen IV applications for operation up to 1000 ˚C or higher. However, large-scale manufacturability issues (including joining) are still being investigated.

Large plastic deformation at low temperature (up to 100%) in ceramics with crystal size of few nanometers has been observed [73] suggesting that nano-ceramics could be an option in the future. This class of materials may potentially benefit simultaneously from both the radiation tolerance and enhanced deformation modes. This coupled with the inherently high chemical inertness of ceramics could make these nanoceramics attractive candidates for structural materials in Gen IV reactors. Ceramic with fluorite crystallographic structure, has been shown to exhibit superior tolerance to radiation-induced amorphization most likely because of the intrinsic ability of this structure to accommodate disorder. Along these lines, amorphous metallic glasses [74] are also being studied due to the absence of order which precludes the formation of Frenkel (vacancy-interstitial) defects by energetic irradiation, although a variety of molecular defect aggregates can be produced [36].

Refractory metals such as Nb, Mo, Ta and W- and their alloys, are potential interesting materials due to their melting points which are typically in excess of 2000°C. Although they are characterized by good creep resistance and swelling resistance up to high radiation doses, other issues, such as poor oxidation resistance, low temperature radiation embrittlement, fabrication (joining) concerns, high atomic number for W and Ta (which has a negative impact on neutron economy and transmutation issues), have limited consideration of their applications to Gen IV reactors [75].

For Gen IV reactors that also operate with corrosive coolants, corrosion can also be an overriding concern in selection of alloys. Here the problem has to be addressed from the standpoints of both the materials and the coolant. For example, in LFR a minimum oxygen content has to be maintained in the liquid lead-alloy coolant to promote the formation of a stable oxide layer. Steels containing oxide promoting elements such as Al and Si can also be beneficial. In MSR, where the protective oxide layers on alloys are unstable in molten fluoride salt coolant, control of redox potential of the salt will be important. Alloys based on Ni and Mo which have a low thermodynamic free energy of fluoride formation are particularly desirable. In VHTR, the moisture, oxygen, and hydrocarbon impurity concentrations in the helium coolant have to be controlled at single ppm levels to prevent corrosion and to promote a stable oxide layer on the surface. In regards to SFR, liquid sodium is one of the few coolants that is not recognizably corrosive.

It is clear that radiation damage resistance, high temperature creep strength, and corrosion are important considerations for selection of materials for Gen IV reactors. While radiation damage characteristics and high temperature strength are dictated by the bulk properties of the material, corrosion is a surface phenomenon (although high corrosion attack depths can compromise load bearing capacity of components). Therefore, surface modification and coating approaches for candidate alloys (selected based on radiation damage tolerance and high temperature strength) are being increasingly considered for enhancement of corrosion-resistance in harsh environments. It is imperative that the coating be dense, capable of plastic strain, resistant to wear, have good thermal conductivity, strong bonding to the substrate, tolerant to radiation damage, and have low neutron cross-section. Coating methods being considered include physical vapor deposition (PVD), which involves the vaporization of atoms and molecules from a solid target to form the coating, chemical vapor deposition (CVD), which involves reaction between gases at high temperature to synthesize the coating, and powder spray deposition process which involves high velocity spray coating of solid or liquid powder particles on to the surface of a substrate to form the coating. Among PVD techniques, pulsed laser deposition (PLD) allows for engineering the structure and properties of coatings at the nano-scale levels. PLD process conditions can be tailored to obtain high-quality coatings with a wide range of microstructures, varying from fully dense and compact, to columnar, hierarchical or porous, and can be carried out at room temperature. The use of ceramic materials as coatings on metallic alloys is gradually gaining acceptance for example for the development of accident tolerant fuels for current and advanced light water reactors [76]. The radiation response characterization of a PLD grown Al_2O_3 coating is a subject of this research.

2.5 Role of Interfaces in the Radiation Damage Response of Materials

2.5.1 Introduction and Background

In recent years, many studies have focused on the role of interfaces on the radiation damage response of materials. In solid materials, interfaces can be classified as homophase which consists of separate crystals (grains) of the same structure and chemistry but with different orientations delineated by grain boundaries, or heterophase which consists of crystals of different structure or chemistry, as well as orientation [77]. Since the first work showing the role of grain boundaries (homophase interfaces) on the plasticity of crystalline materials [78], many studies have shown how interfaces play a decisive role in determining materials properties such as strength, fracture, work hardening [77]. However, it has been shown that by increasing the amount of internal interfaces it is possible to improve the radiation response of materials, as has been experimentally demonstrated for nano-grained nickel and copper [79], gold [80], ZrO_2 [81,82], and steels [83]. This is also corroborated by molecular dynamic simulations performed on copper [69], where vacancies were shown to annihilate in the vicinity of grain boundaries through a mechanism of interstitial emission from the grain boundaries. Additionally, nanoscale multi-layered systems have been shown to exhibit increased radiation damage tolerance as compared to their individual constituents [84,85].

2.5.2 Interfacial energy and interfaces

Solid-solid interfaces can be further classified into three different categories, depending on the relative mismatch between the two mating surfaces: coherent, partially coherent (semi-coherent), or incoherent [86]. Coherent interfaces are characterized by an almost perfect match between the two constituent materials, while in incoherent interfaces there is no registry between the two layers. When a difference in the lattice parameter between the two materials exists, strain at the interface can be released through the creation of misfit dislocations. A schematic representation of coherent, semi-coherent and incoherent interfaces is shown in **Figure 2-14**.

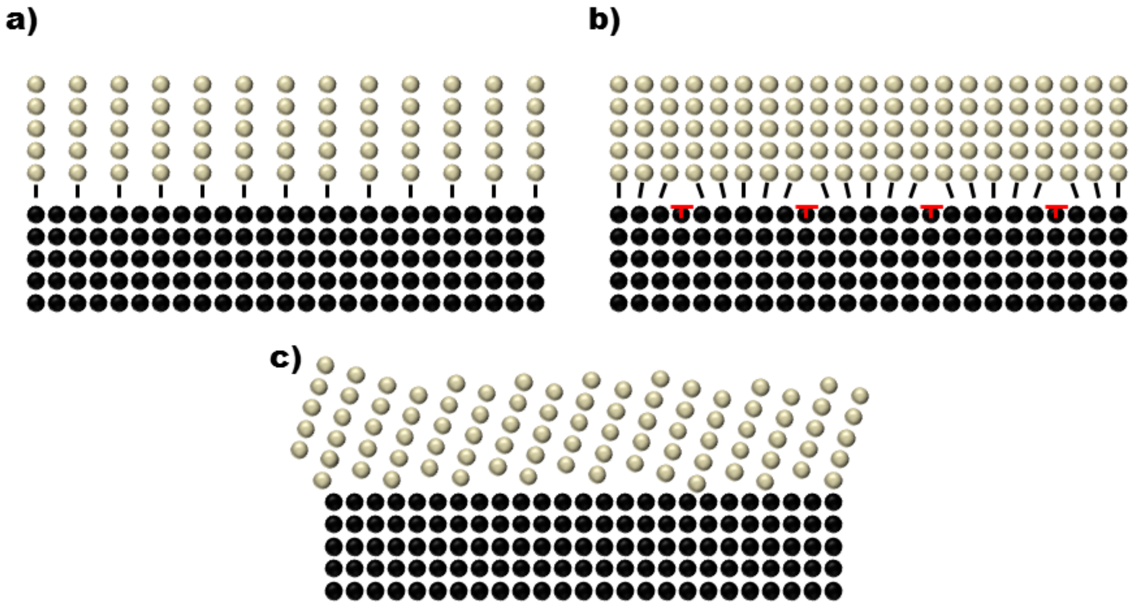

Figure 2-14: Schematic representation of (a) coherent (b) semi-coherent and (c) incoherent interfaces. Misfit dislocations in semi-coherent interfaces are periodically found to release the stress caused by lattice mismatch.

Energies of coherent interfaces (0.005-0.2 J/m^2) are lower than that of semi-coherent interfaces (0.2-0.8 J/m^2) which in turn are lower than that of incoherent interfaces (>0.8 J/m^2)[87]. Although this research focuses on planar interfaces nucleation of second phases in metallic materials will be provided, as interfacial energy plays a fundamental role in explaining some basic mechanism of second phase growth and coarsening which can then be used to interpret and understand the results given here. The role played by elastic stress induced by misfit strain at the interface is crucial in determining the equilibrium morphology of cubic lattice second phases nucleating in a metal matrix with cubic lattice [88]. In fact, the particles' shape evolution during growth will be dictated by the elastic energy, which is proportional to the volume of the particle through the elastic constant C of the two materials and the square of the lattice mismatch $\Delta = \frac{a_1 - a_2}{a_1}$ (a_i is the lattice parameter of the i-th constituent) [89]. The Gibb's free energy of the nucleus can be derived by adding the strain energy to the Gibb's free energy expression for homogenous nucleation. Because the strain affects both the phases - the matrix as well as the nucleating particle, it must be taken into account also inside the crystal. This yields the following equation (**Equation 2-14**):

$$\Delta G(r) = {}^{4\pi}/_{3}\, r^3 \Delta G_V + 4\pi r^2 \gamma + {}^{4\pi}/_{3}\, r^3 C \Delta^{\,2} \qquad \text{Equation 2-14}$$

where γ is the interfacial energy. As can be seen, the shape will depend on the balance between the interface energy of the matrix/precipitate interfaces and the elastic strain energy of precipitates [90]. For larger precipitates the elastic energy, proportional to r^3, will dominate and conversely for smaller precipitates the interface energy, proportional to r^2, will dominate. Thus, in ODS steels and NFAs smaller precipitates are typically coherent or semi-coherent with the matrix, while bigger precipitates are typically incoherent. Coarsening at high temperature can cause initially coherent precipitates to lose the coherency with the matrix.

2.5.2 Metal/Metal systems

Some of the results obtained from the IBM theory (discussed in **Section 2.2**) can be readily extended to understand the radiation response of multilayered metallic systems. The enthalpy of mixing plays a fundamental role in the radiation response of the multilayered systems. For example, immiscible systems such as Cu/V, Cu/Mo and Cu/Nb, have been shown to retain their individual layer character after room temperature helium irradiation (50-100 KeV) at doses up to 6x10^{16} cm^{-2} [84,91,92]. In Cu/V multilayers with individual layer thickness of 50 nm, helium bubbles were not visible in TEM at a nominal concentration of 0.28%, orders of magnitude greater than the helium solubility in pure metals. Owing to their high capacity to absorb helium, Cu/Nb nano-laminates have shown also to restrict the growth of He bubbles [93–95], as shown in **Figure 2-15**.

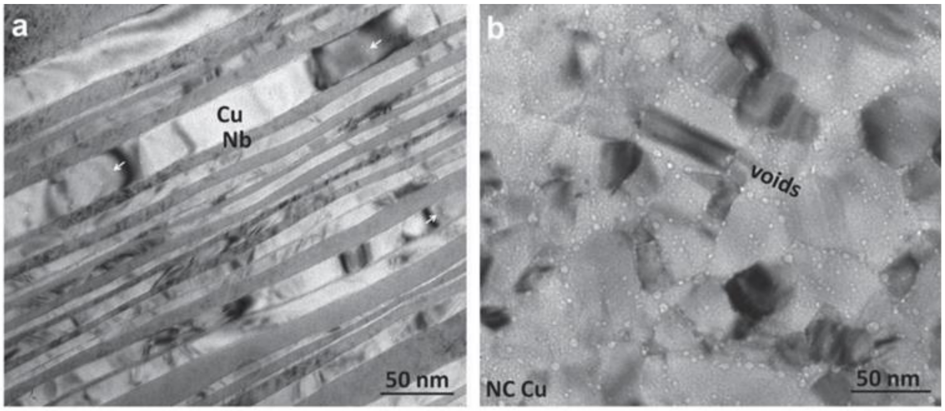

Figure 2-15: (a) Helium ion irradiated Cu-Nb nanoscale multilayered composites with 20 nm individual layer thickness showing a void free structure. Arrows indicate small, isolated voids in the thicker Cu layers. (b) irradiation damage in nanocrystalline Cu under identical irradiation conditions showing voids (from Ref. [95]).

Neutron reflectometry which has depth resolution on the order of fractions of a nanometer [96] revealed that regions of high helium concentration are localized at the Cu/Nb interface, leaving the layers themselves intact and helium free [97]. Simulations suggest [96] that misfit dislocation intersection (MDIs) plays an important role in helium management. The MDIs are stable in the presence of constitutional vacancies and the excess free volume resulting from this readily traps helium atoms. Cu/Nb interfaces have a high density of MDIs, and as a result are able to store helium more efficiently [92]. Other studies based on multi-scale modeling [98] have shown that at these interfaces helium does not always nucleate as spherical bubbles [99], but also as platelet-shaped helium-filled cavities. The origin of these stable interfacial helium platelets can be related to a location-dependent internal structure of the interface, and hence a location-specific interfacial energy. The high energy interfaces in Cu/Nb thermodynamically drive helium to occupy these regions. These platelets with sizes up to 20 atoms, and stable under radiation can store helium nearly three times more efficiently than spherical bubbles. Only after reaching a critical size, these platelets grow by increasing their thickness while maintaining the interfacial area constant [98]. **Figure 2-16** summarizes this behavior, comparing the volumetric change of an eighteen helium atom cluster at a Cu/Nb interface and in pure FCC Cu. The bubble in pure Cu has two equilibrium points corresponding to distinction between helium-stabilized bubbles and unstably growing voids by vacancy capture (see CBM model in **Section 2.3.2**) [98]. On the other hand, the Cu/Nb interface has three equilibrium points, the two similar to that in pure copper, and the aforementioned interfacial helium platelet.

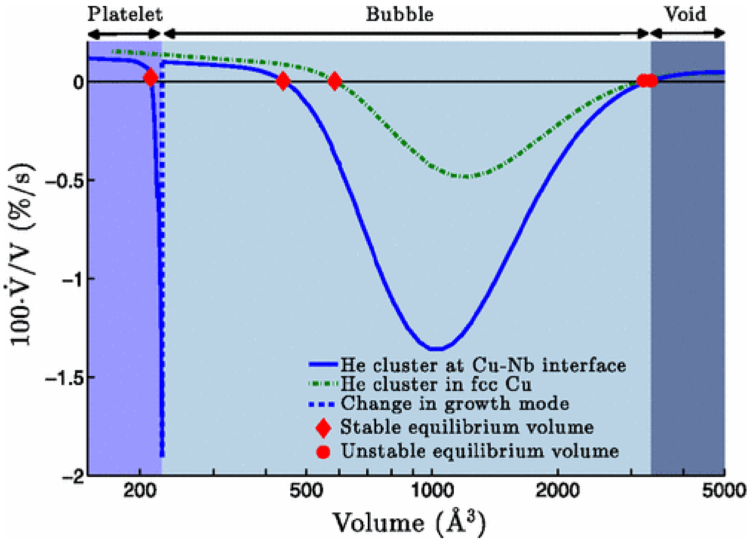

Figure 2-16: Rate of volumetric change for eighteen atom helium cluster at a Cu/Nb interface and in pure Cu(from Ref. [98]).

The individual layer thickness, which determines the fraction of internal interfaces (for a given unit volume of the multilayer system), plays an important role in the ability of these mutilayered structures to absorb radiation-induced defects. For several systems, a decrease in the thickness of the individual layers causes a decrease in the radiation hardening after helium implantation, until the hardening becomes almost negligible for thicknesses of ~2.5 nm [85]. This was observed even for miscible systems such as Fe/W which are not able to retain layered structure after irradiation [100]. In conclusion, is interesting to note the case of Al/Nb [101] system, made up of two miscible elements which should intermix under radiation, but in fact retain the individual layered structure. This happens because, when irradiated, they form a hard and dense Nb_3Al intermetallic compound along the Al/Nb interface, which impedes extensive intermixing and but leads to radiation hardening particularly for small thickness layers. Thermal stability studies have revealed that [102–104] the first phase to form in this system should be $NbAl_3$, thus suggesting that the Nb_3Al phase is also more resistant to radiation.

2.5.3 Metal-Oxide Interfaces

Metal-oxide interfaces may be classified as hetero interfaces because of the vast difference in properties between metals and oxides in regards to crystal structure, surface energy, and atomic bonding characteristics (electron delocalization in metals vs mostly ionic and covalent for oxides) [105]. To maintain charge neutrality, the top surface an oxide can exhibit a range of different structures, including deviations from oxide stoichiometry [106], faceting, metallization, adsorption of charged species, and modification in the surface electronic structure [107]. These structures are often modified when a metal is bonded to the oxide [108]. This complexity constitutes a challenge when these systems are studied through simulations. Because of the lack of empirical potentials, metal/oxide interfaces are typically studied by means of DFT, which in turn limits the size of the systems to small cells [108]. In systems where there is a lattice mismatch between the constituents, the misfit dislocation structure must also be taken into account and only in few studies in literature have included electronic structure calculations [109–111].

One interfacial phenomenon which is crucially important to predict, is the enrichment/depletion of specific elements at interfaces because such a behavior can have deleterious effects on the properties of materials, such as embrittlement caused by Cr segregation at grain boundaries [112], or irradiation assisted stress corrosion cracking caused by the opposite phenomenon of Cr depletion at grain boundaries [113,114]. This elemental segregation occures when, under radiation, there is a preferential association of solute atoms with irradiation generated point defects and preferential interaction with interfaces, which cause a change of local chemistry (radiation-induced solute redistribution). This effect consists of either depletion or enrichment of solute atoms near interfaces [5,115,116]. In metal/oxide systems, the prediction of solute segregation to semi-coherent interfaces is very complex. In general, this phenomenon is typically governed by two competing factors, the chemical and the strain energy, both of which must be taken into account in order to predict solute segregation [117].

Recently, a series of papers by Choudhury et al. [108,117] have used DFT calculations to study the role of misfit dislocation in stabilizing the structure of a model Y_2O_3/Fe interface in the $[001]_{Fe}||[100]_{Y_2O_3}$ and $(010)_{Fe}||(011)_{YO}$ orientation relationship, shedding light on the critical role of misfit dislocations in stabilizing the interfacial structure in determining the interaction with defects and in solute segregation. First, it was noted that a misfit dislocation will not only be associated with a strain field, but it will also affect the local chemistry of the interface, by causing an imbalance in the Fe/O ratio affecting the electron transfer between the metal and the oxide. It is this initial chemical imbalance at the misfit dislocation that provides the driving force for the defect behavior at the interface [108]. Specifically, when a misfit dislocation resides in the Fe sublayer, the Fe/O ratio becomes >1 and some Fe atoms become instable at these sites because there are not enough oxygen atoms to accept their electrons. Stability can be restored by the introduction of defects, either oxygen interstitials or iron vacancies, in the misfit dislocation region. The concentration of the latter, regardless of the interstitial oxygen content can get to approximately ~0.5, a value which is orders of magnitude higher than the vacancies necessary to stabilize metal interfaces. The independence of the Fe vacancy concentration from the interstitial oxygen content can be understood by the fact that oxygen insertion, while restoring the chemical imbalance at the interface, will also introduce strain which can alleviated by Fe atoms removal. It should be noted that the tendency of coherent $\{100\}\langle 100\rangle_{Fe}||\{100\}\langle 100\rangle_{Y_2O_3}$ interfaces to form iron vacancies, close to the interface, was also validated through DFT calculation by other authors [118]. Thus, the point defect structure associated with misfit dislocation is determined by two competing energy terms, the strain energy and chemical energy, as shown in **Figure 2-17**

[108]. As the introduction of vacancies can also cause the Fe/O ratio to be < 1, the formation of FeO becomes possible, starting first at the misfit dislocation location and to then eventually extending to the rest of the interface.

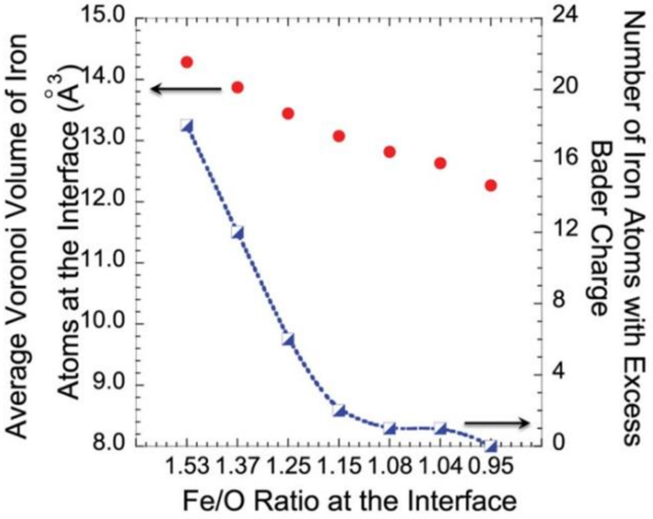

Figure 2-17: Plot of the average Voronoi volume[2] (vertical axis, left) and Bader charge[3] (vertical axis, right) as oxygen atoms are inserted at the $\{100\}\langle100\rangle_{Fe}||\{100\}\langle100\rangle_{Y_2O_3}$ interface. Increasing interstitial oxygen content restores the chemical imbalance at the interface however this also introduces strain into the system. A decrease in the Voronoi volume correlates with an increase in the strain energy of the system. Thus, introducing interstitial oxygen reduces the Voronoi volume, indicating that the strain energy of the system has increased with higher oxygen content (from Ref. [108]).

Finally, the local oxygen content (dramatically different at the misfit region of the interface as compared to the terraces [117]) coupled with oxide-forming tendency (governed by Ellingham diagram [119]) of the solute, govern the solute segregation to particular iron sites at the Fe/Y_2O_3 interface. At the terraces and in the absence of oxygen interstitials, elements such as Cr prefer to remain in the BCC iron matrix, as predicted by Hume-Rothery rules[4] [120]. Cr also has a BCC crystal structure and therefore does not segregate to the interface under these

---

[2] The average Voronoi volume of the iron atoms at the interface is a measure of the average free volume available at the interface [241].

[3] Number of electrons on the iron atoms compared to the iron atoms in unstrained bulk iron

[4] which describe the tendency of a solute to dissolve in a matrix based on the mismatch of crystal structures, atomic radius, electronegativity and valence between the solute and the solvent.

conditions. **Figure 2-18** effectively summarize the complex interplay between the strain and chemistry at the Fe/Y_2O_3 interface, on the segregation of a strong oxide former (Cr) and a weak oxide former (Ni), in three different scenarios: (i) perfect (no point defects) interface, (ii) Fe vacancy-stabilized structure interface, and (iii) combined Fe vacancy + oxygen interstitial-stabilized interface structure. Elements with a strong oxide forming tendency segregate at the interface in regions where the Fe/O ratio is low (misfit dislocations) and conversely are repelled under reducing conditions, when both Fe vacancies and interstitial oxygen are present in the misfit region. On the other hand, the segregation tendency within the terrace remains relatively unchanged within the three structures. Weak oxide forming elements show an opposite tendency, and prefer to segregate to the interface within the perfect and the Fe vacancy-stabilized interfaces and are repelled particularly from the misfit region under oxidizing conditions.

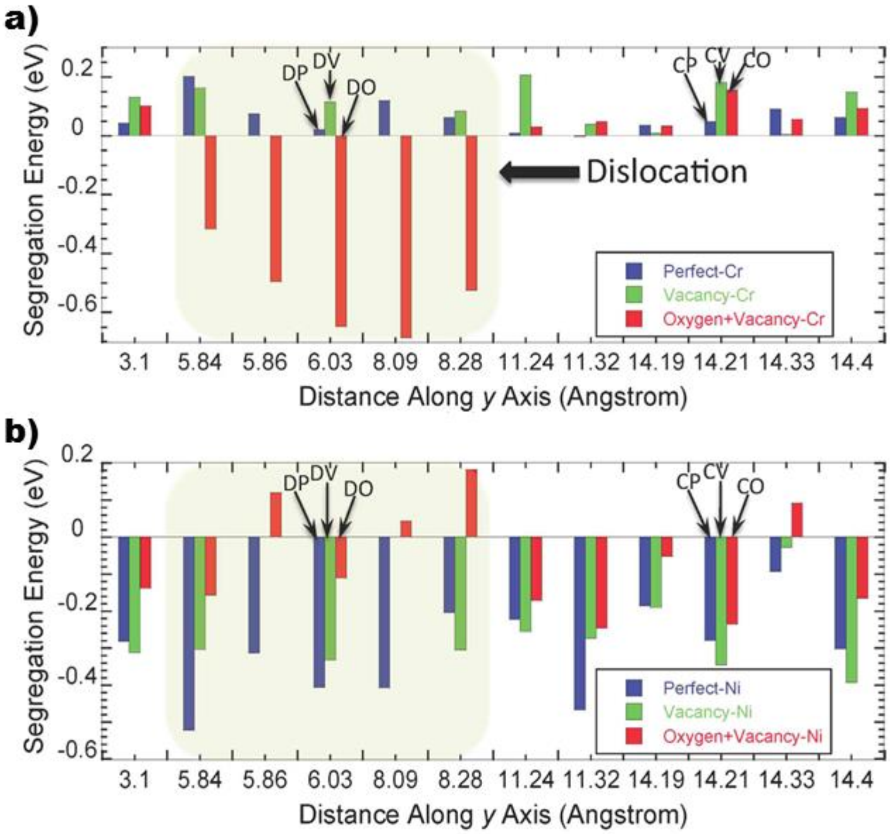

Figure 2-18: Spatial variation of Cr and Ni segregation energies within the dislocation and coherent regions. In all the figures, the shaded region represents the location of dislocation. Perfect interface (P), Fe vacancy-stabilized interface (V), and oxygen interstitial + Fe vacancy stabilized interfaces (O). Sites are labeled as DP, DV, DO and CP, CV, CO, respectively in the dislocation core (D) and coherent regions(C) of the interface (from Ref. [117]).

2.5.4 Properties and Radiation Response in ODS steels

One of the most practical, contemporary examples of the importance of the role of interfaces in enhancing radiation damage resistance is oxide dispersion strengthened (ODS) steels, which come under the broader category of the so-called nanostructured ferritic alloys (NFA) and sometimes referred to as such. Ferritic steels have limited high temperature mechanical properties and significant microstructural changes (grain growth, precipitates coarsening etc.) begin to occur at temperatures even below the operational temperatures of Gen IV nuclear reactors [121], where the conditions are further exacerbated by the radiation fields

[122,123]. One viable approach to control and mitigate these microstructural changes is to introduce a high density of trapping sites (or interfaces) for defects [121]. This is the basis for the development of ODS steels which consist of Y-Ti-O nanoprecipitate particles and is produced by mechanical alloying (M(A) [124,125]. This approach involves ball milling ferritic steel powders with Y_2O_3 powders. The energy introduced by the milling process solutionizes Y in the steel which then reprecipitates as nanoclusters of Y_2O_3 during subsequent high temperature consolidation and sintering treatments. Addition of Ti facilitates the decomposition of Y_2O_3 and its subsequent solutionizing, and results in the formation of Y-Ti-O nanoclusters rather than just those of Y_2O_3 [16,125–127]. This sequence of events was first characterized by Alinger et al. [125] using small angle neutron scattering (SANS) technique, however conflicting results have been reported regarding the role of titanium on the coarsening resistance of the nanoclusters at high temperature, with some researchers claiming that a higher Ti content makes the clusters resistant to coarsening [128], and others claiming that the coarsening properties are independent of the titanium content [129].

The nanoclusters are extremely beneficial in pinning grain boundaries during processing heat treatments limiting their size to a value typically less than 1 μm. At high temperatures these nanoclusters impede dislocation motion [130,131] thus improving creep resistance [127,132] as compared to conventional steels. From a radiation damage resistance standpoint, the interfaces between the nanoclusters and the steel matrix act as sites for defect recombination and can trap helium.

Several studies have shown that the oxide nanoparticles in ODS steel typically have sizes in the 2-50 nm [133] range and different chemistries, including $Y_2Ti_2O_7$, Y_2TiO_5, Y_2O_3, TiO_2 and Y-Ti-O non-stoichiometric oxides. Generally, the $Y_2Ti_2O_7$ phase is considered to have a cubic $Fd\bar{3}m$ structure [134,135] which can be ordered (pyrochlore) or disordered (fluorite) with respect to the cations. The Y_2TiO_5 phase is thought to be either orthorhombic or hexagonal [136,137], and Y_2O_3 has several polymorphs including those with cubic and monoclinic structures [138]. DFT simulations have confirmed that the $Y_2Ti_2O_7$-Fe interface can be Y/Ti-rich, stoichiometric, or O-rich, depending on the internal oxygen partial pressure and temperature [139]. **Figure 2-19** shows some of these precipitates in a 14 YWT ODS steel. More recently, APT has been used to identify a high population density of smaller sized (~2-5 nm) oxide nanoclusters of ODS steels, that could not be imaged by TEM [140]. **Figure 2-20** shows an APT reconstruction of these nanoscale precipitates in a 9%Cr ODS steel.

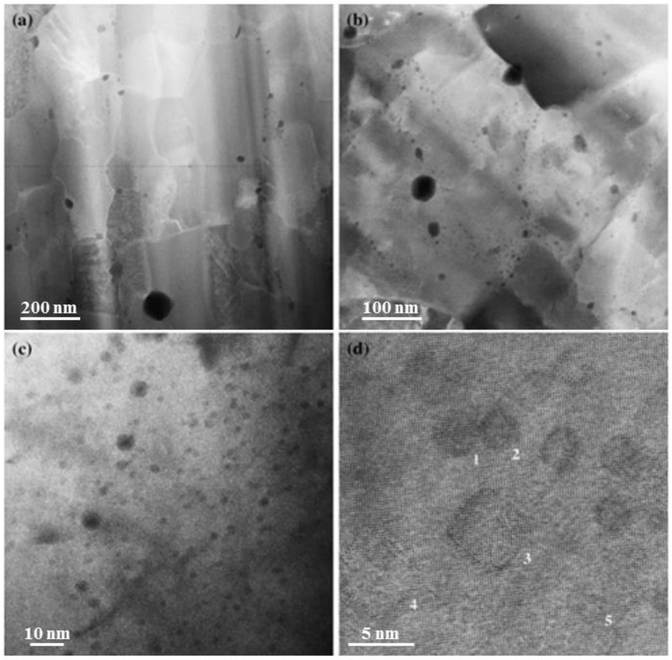

Figure 2-19: Microstructure of a 14 YWT ODS steel. Particles of different size (having a darker contrast with respect to the steel matrix) are observed in the matrix and along grain boundaries (from Ref. [133]).

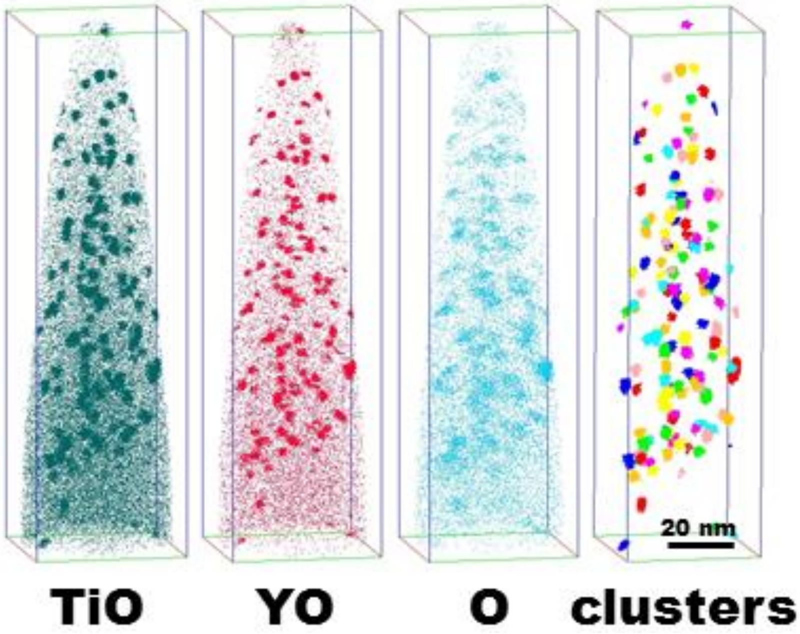

Figure 2-20: APT imaging of Y-Ti-O enriched nanoclusters in a 9%Cr-ODS steels showing TiO, YO, O nanoclusters (from Ref. [141]).

It is clear that the stability of the oxide nanoclusters is critically important to the high temperature strength and radiation damage resistance of ODS steels. Swenson at al. [142], in a review article on this subject, have reported how results on radiation response of ODS steels can vary depending on alloy composition, radiating species (protons, heavy ions, neutron), and temperature. Work by Certain [143] on a 14YWT ODS steel indicates that at cryogenic temperatures nanoclusters completely dissolve in the matrix when ion irradiated to 100 dpa using heavy ions. At such low temperatures and high dose rates, nanoclusters were unstable due to ballistic dissolution and the reduced energy for back-diffusion of ejected atoms to re-from the cluster. At intermediate temperatures, nanoclusters were present but many areas examined showed a highly reduced population of nanoclusters when imaged by energy filtered transmission electron microscopy (EFTEM). However, the APT technique which is especially conducive to studying small sized nanoclusters, showed no difference in the number density of nanoclusters between the unirradiated and irradiated samples in the intermediate temperature range to 100 dpa. For heavy ion irradiations conducted at high temperatures (450-600 °C), no discernable change in the cluster population was observed using both EFTEM and APT indicating sufficient thermal energy was available for back diffusion to restore nanocluster stability. Nanoclusters previously dissolved during low temperature irradiations, were also seen to precipitate back into the matrix after further exposure at high temperature. Dissolution of the precipitates at cryogenic temperature was confirmed also by He et al.[144].

Despite extensive research, important questions regarding the nanocluster chemistry, crystal structure, orientation relationship, and interfacial structure with respect to the matrix have not yet been fully addressed. In particular, the stability of the interface of the nanocluster and the matrix which plays a vital role in conferring radiation damage resistance warrants further study [16,145]. These issues are further complicated because of various ODS steel compositions investigated in literature, the variations in the processing and characterization techniques used, and the inherent challenges in studying very fine precipitates. Some studies have investigated the nanoclusters using the extraction replicas and high resolution STEM which allows for examinations without interference from the surrounding matrix [133], but concerns can potentially be raised about morphological and chemical relaxation of the nanoclusters. In conventional TEM and STEM imaging studies, on the other hand, concerns exist due to the thickness of TEM foils which can obscure nanocluster analysis (due to matrix effects) [146], further exacerbated by the potential presence of thin native oxide layers on both the sides of the foil. In a recent detailed HRSTEM study performed on a 14WYT ODS steel [133], the smallest nanoclusters (< 5nm in size) where determined to be coherent with the matrix, with truncated rhombic dodecahedron morphologies defined by {100} and {110} planes. Their structure, however, was determined to be amorphous. **Figure 2-21** show HRSTEM images of small (~2-5 nm) NCs in a 14YWT alloy.

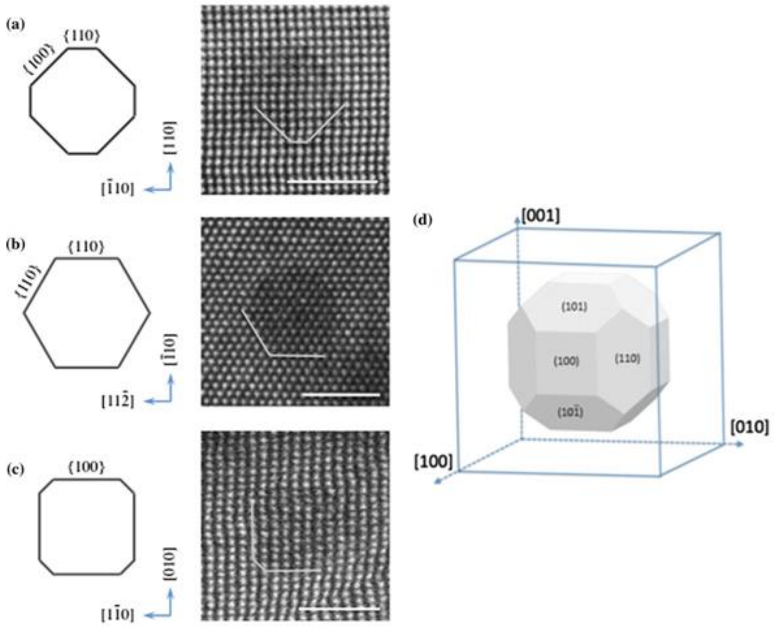

Figure 2-21: HRSTEM images of ultrafine Y-Ti-O nanoclusters (2 to 5 nm) in a 14YWT alloy, viewed along (a) <100>$_{Fe}$, (b) <111>$_{Fe}$ and (c) <110>$_{Fe}$. The shape of the cluster shown in (d) is inferred from the facets identified on the HRSTEM images (from Ref. [133]).

An interesting aspect of nanoclusters is their association with a large number of vacancies. Positron life-time spectroscopy has revealed for the first time the existence of vacancy clusters in a mechanically alloyed, hot extruded ODS steel [147] and later studies performed using a combination of *in situ* SANS and APT has provided compelling evidence of the existence of a large amount of vacancies in the nanoclusters, with their number density varying with annealing time and approaching the oxygen concentration [148]. These vacancies play an important role in the stabilization of the nanoclusters. The initial nucleation starts when oxygen atoms cluster with yttrium, titanium and vacancies, as vacancies have exceptional affinity to oxygen [149] (the oxygen vacancy binding energy can be as low as -1.5 eV [150]). Once an oxygen-vacancy pair has formed, the complex moves as a unit [151], restricting its diffusion.

The oxygen-vacancy pair is also prone to attract more oxygen-vacancy complexes, leading to a similar content of oxygen and vacancies in the nanocluster. Moreover, the presence of titanium is able to further increase the oxygen-vacancy binding energy to a value of -3.2 eV from that of oxygen in a defect free (and titanium free) iron lattice [150]. Given that yttrium has a higher affinity to oxygen than iron, its addition is also expected to lower the binding energy of oxygen in the nanocluster.

A fundamental factor governing the radiation stability of ODS steels is the interfacial structure and crystallographic coherency between the nanocluster and the surrounding matrix, which governs mechanical properties and radiation stability of the steel [152–154]. Several studies have focused on the coherency of nanoclusters with the ferritic matrix [128,146,155] and most have demonstrated coherent to semi-coherent interfaces [156]. As one of the focus areas of this thesis is the synthesis and radiation response of Y_2O_3/Fe interfaces, it is worth mentioning the works of Klimiankou et al.[157,158], in which for a ferritic-martensitic steel (without the addition of titanium), most of the small (<~10 nm) Y_2O_3 oxide particles show a $[110]_{Y_2O_3}||[111]_{FeCr}$ and $(1\bar{1}1)_{Y_2O_3}||(\bar{1}01)_{FeCr}$, correlation with the matrix as revealed by HRTEM imaging and analysis of FFT (Fast Fourier Transform, performed for determining atomic planes spacing using HRTEM) from these particles, as shown in **Figure 2-22**. In summary, the superior radiation resistance exhibited by ODS steels compared to conventional F/M steels is due to their inherently radiation resistant matrix and a very high number density of radiation induced defect sinks. Very high sink strengths are achieved by both reducing the grain size and the formation of fine nanoclusters in a steel matrix.

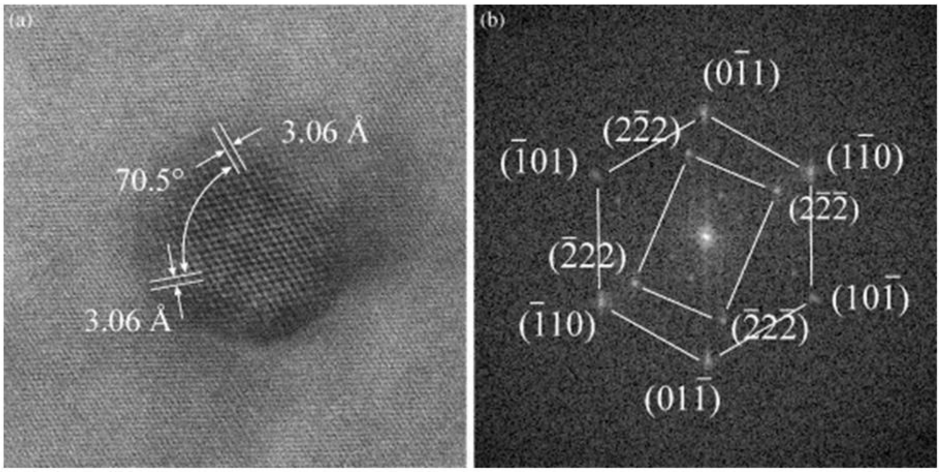

Figure 2-22: HRTEM studies: (a) micrograph of Y_2O_3 nanocluster with surrounded matrix and (b) FFT of the micrograph. Matrix is aligned on the [111] zone axis, while the FFT of the particles correspond to a [110] zone axis (from Ref. [157]).

2.5.5 He management in ODS steels and NFA

Synergistic TEM and APT studies have provided compelling evidence indicating that helium bubbles nucleate close to the cluster/matrix interface [159,160] in ODS steels. In particular, the work by Edmondson et al. [159] showed that after helium implantation at 400ºC to 6.75 x 10^{17} ions/cm^2, ~4.4% of the bubbles are located on coarse precipitates, ~12.2% on dislocations, ~14.4% at grain boundaries, ~48.6% at nanoclusters and the remaining in the matrix. In order to benchmark these experimental findings with models, DFT-based approaches have focused on the interaction between helium atoms and the metal/oxide interface in these alloys. DFT simulations have already shown that bulk oxides have a better ability to trap helium than the ferritic matrix [161,162] and **Figure 2-23** [139] succinctly illustrates the helium distribution in ODS steels and the events that can lead to bubble nucleation at the interface.

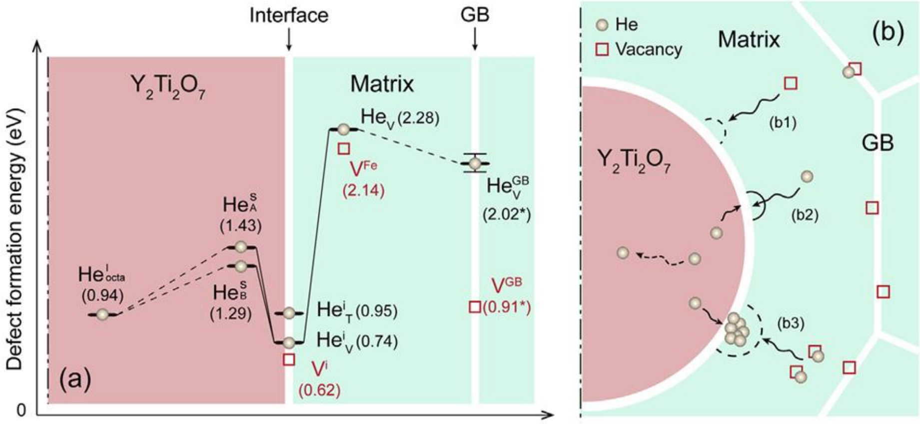

Figure 2-23: (a) Energies of formation of vacancies and helium trapping at various sites in ODS steels, including matrix, oxide, metal/oxide interface, and grain boundaries, and (b) schematic illustration of formation of interfacial helium bubbles in ODS steels. The superscript '*' refers to the DFT results available in the literature. A very high density of metal/oxide interface can reduce the amount of helium migrating on grain boundaries (from Ref. [139]).

Gan et al. have used DFT calculations for a 14WYT ODS steel [163], to elucidate the role of the nanoclusters in managing helium. Six types of reference structural units within the material were considered: (i) pure Fe (ii) Fe + vacancy, (iii) Fe+O: vacancy pair, (iv) Fe + O:vacancy pair + Ti (v) Fe + O:vacancy pair + 4Ti (vi) Fe + O:vacancy pair + 3Ti + Y, all representative of different environment in the ODS steel. These calculations showed that while a single vacancy is able to trap up to seven helium atoms, the energy cost for the helium bubble to grow increases in the presence of solute elements (titanium, yttrium or oxygen) in the reference unit. The number of helium atoms that can be trapped by a vacancy is reduced if the vacancy is pre-occupied by an oxygen atom and further reduced if titanium and yttrium are also present in the reference unit. Moreover, once a bubble has nucleated, other helium atoms tend to join, expanding its size along directions away from the solute atoms. Thus, while efficient in trapping helium at the metal/oxide interface, nanoclusters might also be effective in limiting the growth of these cavities, another theoretical confirmation of the fundamental role of these nanoscale features play in retarding the onset of swelling in irradiated materials.

CHAPTER 3

Experimental Methods

In this chapter, the main experimental techniques used in this research will be briefly described, along with the physical process underlying their functioning. The exact parameters used in the experiments will be provided in later sections.

3.1 Thin Film Depositions

3.1.1 Sputtering

Sputtering is the erosion of a material by the interaction with energetic positive ions. Usually, sputter deposition devices consist of a deposition chamber, a supply gas, pumps, a DC/RF voltage power supply, a quartz crystal for measuring film thickness, and target cathode for the deposition of the film. Deposition is performed at pressures typically lower than $2\text{x}10^{-6}$ Torr. A very common sputtering gas is argon, but sometimes a combination of gases may be used for reactive sputtering. When electrons are accelerated away from the target through the application of a DC voltage on the cathode target, they collide and strip electrons from molecules of the supply gas in the chamber, initiating and sustaining plasma. The now positively charged particles (ions) are attracted toward the cathode. From the collisions of the energetic positive charged ions of the plasma with the target, neutral species (atoms, clusters or molecules) are emitted from its surface which then deposit on the surface of the substrate. A schematic illustration of the process is shown in **Figure 3-1**. Modern sputter systems are typically equipped with magnets behind the target, for what is called magnetron sputtering. The magnetic field from the magnets confines the plasma in close proximity of the cathode and increases the deposition by intensifying ion bombardment. On the other hand, magnetic targets such as Fe cannot be effectively sputtered by magnetron sputtering unless very strong magnetic fields are used.

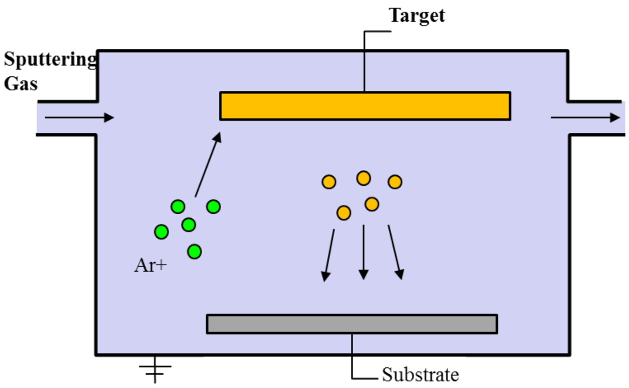

Figure 3-1: Schematic illustration of the DC sputtering process. The target is negatively polarized with a DC voltage. The electrons in the system are accelerated away from the target and collide with the molecules of the gas filling the chamber creating a plasma. The positively charged ions in the plasma then result in the sputtering of the target.

The application of a DC potential can be effectively employed for deposition from conductive targets, but when applied to nonconductive materials (e.g. oxides) charge build-up occurs on the target surface. This in turn causes the plasma to arc, suppressing the deposition process. Therefore, nonconductive targets are sputtered with RF sputtering system, where the polarity of the anode-cathode bias is varied at a high rate, thus avoiding the charge build-up. Usually, because of the low thermal conductivity of oxides, these targets are bonded to Cu backing plates as shown in **Figure 3-2** for the Y_2O_3 target used in part of the experiments in this study. The bonding process usually sets a limit to the power which can be applied to the target and the maximum power limits the maximum deposition rate in the process. Sputter deposition was employed to deposit thin films of Ti, TiO_2 and Y_2O_3, as described in **Chapter 4** and **Chapter 5**.

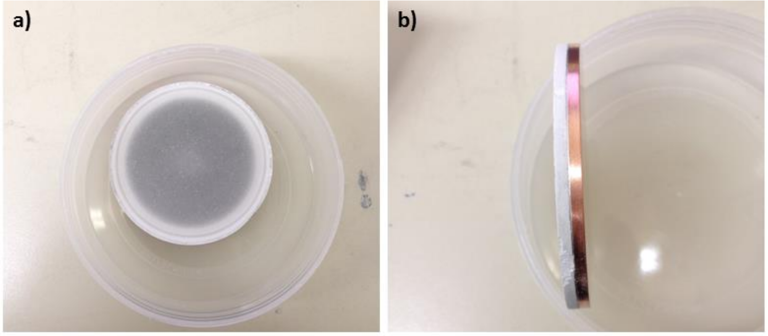

Figure 3-2: Y_2O_3 sputter target used in this research (a) front view (b) side view showing Cu backing plate.

3.1.2 Pulsed Laser Deposition

Similar to sputtering, in Pulsed Laser Deposition (PLD) atoms or molecules are transferred from a target onto a substrate to form a film. However, the particles are ablated from the target by means of a high energy-high repetition rate laser, instead of being sputtered by accelerating ions. **Figure 3-3** schematically illustrates a typical PLD system. In its basic configuration, a set of lenses focuses a high-power laser onto the target surface, which is the evaporation source. Most nonmetallic materials that are evaporated exhibit strong absorption in the ultraviolet spectral range between 200 and 400 nm. Because absorption coefficients typically tend to increase at the shorter wavelengths, reduced penetration depths are achieved. Therefore most lasers used in PLD use solid state Nd^{3+}:YAG (1064 nm) and are of the gas excimer type. The former can deliver 2 Joules pulse at a pulse repetition rate of ~ 30 Hz and the 1064 nm. The frequency is doubled twice and mixed so that outputs of 355 and 266 nm are produced. Although attenuated in power relative to the fundamental output they are sufficiently intense for PLD work. The absorbed beam energy is converted into thermal, chemical and mechanical energy, causing electronic excitation of target atoms, ablation and exfoliation of the surface, and plasma formation. Evaporants form a plume above the target consisting of a motley collection of energetic neutral atoms, molecules, ions, electrons, atom clusters, micron- sized particulates, and molten droplets. The plume is highly directional, i.e., $cos^n(\theta)$, where $8 < n < 12$, and its contents are propelled to the substrate where they condense to form a film. Gases such as O_2 and N_2 can be introduced in the chamber to promote surface reactions or maintain stoichiometry. In this research PLD was employed for the deposition of epitaxial Y_2O_3 (discussed in **Chapter 6** and the deposition of the Al_2O_3 coatings (discussed in **Chapter 7**).

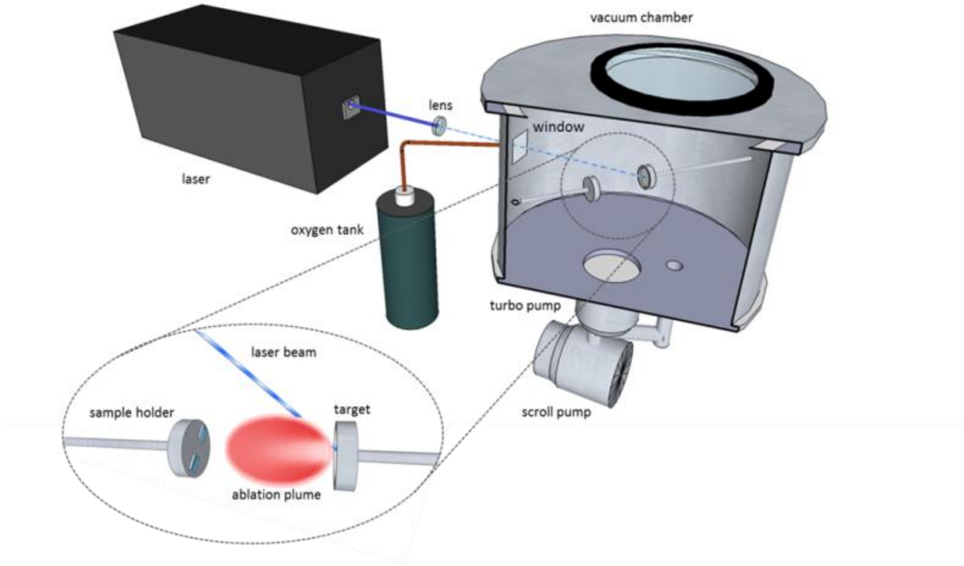

Figure 3-3: Schematic illustration of the Pulsed Laser Deposition (PLD) process.

3.1.3 Molecular Beam Epitaxy

Molecular beam epitaxy (MBE) is a single crystal growth technique which represents the state-of-the-art attainable for deposition process from the vapor phase [164]. One of its most notable aspects is the extremely low deposition rate that aids in the epitaxial growth of thin film, but the process requires very high vacuum or ultra-high vacuum systems (10^{-8}-10^{-12} Torr) to avoid incorporation of impurities into the growing film. A typical MBE system, schematically shown in **Figure 3-4**, has different independently controllable beams and film sources, and real time structural and chemical characterization capabilities. For solid sources, the deposited element is heated in separate Knudsen[5] effusion cells until it begins to sublime. The gaseous particles then condense on the substrate to form a thin film.

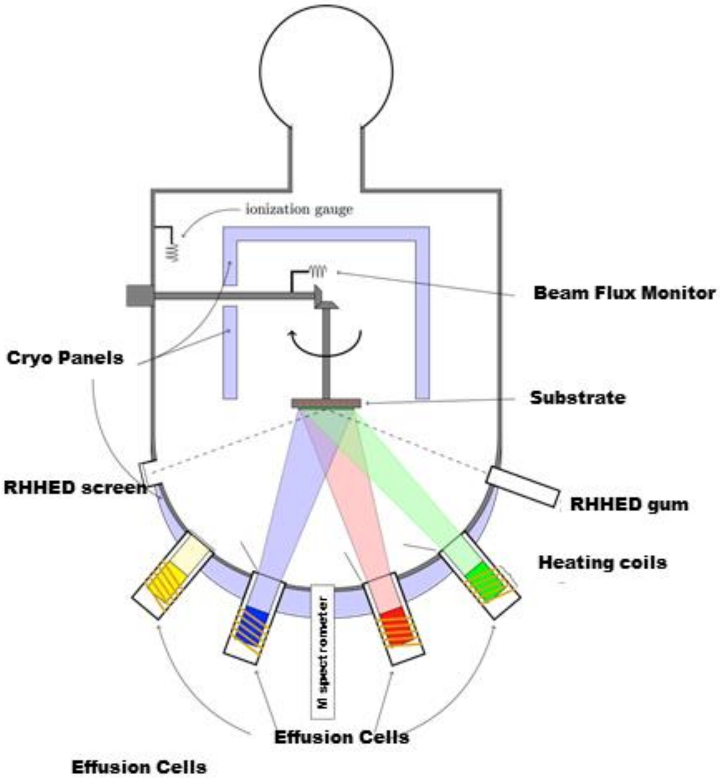

Figure 3-4: Schematic illustration of the Molecular Beam Epitaxy (MBE) deposition system.

The growth of the crystal is usually monitored through reflection high energy electron diffraction (RHEED) which is schematically shown in **Figure 3-5**. RHEED is the overwhelmingly preferred real time film characterization tool in MBE systems [165]. An

---

[5] Knudsen effusion cells typically contain a crucible (to host the evaporating material), a heating filaments, water cooling system and are often used as sources for relatively low partial pressure elementary sources, because it is easy to control the temperature of the evaporating material in Knudsen cells

electron beam is made incident on the surface of the sample with a grazing angle of few degrees, and with energies ranging between 5 to 100 KeV. These high energy electrons lead to a very large Ewald sphere (as in the case of TEM), and because the reciprocal lattice rods have a finite width due to crystal imperfections and thermal vibrations, the intersection with the Ewald sphere have a finite width, giving rise to streaked rather than spotty diffraction patterns. More spotted diffraction patterns occur for smooth thin films while more streaked patterns result from island or surface asperities. MBE was employed to deposit thin Fe films on Y_2O_3 grown by PLD on single crystal substrates of yttria-stabilized zirconia, as described in **Chapter 6**.

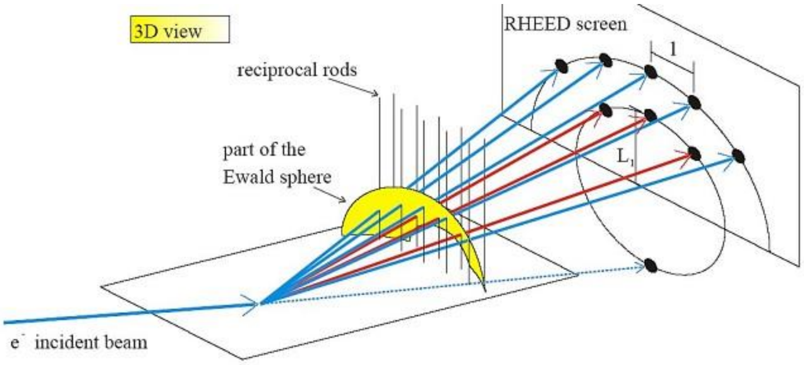

Figure 3-5: Schematic illustration of the principle underlying reflection high energy electron diffraction (RHEED).

3.1.4 Heavy Ions Irradiations

Heavy ion irradiations at high temperature were performed at Environmental and Molecular Science Laboratory (EMSL) at Pacific Northwest National Laboratory (PNNL), located in Pasco, WA, using 5 MeV Ni^{2+} ions. The EMSL facility is equipped with a 3 MV Tandem Pelletron accelerator, a Source of Negative Ions by cesium Sputtering (SNICS), injector and switching magnets. The beam is directed toward the stage, where the samples are irradiated, through sets electric steerers to steer the beam, quadrupole magnets to shape and focus the beam, Faraday cups to read its intensity, and scanners to allow effective monitoring of its shape. Images of the accelerator tank and a quadrupole are shown in **Figure 3-6**.

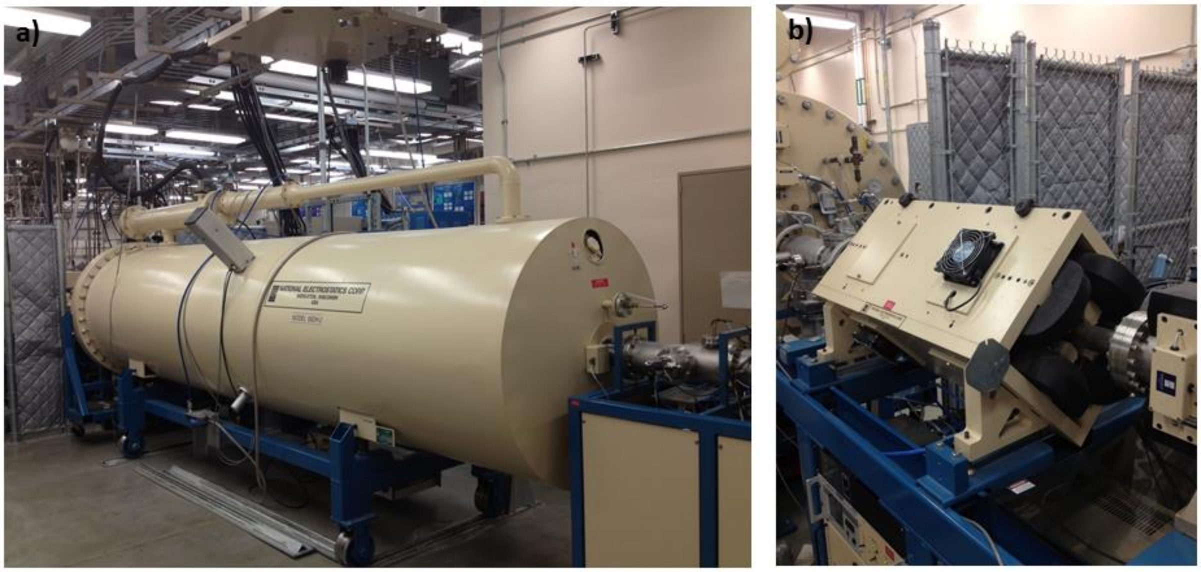

Figure 3-6: EMSL accelerator (a) accelerator tank (3MV Tandem Van Der Graaff accelerator) and (b) set of quadrupole magnets in the high energy part of the beam.

Negative ions of the irradiating species are produced from a metallic cathode. Cesium vapor from a cesium oven enters an enclosed region between a cooled cathode and a heated ionizing surface. Some of the cesium condenses on the front side of the cathode and some of it is ionized by the hot surface. The ionized cesium accelerates towards the cathode, sputtering particles from the cathode through the condensed cesium layer. Materials which preferentially sputter neutral or positive particles will pick up electrons as they pass through the condensed cesium layer [166], producing negative ions. Once the negative ions are formed, they are injected into the acceleration tank and accelerated by the positively charged terminal voltage, in the middle of the accelerator tank, between two grounded ends. In the tank the ions are forced to pass through a stripping chamber in which a gas or a thin foil collisionally removes electrons. The now positively charged beam experiences a second boost of acceleration from the positive terminal voltage (the reason why this kind of accelerator is called “Tandem accelerator”). The energy that can be reached by the ions is governed by the expression:

$$E = TV + Q \cdot TV \qquad \text{Equation 3-1}$$

where E is the energy of the ions in eV, Q is their charge state and TV is the terminal voltage in volts. With a charge state of +2, the terminal voltage has to be set up at 1.685 MV to achieve an energy of 5 MeV considering that the species are accelerated out of the cathode with approximately 50 KV.

The samples were mounted on a radiation stage that allows temperature control through heating with electron beam and cooling with liquid nitrogen flow in the cooling channel. A rastered beam, rather than defocused beam, was used because the rastered beam possesses uniform beam intensity. It must be noted lately the scientific community has questioned the use of rastered beams for irradiation studies, especially when neutron damage needs to be simulated, especially in regards to neutron-induced void swelling [167]. In this work we used a rastered beam (for the experiment described in **Chapter 4** and **Chapter 5)** in order to achieve uniform damage on the irradiated surface of the sample. The use of a rastered beam should not affect the observation made, as this study is focuses on ion beam intermixing phenomena, which are mainly ballistic and influenced by thermodynamics, and it is therefore very likely that the use of a defocused beam would have yielded very similar observations. For the experiments described in **Chapter 7**, a defocused beam was used instead.

The temperature of the samples was monitored using a K-type thermocouple, kept in contact with the surface of the sample, away from the region impinged by the beam. The damage exposures, expressed in dpa (displacements per atom) are calculated from ion fluences with the

Stopping Range of Ions in Matter (SRIM) software [19] according to the procedure described by Stoller et al. [20].

3.1.5 TEM samples preparation

Samples analyzed by TEM and STEM-EDS were prepared using the FIB lift-out technique. There are several reasons for which the FIB lift-out technique was preferred over other commonly used TEM sample preparation methods. First, when using the magnetic materials, significant electron aberrations during TEM and STEM investigation can occur and the use of FIB lift-out samples eliminates all noticeable aberrations caused by the magnetism of the samples. Moreover the differences in chemical nature of the substrate and the coatings would cause different dissolution rate between the two materials during sample preparation with for example electro-polishing. Finally, mechanical techniques were excluded to safeguard the integrity and the adhesion between the coating and the substrate. It must also be noted that FIB lift-outs allow for proper selection of the exaction area of interest in the sample to be analyzed. This way samples from the region of the interface between the substrate and the thin films could be lifted out, and select regions of interest of the samples could be chosen for analysis.

A Zeiss 1540XB Crossbeam FIB/SEM at the University of Madison-Wisconsin was used for this purpose. During the lift-out procedure, a thin cap of platinum was deposited on the surface of the sample, to avoid charging effects and to minimize gallium contamination (FIB uses gallium ions) in the region of interest. The material is removed from both the sides of the platinum cap, shaping a thin lamella (~2μm thick). Once the lamella is shaped, it can be cut free after one of its sides is welded with platinum to a needle. The lamella is then attached to a copper Omniprobe® Lift-Out Grid, specifically designed to house the TEM lamellas milled out by the

FIB system. These grids have a typical thickness of 25-30µm with a diameter of 3mm. Different posts are available to weld the lamellae on the grid and they fit standard TEM holders and provide a non-obscured view of the thin sections attached to the posts. For samples exposed to TEM in situ thermal treatment molybdenum FIB grids were used instead, to avoid partial evaporation of the copper grid at high temperature. **Figure 3-7** shows a schematic of TEM sample preparation steps via conventional FIB lift-out techniques.

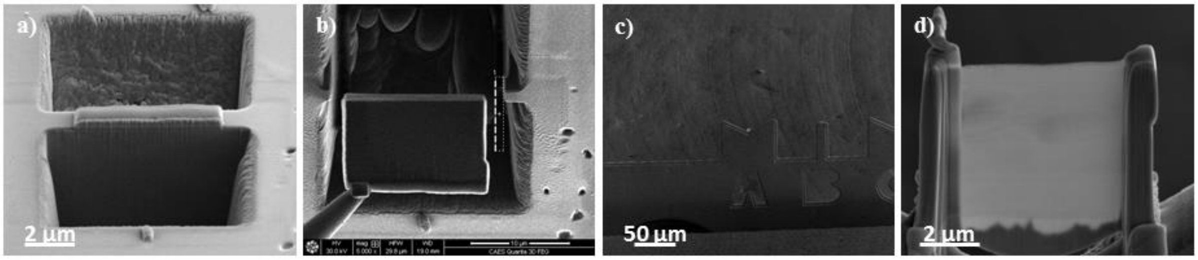

Figure 3-7: TEM sample preparation using conventional FIB lift-out techniques (a) deposition of Pt cap on top of the sample and shaping of the lamella (b) U-cut to release the lamella from the bulk sample (c) sample welded to Omniprobe grid, and (d) final thin sample.

Samples were mounted with a chevron instead or the normal 'flag' mount. The Chevron configuration, locks the lamella on both sides of the sample and this prevents the sample from warping or bending during thinning. Once the lamella is attached to the grid, it is thinned out through successive high energy (30KV) milling steps. At every step the current is reduced in order to minimize the damage caused to the samples by the gallium ion beam. Usually one or two final steps are performed at lower voltages (5KV and 2 KV) in order to obtain a flat and clean surface of the TEM sample. **Figure 3-7** (d) shows an electron transparent TEM sample mounted in Chevron position.

3.2 TEM and STEM imaging principles and microscopy observations

The Transmission Electron Microscope (TEM) consists of an electron gun, a set of lenses, detectors/screens, high vacuum column and a specimen holder. Usually a TEM is divided into three components: the illumination system, the objective lens/stage, and the imaging system. In the illumination system, electrons are emitted from the gun and transferred to the specimen though the condenser lenses. The beam can be directed on the sample in parallel, for TEM imaging and selected area diffraction (SAD), or as a convergent beam, used for scanning (STEM) imaging, analysis via x-ray and electron spectrometry, and convergent beam electron diffraction (CBED). At the center of the TEM, the objective lens and the specimen holder/stage system are a critical region where all of the beam-specimen interactions take place. Moreover, the various images and diffraction patterns (DP) are created and subsequently magnified for viewing and recording. The quality of the objective lens determines the quality of all the information of the specimen, thus the objective lens is the most important lens in the TEM. Finally, the imaging system uses several lenses to magnify the image or the DP produced by the objective lens and to focus these on the viewing screen or computer display via a detector CD, or TV camera.

The image formation mechanism in a TEM is complicated. Different mechanisms can be used to obtain an image from the specimen and each of these modes can provide different information about the specimen. In this work, the main TEM imaging technique used was High Resolution TEM (HR-TEM), which maximizes the useful detail in the image. With current state-of-the-art TEM, sub nanometers resolution are routinely achieved and, therefore, atomic resolution can be obtained from thin samples. STEM stands for Scanning Transmission Electron

Microscopy and implies a transmission electron microscopy performed with a scanned and focused beam [1]. In STEM a focused beam is scanned over a thin sample and the intensity of the transmitted electron signals are measured with different electron detectors. An image is built up point by point as in a conventional SEM. The essential difference though, is the extremely small size of the beam that is used. If x-ray or electron energy loss detectors are used, chemical analysis can be performed point by point. Usually STEM microscope uses a field emission electron gun, because only with this, a very small probe (less than 1 nm in diameter) with high currents can be delivered to the sample. Different types of detectors can be used to collect the electrons that have interacted with the specimen, hence different types of images can be created in a STEM system. Basic schematic of STEM imaging detectors are shown in **Figure 3-8**.

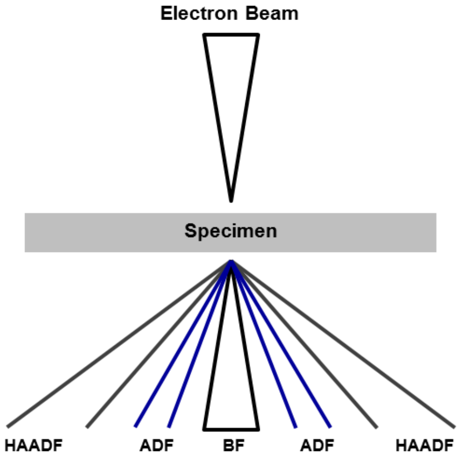

Figure 3-8: Bright Field (BF) detector are axial detectors which collect the electrons that are transmitted right through the sample, Dark Field (DF) detectors collect those electrons that are scattered at low angle and High Angle Annular Dark Field (HAADF) detectors collect those electrons that are scattered at high angle from the interaction with the sample.

The most important detectors are the Bright Field (BF) detectors, which are axial detectors and which the electrons that are transmitted right through the sample. Annular Dark Field (ADF) detectors, on the other hand, collect those electrons that are scattered at low angle, and High Angle Annular Dark Field (HAADF) detectors collect those electrons that are scattered at high angle from the interaction with the sample. Secondary Electron detectors can be added to form an SEM like image. Bright Field images are the images that most resemble conventional TEM images. ADF images show diffraction contrast because the strongly excited diffracted beams are detected. HAADF images show little to no diffraction contrast, since diffracted beams do not contribute to image formation, leaving only the thermal diffuse scattering to be recorded. HAADF images have atomic number contrast, since heavier elements will scatter electrons at higher angles. These images also do not show contrast reversal with changing focus and specimen thickness.

TEM samples were analyzed with a FEI Titan S-Twin D2080 transmission electron microscope (TEM) with an accelerating voltage of 200 KV. This microscope is equipped with EDAX energy dispersive x-ray spectroscopy (EDS) detector and spectrum image acquisition capabilities. During EDS spectra acquisition, beam drift was minimized to reduce position error over the duration of the scan. STEM investigations were performed using either high angle annular dark field (HAADF) or annular dark field (ADF) STEM imaging. The former provides for a strong Z-contrast imaging, and the latter provides for a stronger diffraction contrast. Quantification of the acquired spectra was performed using the FEI’s TEM Imaging and Analysis software (TIA). For the experiments described in **Chapter 6**, aberration corrected STEM techniques were used to image helium bubbles in the samples.

3.2.1 X-ray Diffraction

Ex-situ x ray diffraction (XRD) experiments were carried out with a Bruker D8 x-ray diffractometer using Cu-Kα radiation in order to identify the phases formed after irradiation in the experiments described in **Chapter 4, Chapter 5** and **Chapter 7.** A low angle incident beam (kept at 2°) was used to maximize the signal from the thin films.

3.2.2 Helium implantation

Helium implantations were performed with a scanning helium ion microscope (SHIM) on Y_2O_3/Fe interfaces to observe nucleation of helium bubbles (**Chapter 6**). A typical FIB microscope produces a gallium-ion beam that is finely focused and scanned across the sample for surface imaging and analysis, and, at high currents, for site-specific sputtering of materials. A helium-ion microscope (HIM) produces instead an intense beam of helium ions, formed by gas field-ionization at the apex of an atomically sharp tungsten tip. With the HIM, charged-particle-based surface imaging, analysis and nanofabrication with unprecedented spatial resolution topographic and compositional contrast is achievable. A notable aspect is that by rastering the helium beam, helium can be effectively implanted into the samples. Helium implantation was performed with a Zeiss ORION NanoFab at QB3's Biomolecular Nanotechnology Center (BNC) at the University of California Berkeley, using 25 KeV helium ions. Several implantations were performed and it was daunting task to optimize the deposition parameters. It was observed in fact that with relatively thick (~ 100nm) samples, the effects of sputtering and re-deposition on the surface of the TEM samples combined with the presence of massive radiation damage, caused a deterioration of the sample's microstructure that made microscopy observation extremely challenging, even after further FIB thinning of the TEM lamellas. Therefore, thin samples (thickness <70 nm) were utilized for the implantations. Thinner samples allow a reduction in the effects of sputtering and re-deposition on the lamella, and have a net effect of lowering the damage dose delivered to the sample.

CHAPTER 4

Irradiation-induced Intermixing Effects at the Interfaces of Titanium and Titanium- dioxide Thin Films and Fe-12%Cr Substrate

This chapter is aimed at examining the irradiation-induced morphological and compositional evolution at the interfaces between a Fe-12%Cr ferritic alloy substrate and thin films of a metal (titanium) and its oxide (titanium-dioxide), in order to study elemental diffusion at interfaces and chromium segregation in metal/oxide bilayers. Irradiations were performed with 5MeV Ni^{2+} ions at 300˚C and 500˚C. The results show that although the metal/oxide system undergoes phase transformations (in the oxide) after high temperature exposure and radiation, no intermixed phases are formed between the substrate and the thin film and a clear and defined interface was still visible in STEM after irradiation at 500°C. Therefore, as expected the metal/oxide system resists radiation and high temperature intermixing more efficiently than the metal/metal interface. Moreover, at high temperature, chromium diffuses from the substrate to sub-stoichiometric regions of the oxide. This observation has important implications on the behavior of ODS steels and NFAs, as the Cr spatial distribution in the alloy plays a fundamental role in its corrosion resistance.

4.1 Experimental Details

The substrate used for this work was Fe-12%Cr binary alloy, with a simplified composition representative of a widely used class of ferritic steels. The detailed composition of the substrate model alloy is shown in **Table 3**.

Table 3. Chemical composition (in wt.%) of Fe12%Cr binary alloy substrate in wt.% (Fe balance).

	C	Si	Mn	P	S	Ni	Cr	Co	Ti	O	N	Al
wt.%	0.009	0.02	<0.01	0.015	0.002	<0.01	12.02	<0.01	<0.01	0.27	<0.001	0.014

Substrate samples sectioned to dimensions of 20 mm x3 mm in width were progressively ground and finally mirror polished with 0.5 µm diamond paste, rinsed in water, acetone, ethanol, and plasma cleaned prior to thin film deposition. Titanium thin films were deposited with a DC sputterer using pure titanium (99.99% purity) sputter cathodes. The depositions were performed at a base pressure of less than $2x10^{-6}$ Torr. Argon was used as a sputtering gas and the chamber pressure was maintained at 1.8 mTorr during deposition. Titanium-dioxide film depositions were performed using an RF sputter deposition system and titanium dioxide (99.9% purity) sputter cathodes. The base pressure for deposition was less than $2x10^{-6}$ Torr. Argon inlet pressure of 1 mTorr was employed for these depositions.

4.1.1 Heavy Ion Irradiation

As mentioned in **Section 3.1.4** the samples were irradiated using 5 MeV Ni^{2+} ions at the EMSL facility at PNNL. The temperatures for irradiation were 300°C and 500°C and the base pressure during radiation was in the 10^{-7} Torr range. The ion beam was rastered over an irradiated area of 3x3 mm^2, and this allowed for irradiation of selected regions of the sample, while also providing for neighboring regions (referred to as thermally exposed) that are not irradiated but experienced identical thermal effects as the irradiated regions. **Figure 4-1** shows the experimental arrangement of the samples on the stage.

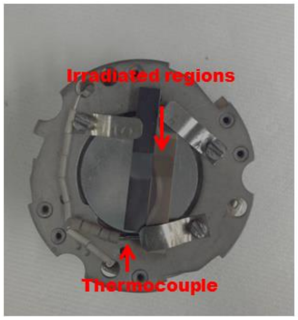

Figure 4-1 Experimental arrangement of the samples on the stage for 5 MeV Ni^{2+} ion irradiation, showing the irradiated regions. The neighboring regions were not irradiated but experienced the same thermal history.

The damage levels, expressed in dpa (displacements per atom) were calculated from ion fluences with the Stopping Range of Ions in Matter (SRIM) software [19] according to the procedure described by Stoller *et al.* [20] with displacement energies of 40 eV for Fe and Cr, 30 for Ti, and 28 for O. Irradiation was performed to a dose of 8.74×10^{16} ions/cm^2 and this corresponds to a damage of approximately 35 dpa at the substrate/thin film interface on the iron side and leads to a nickel peak concentration of ~1.8 atomic % at a depth of more than 1.5 μm underneath the interface. The temperature of the samples was monitored using a K-type thermocouple that was kept in contact with the surface of the sample, but away from the region impinged by the beam. **Figure 4-2** shows the damage and nickel concentration profiles for the Fe-12%Cr-Ti sample as determined using SRIM calculations. Profiles for the Fe-12%Cr-TiO_2 samples were similar, although a slightly lower damage level was reached in the oxide thin film, as compared to the metal thin film.

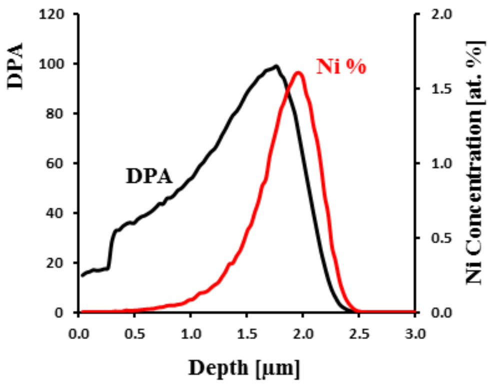

Figure 4-2: SRIM plots comparing the damage profile with the implanted Ni-atom profile for the Ti coated samples. The energy of the ions was chosen to be 5 MeV in order to minimize the concentration of the Ni atoms implanted near the interfacial region.

TEM sample preparation, microscopy characterization and x-ray diffraction analysis were described previously in **Sections 3.1.5** and **3.2.1**.

4.2 Results and Discussion

4.2.1 Titanium Thin Films

The BF/DF TEM images and a diffraction pattern of the as-deposited titanium thin film are shown in **Figure 4-3**. The film exhibits a columnar grain structure (typically observed for metallic thin films deposited by sputtering at low temperature) that grow through the entire thickness of the film [165]. STEM-EDS line scans across the interface of these samples showed a clearly defined interface with no intermixing between the substrate and the thin film (not shown).

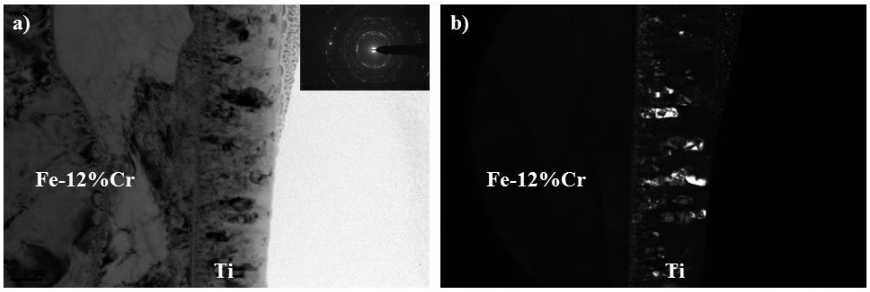

Figure 4-3: TEM BF/DF analysis of the as-deposited titanium film on Fe-12%Cr substrate, (a) BF image and diffraction pattern and (b) DF image.

In order to characterize the structure of the films and evaluate intermixing effects between the substrate and the thin film on a nanometer scale, STEM-EDS analysis was performed. **Figure 4-4** shows typical composition profiles for Fe, Cr and Ti for the 300˚C experiment for the irradiated and the thermally exposed conditions.

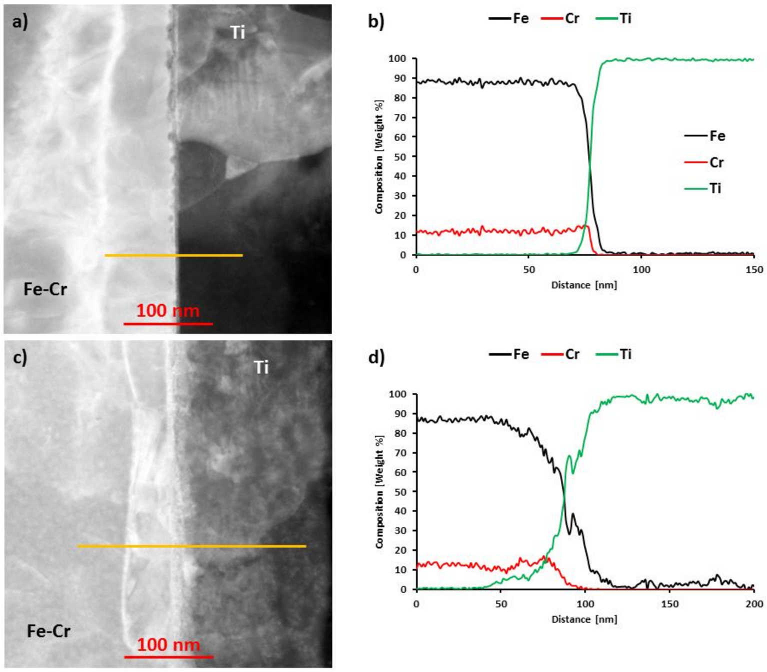

Figure 4-4: STEM-EDS elemental concentrations profiles across the Fe-12%Cr substrate - Ti thin film interface in the thermally exposed and irradiated regions at 300˚C. (a and b) thermally exposed region (c and d) irradiated region. Compositional line scans were acquired along the orange line indicated in the ADF images.

Comparing the elemental compositional profiles for the two conditions, it is evident that irradiation significantly enhanced the interdiffusion between the Ti film and the Fe-Cr substrate, across the interface. In order to quantify the intermixing between the substrate and the film for the irradiated and thermally exposed regions, the interdiffusion coefficient was calculated analogous to the diffusion process between two semi-infinite solids. In the quantification process, in order to obtain elemental composition ranging between 0 and 100%, iron and chromium concentrations were summed up. Starting with Fick's second law, the solution for the concentration in the case of a bilayered system can be fitted by an error function (and its complement), which is also the solution of the equation in the case of a semi-infinite source:

$$C(x,t) = \frac{C_0}{2} erf\left(\frac{(x - x_0)}{\sqrt{4\widetilde{D}t}}\right) \qquad \text{Equation 4-1}$$

where $C(x,t)$ is the concentration profile of the diffusing atoms, erf is the error function, C_0 is the initial concentration, x_0 is the center of the mixing profile, $\widetilde{D}$ is the interdiffusion coefficient, and t is the exposure time. The experimental profiles were interpolated by integral fitting of the functions representing the elemental compositions, following the approach outlined in literature [21]. The relevant parameters to perform the fit are x_0 and $\sqrt{4\widetilde{D}t}$. Other parameters were used in the fitting process but they serve only to shift and scale the functions along the y-axis and therefore do not represent any physical phenomena. **Figure 4-5** shows typical composition profiles for Ti and Fe+Cr in the 300˚C experiment for the titanium coated samples. The interdiffusion coefficients calculated and averaged for five separate line scans were determined to be $(4.09\pm0.31)\text{x}10^{-18}\text{cm}^2/\text{s}$ and $(9.02+1.37)\text{x}10^{-16}\text{cm}^2/\text{s}$ in the thermally exposed and irradiated samples, respectively. As can be seen, irradiation caused an increase in the interdiffusion coefficient by a factor greater than 20. Also, because ion beam mixing is a symmetrical process

[22], the interdiffusion coefficients calculated from the compositional profiles of Ti and Fe+Cr are equal, within the experimental error.

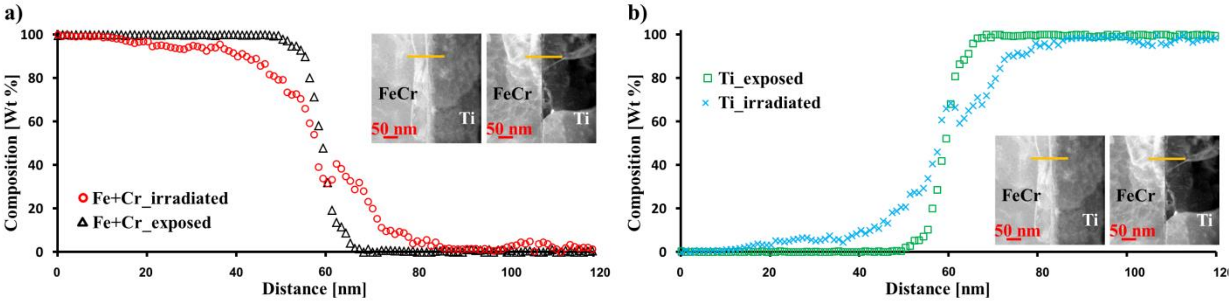

Figure 4-5: STEM-EDS elemental concentration profiles across the Fe-12%Cr substrate - Ti thin film interface in the thermally exposed and irradiated regions at 300˚C, (a) Fe+Cr profile (b) Ti profile. Insets represent the ADF STEM images of the thermally exposed (left image) and irradiated exposed (right image) regions. Compositional line scans were acquired along the orange line indicated in the ADF images.

STEM-EDS analysis was performed on the thermally exposed and irradiated regions of the samples irradiated at 500˚C, and typical line scans are shown in **Figure 4-6**. At this temperature thermal effects are expected to play a more dominant role in the evolution of the system, because of the high chemical affinity between iron and titanium due to the large negative enthalpy of mixing ($\Delta H_{Fe\text{-}Ti}$=-25 KJ/mol as calculated by the Miedema's model [168]). As can be seen from **Figure 4-6** (a) and (b) thermal exposure alone results in the formation of a wide *interdiffusion region* (~340 nm) between the substrate and the thin film, with a reaction layer consistent in composition with Fe_2Ti intermetallic phase. In this region, spikes in the iron and titanium concentrations suggest the formation of nanoscale precipitates enriched in titanium and depleted in iron, relative to the reaction layer matrix composition. These precipitates are speculated to be FeTi intermetallic compounds. The deviation of the observed composition from the one expected for FeTi may be due to the juxtaposition of the nanoprecipitate dispersion and the matrix material, both of which contribute to the measured EDS signal even in such high resolution analysis. These two phases are the only equilibrium intermetallic compounds between Fe and Ti, as dictated by the Fe-Ti equilibrium phase diagram [169]. As shown in **Figure 4-6** (c) and (d), irradiation enhances the spatial extent of the intermixed layer (~490nm), and additionally promotes diffusion of Cr from the substrate into this region. In both the irradiated and thermally exposed regions, chromium concentration was found to be higher at the substrate-thin film interface, as compared to the substrate matrix composition.

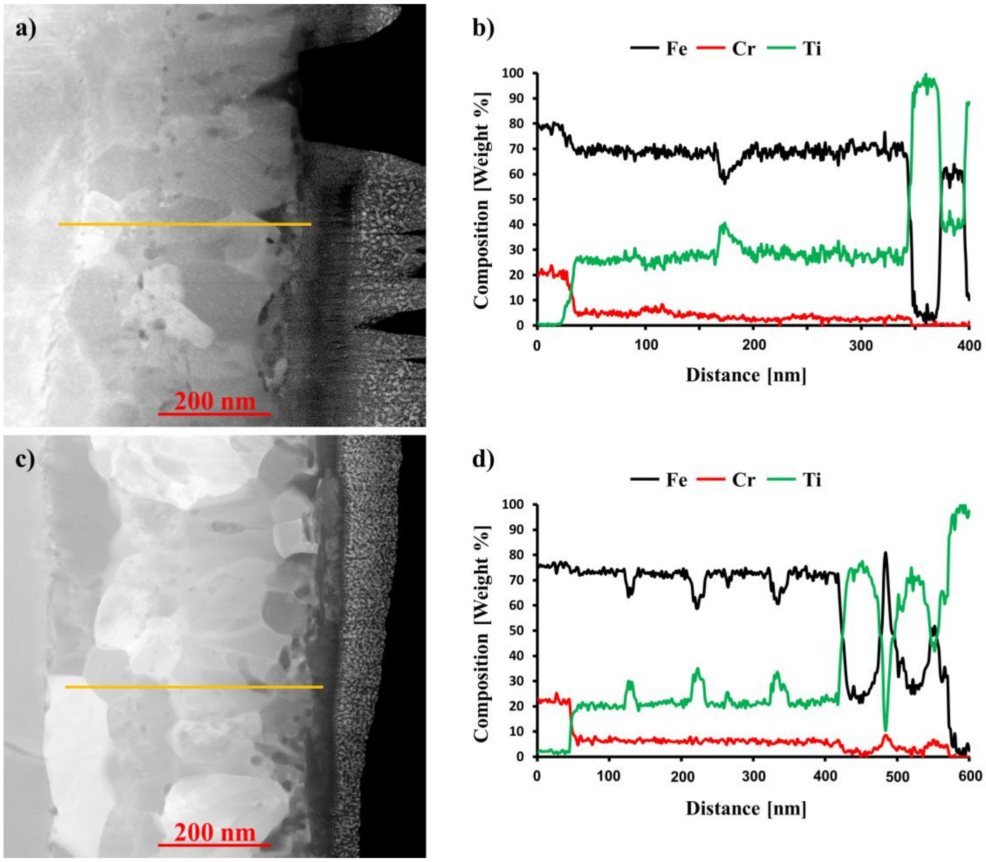

Figure 4-6: STEM-EDS analysis of the interface between the Ti film and the substrate after 500˚C irradiations. (a and b) STEM image and EDS line profile for the thermally exposed region (c and d) STEM image and EDS line profile for the irradiated regions. Compositional line scans were acquired along the orange line indicated in the ADF images.

To identify the phases formed in the near-surface regions of the film-substrate system, XRD analysis was performed on the samples and the results are shown in **Figure 4-7**. As can be seen, after both thermal exposure and irradiation the peaks corresponding to Fe_2Ti are clearly observed. Moreover, irradiation causes a slight shift of the Fe_2Ti peaks toward higher 2θ angles, which indicates a reduction (relaxation) of the lattice parameter for this phase after irradiation.

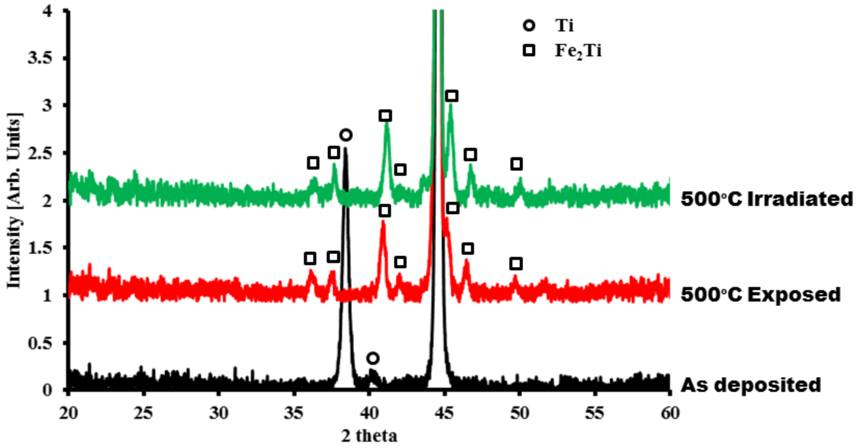

Figure 4-7: XRD patterns of the titanium thin film deposited sample on Fe-12%Cr substrate in the as- deposited condition, thermally exposed and irradiated regions at 500°C. After thermal exposure and irradiation, the peaks corresponding to Fe_2Ti phase are observed. The peak close to 2θ=45° is due to the substrate.

Previous studies on irradiation stability of Fe/Ti multilayers, performed at room temperature, have observed the formation of a solid solution and amorphous compounds [170–172]. Intermixing studies performed at temperature ranges comparable to our study have observed the formation first of a Fe-Ti solid solution, followed by the precipitation of FeTi intermetallic compound [173–175]. The difference observed in our experiments (formation of Fe_2Ti layer along with, possibly, nanometer sized FeTi precipitates) is speculated to be due the difference in the relative Fe/Ti compositions between the cited studies (Fe/Ti ~1) and our experiment (Fe>>Ti).

4.2.2 Titanium Oxide Thin Films

The as-deposited titanium-dioxide films were amorphous. A BF-TEM micrograph of the as-deposited film is shown in **Figure 4-8**, along with its diffuse ring diffraction pattern indicating its amorphous nature. STEM-EDS line scans acquired across the interface of this sample showed a clear, well-defined interface and no appreciable intermixing between the substrate and the film (not shown).

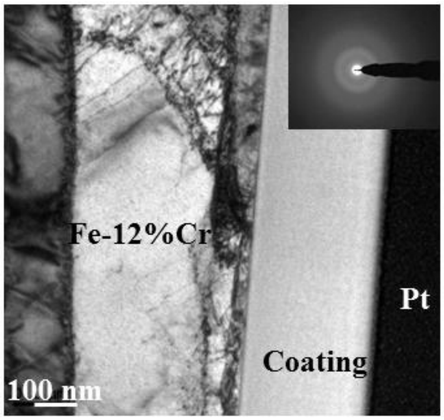

Figure 4-8: TEM-BF image of titanium-dioxide thin film deposited on Fe-12%Cr substrate. The diffraction pattern for the film (inset) shows diffuse rings typical of amorphous phase.

Figure 4-9 shows the STEM-EDS analysis of the samples irradiated at 300°C for the irradiated and thermally exposed regions along with the ensuing composition profiles determined using the procedure described earlier for the Ti-films. The length-scales for intermixing for the TiO_2-film are shown in **Figure 4-9** and are significantly smaller than the ones observed earlier for Ti films (**Figure 4-5**). Irradiation had a less significant effect on the interdiffusion between the substrate and the film. Quantitative analysis of the substrate-thin film interdiffusion coefficient indicates an increase by a factor of 1.2, from $(5.97\pm0.28)\ \mathrm{x}10^{-18}\mathrm{cm}^2/\mathrm{s}$ in the thermally exposed region to (7.11±0.34) x 10^{-18}cm^2/s for the irradiated region, indicating that the metal-oxide bi-layered system is more resistant to intermixing than the metal-metal system.

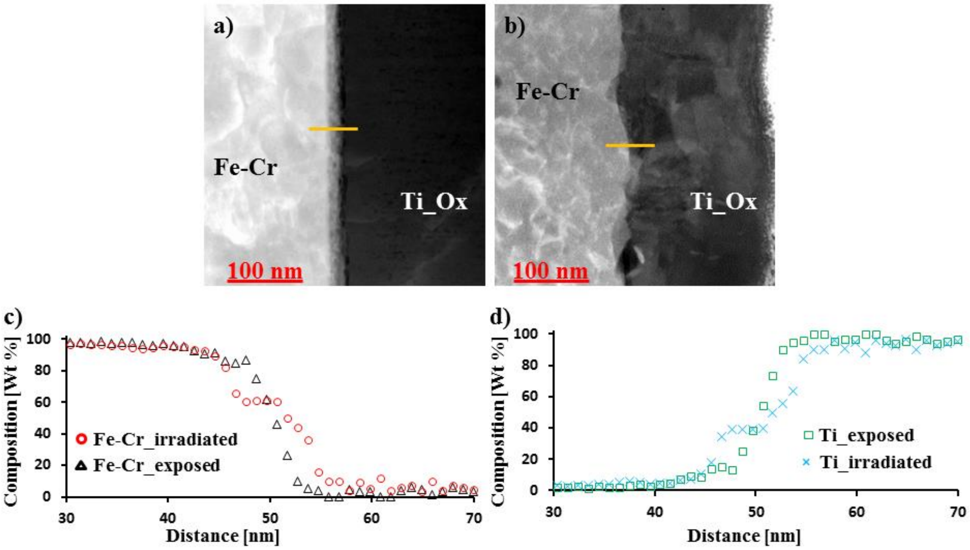

Figure 4-9: Experimental elemental profiles across the substrate-thin film interface in the thermally exposed and irradiated regions of the TiO_2 film samples at 300˚C. (a and b) Fe+Cr profile (c and d) Ti+O profile. Insets represent the ADF STEM images of the thermally exposed (left image) and irradiated exposed (right image) regions. Compositional line scans were acquired along the orange line indicated in the ADF images.

Analysis of the samples irradiated at 500ºC was complicated due to the evolution of various phases in the TiO_2 film in both the irradiated and thermally exposed regions. **Figure 4-10** shows the results of XRD analysis indicating phase evolution in the TiO_2 film. The XRD pattern for the as-deposited film does not indicate any crystalline peak confirming its amorphous nature. This is consistent with the observations made in **Figure 4-8**. After thermal exposure at 300°C, XRD results reveal that the amorphous TiO_2 film transforms to crystalline anatase TiO_2. There are three stoichiometric polymorph of TiO_2: rutile, anatase and brookite. Rutile is the stable phase, anatase and brookite are metastable, with brookite in particular difficult to synthesize and less often studied [176]. The transformation to crystalline anatase, observed upon thermal exposure at 300°C, may be explained taking into consideration the densities of anatase and rutile, which are 3.894 g/cm^3 and 4.250 g/cm^3 respectively [176]. The amorphous thin film is expected to have a lower density. Therefore the formation of rutile from an amorphous matrix would mean a greater densification and hence anatase may be favored to form from the standpoint of elastic energy considerations.

On the other hand, irradiation at 300°C results in the formation of an oxygen deficient Ti_2O_3 phase. After thermal exposure at 500°C, the TiO_2 anatase phase was detected along with other sub-stoichiometric phases of titanium dioxide. For films irradiated at 500°C, Ti_2O_3 was the predominant phase. Based on these observations, irradiation appears to promote the formation of the sub-stoichiometric Ti_2O_3 phase. We note here, that for films irradiated at 300°C, and those thermally exposed as well irradiated at 500°C, a peak positioned at a 2θ angle of 26.3° could not be uniquely assigned to any specific oxide phases of titanium dioxide.

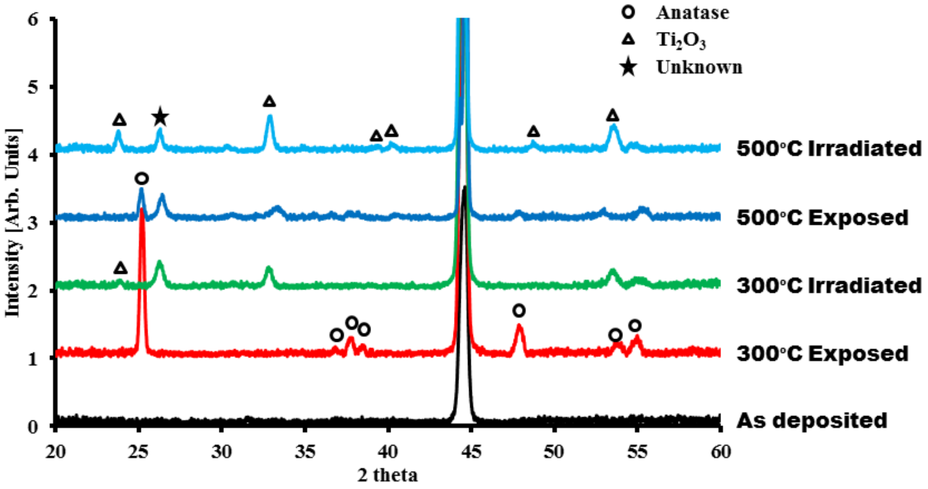

Figure 4-10: XRD patterns of samples of TiO_2 thin film deposited on Fe-12%Cr substrate samples. Upon exposure at 300°C the initially amorphous coating crystallizes in the anatase form of TiO_2, however irradiation appears to promote the formation of Ti_2O_3 phase.

In the 500°C thermally exposed regions, STEM-EDS examination indicated that Cr diffusion had occurred in some grains of the TiO_2 film while other grains were devoid of Cr diffusion. Therefore grains with and without Cr diffusion were selectively analyzed by TEM to identify the phases constituting these grains. Phase identification in TEM relies on the acquisition of multiple diffraction patterns using multiple zone axis. When these diffraction patterns are acquired, their respective angles can be determined by recording the TEM holder positions. The procedure of calculating the angle between two different zone axis is shown in **Figure 4-11**.

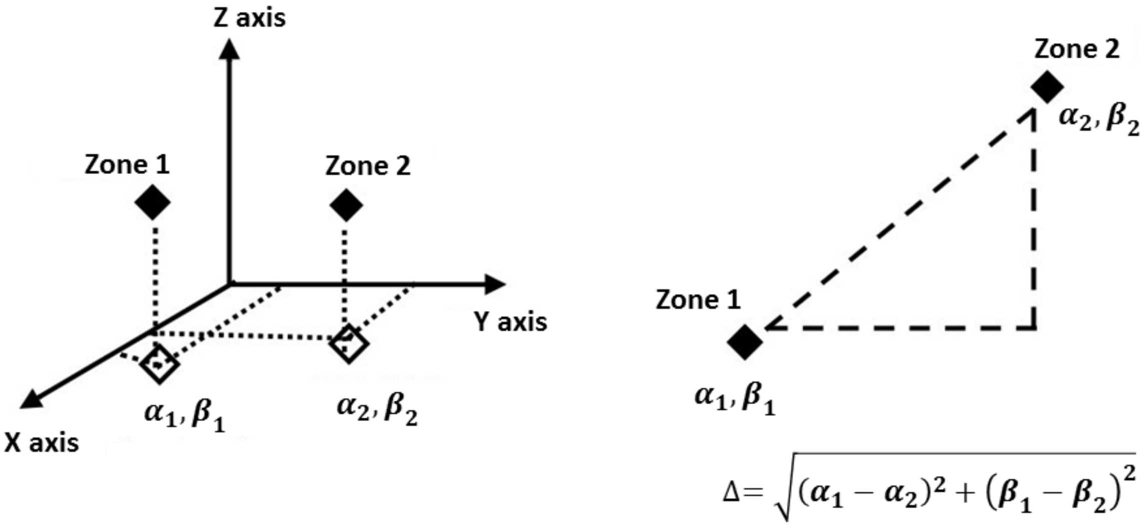

Figure 4-11: Calculation of the tilting angle Δ between two zone axis (adapted from Ref. [177]).

The angle between two zone axes is the distance between the two zones in the 2-D (*X*, *Y*) axis, projected by three-dimensional (3-D) coordinates. The distance or angle between the two zones can be calculated by using the Pythagorean relationship as:

$$\Delta = \sqrt{(\alpha_1 - \alpha_2)^2 + (\beta_1 - \beta_2)^2} \qquad \text{Equation 4-2}$$

Where Δ is the angle between the two zone axes, and α_i and β_i are the coordinates of the i-th zone axis, as recorded during the TEM observation. The measured values can then be compared to the theoretical values as obtained by the stereographic projection of potential phases [177] (in this case Ti_4O_7, Ti_2O_3, Ti_3O_5, TiO, anatase and rutile were chosen as possible candidates). **Figure 4-12** shows TEM and STEM micrographs, along with EDS line scans, of two different grains, one in which chromium diffusion was observed and one in which it was absent.

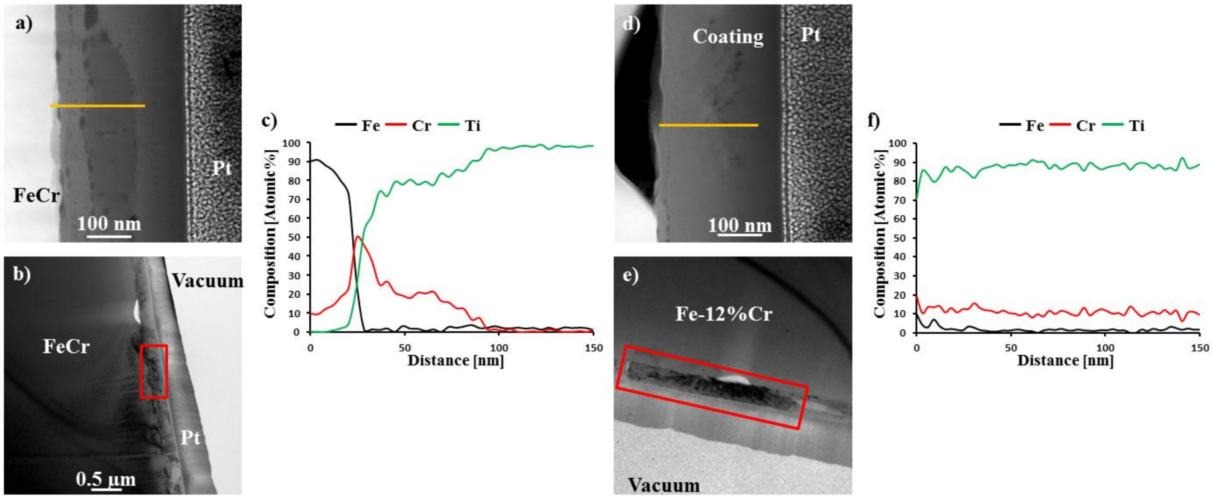

Figure 4-12: Phase identification in the TiO_2 film in the thermally exposed region after 500°C experiment (a-c) STEM, TEM and EDS line scan of the grain in which chromium diffusion was not observed (d-f) STEM, TEM and EDS line scan of the grain in which chromium diffusion was observed. The analyzed grains are encompassed in the red rectangle. Oxygen was excluded from the quantification.

Figure 4-13 shows the phase identification performed on the grain in which Cr diffusion was not observed. First, a zone axis compatible with the [100] zone axis of anatase was acquired and then the analyzed grain was tilted following one Kikuchi line (the tilting direction is represented by a dashed white line in **Figure 4-13**) until the next zone axis appeared. DPs were acquired sequentially and compared with simulated DPs (shown as superimposed red dots in

Figure 10 (b) – (e)). The following zone axes match well the$[50\bar{1}]$, the $[20\bar{1}]$ and the $[10\bar{1}]$ zone axes of anatase. The experimentally determined angles between the $[100]$ zone axis and the following angles, namely 26.39°, 51° and 66.9° degrees, which are very consistent with the ones expected theoretically for anatase, which are 26.7°, 51.5° and 68.31°, respectively According to this analysis, this grain can be identified as TiO_2-anatase phase.

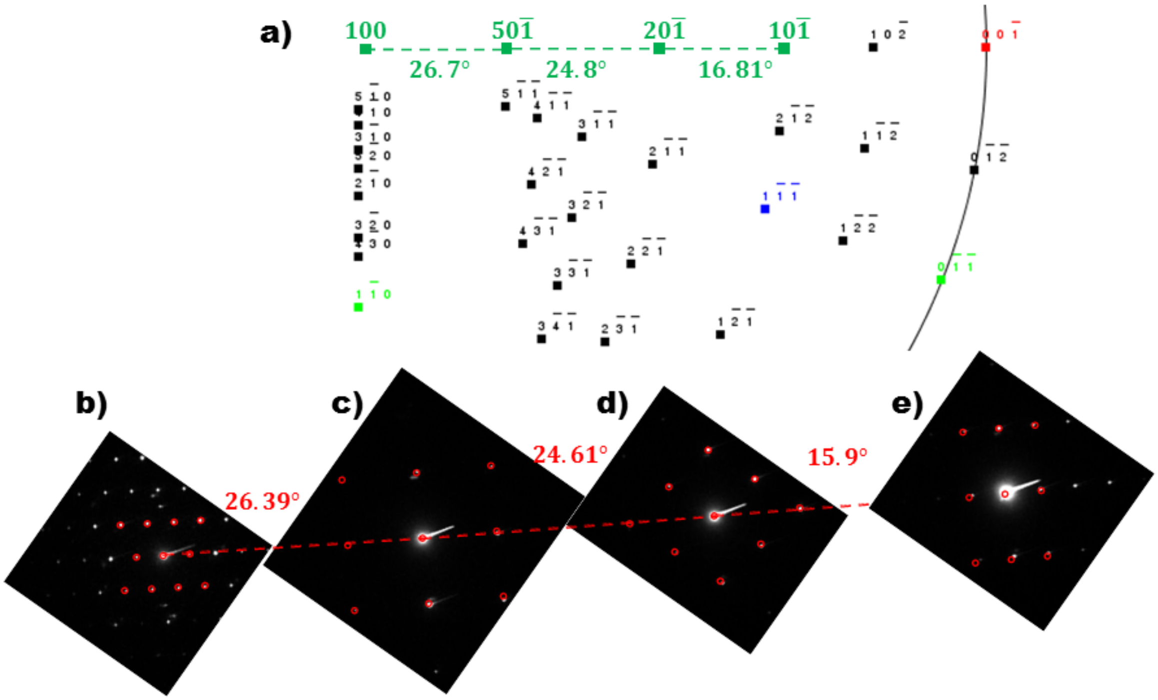

Figure 4-13: Phase identification in the TiO_2 film in the thermally exposed region after 500°C experiment (a) stereographic projection of anatase (b-e) diffraction patterns acquired to perform the phase analysis. Red dots correspond to simulated spots.

Figure 4-14 shows the phase identification performed on a neighboring grain in which chromium diffusion was observed. Successful phase identification in this Cr-diffused grain was not achieved as the zone axes acquired could not be uniquely matched to any of the possible phases hypothesized. It was however confirmed that this grain was not anatase or rutile. The zone axes shown in **Figure 4-14** are compatible with the (b) [210], (c) $[42\bar{1}]$, (d) [541] and (e) [120] zone axis of Ti_2O_3. Simulated DPs (red dots) for the Ti_2O_3 structure are superimposed on the experimentally obtained data. Dashed red line indicates the direction, in the reciprocal space followed while tilting the specimen to acquire the different DPs. A portion of the stereographic projection of Ti_2O_3 is also shown for reference. Angles between the [120], the $[42\bar{1}]$ and the [210] zone axis were measured to be 37.64° and 58.93°, respectively and are consistent with theoretical values of 37.34° and 60°, respectively for Ti_2O_3. Angles between the $[42\bar{1}]$, the $[54\bar{1}]$ and the [120] zone axis are 16.88° and 67.67° which also compare well to the theoretical values of 17.48° and 66.58°, respectively, for Ti_2O_3. It must be noted however that following the Kikuchi lines connecting the [210] zone axis to the [120] zone axis, a zone axis that did not match the expected [110] for Ti_2O_3 was noted. Thus the Ti_2O_3 phase was identified in the Cr-diffused grain with a high degree of certainty. It was however confirmed that this grain was not either TiO_2 anatase or rutile phase. Because anatase and rutile are the only two stoichiometric phases of titanium dioxide stable in this temperature range, we can conclude that the identified phase must be a sub-stoichiometric form of titanium dioxide.

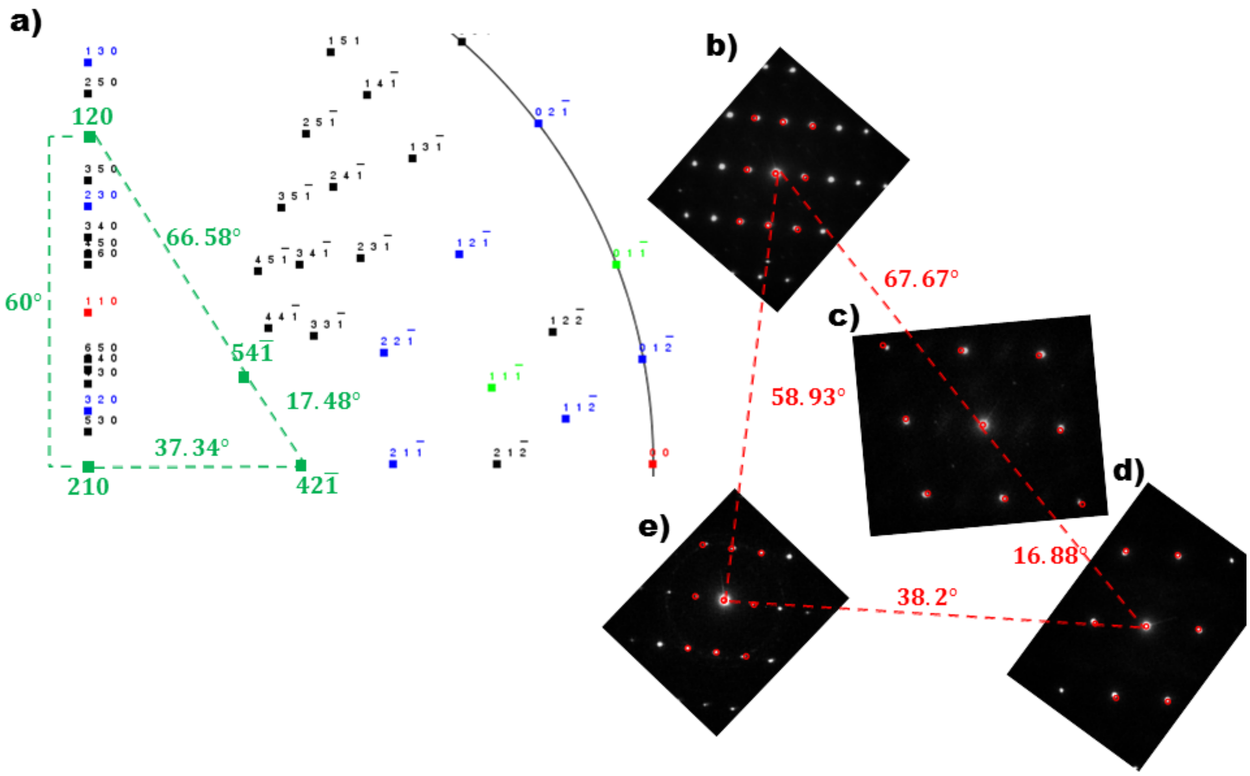

Figure 4-14: Phase identification in the TiO_2 film in the thermally exposed region after 500°C experiment (a) stereographic projection of Ti_2O_3 (b-e) diffraction patterns acquired to perform the phase analysis. Red dots correspond to simulated spots.

It is worth noting that in **Figure 4-12**, enrichment of Cr at the substrate-thin film interface was observed. This was not observed in the entire film, but only in small regions. It is likely that this selective enrichment of Cr in certain regions of the interface will be influenced by the relative orientation (or misalignment angle) between grains of the substrate and the grains of the film, similar to what is observed for grain boundaries in steels [47].

It is interesting to note that diffusion of Cr from a FeCr thin film into a TiO_2 thin film, after thermal exposure and irradiation with nickel ions at the same temperature (500ºC), has been previously observed by Xu et al. [112], where diffusion of Cr inside titania was correlated with the presence of an oxygen deficient phase of TiO_{2-x}. Our observations are consistent with these results. Regarding the mechanism for Cr diffusion into this oxygen- deficient phase, there are a few possible mechanisms: (i) interstitial diffusion after Cr has dissolved substitutionally, (ii) diffusion of Cr along grain boundaries, which provide fast diffusion pathways in the oxide, and (iii) diffusion through vacancy exchange mechanism into the oxide. Following the reasoning in ref. [112], the third mechanism is deemed to be the most likely. Cr diffusion is observed after thermal exposure, where interstitials are unlikely to be present, and the Cr distribution appears to be homogenous in the TiO_{2-x} phase and no enrichment is found on film's grain boundaries.

Finally **Figure 4-15** shows results of STEM-EDS analysis of samples irradiated at 500°C.

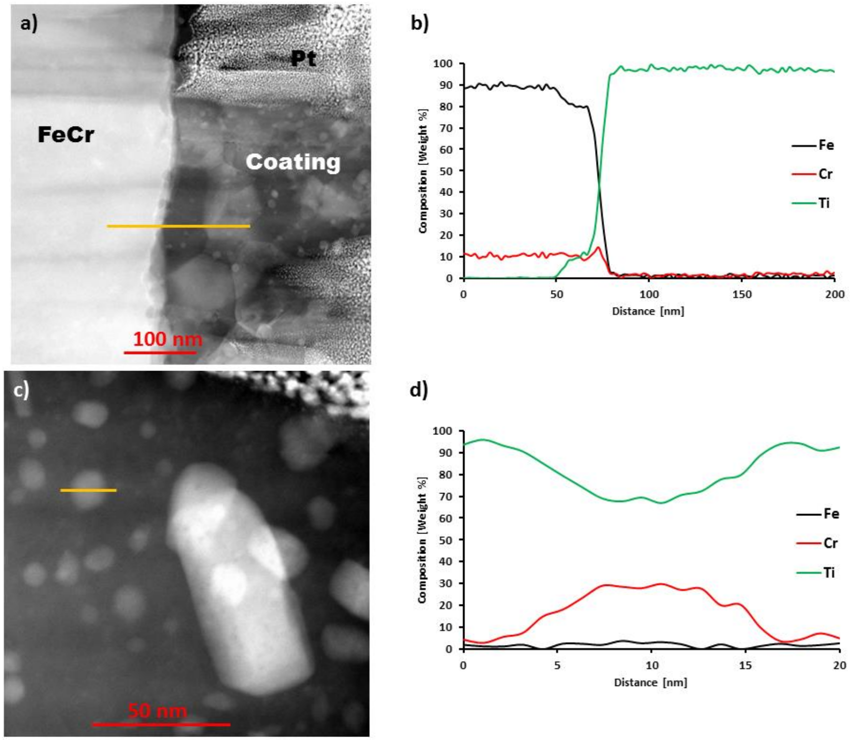

Figure 4-15: Experimental elemental profiles across the substrate-thin film interface in the TiO_2 thin film samples irradiated at 500°C (a and b) profile across the interface and (c and d) Cr-rich precipitates formed within the Ti-oxide coating. Oxygen was excluded from the quantification process.

As can be seen, the substrate thin film interface is still intact. However, Cr-rich precipitates (as shown in **Figure 4-15** (c and d)) were observed within the oxide. Although Cr diffusion was observed even in thermally exposed samples, radiation clearly facilitates the formation of Cr-enriched precipitates. A phase identification of these ultra-fine precipitates was attempted. However, due to their small size (< 20 nm) a fully accurate characterization was difficult. To better understand their composition, EDS point scans were performed on relatively larger precipitates (~20 nm) and from region of the Ti_2O_3 matrix surrounding it. A consistent reduction of the relative oxygen concentration in the EDS spectra in regions of these precipitate was observed. If the particle was an oxide phase of chromium, it would be expected to be Cr_2O_3, CrO, CrO_2, CrO_3, or CrO_5. Of these oxides, Cr_2O_3 should maintain the amount of oxygen in EDS spectra similar to the surrounding matrix (made up of Ti_2O_3), and only CrO would cause a reduction; however CrO dissolves at 300˚C. Therefore a reduction in the amount of oxygen in regions of these precipitates might be due to these precipitates being made up of pure chromium and not chromium oxide.

4.3 Conclusions

Film-substrate interface mixing effects in titanium and titanium dioxide thin films deposited on Fe-12%Cr alloy substrate due to 5 MeV Ni^{2+} ion irradiations at 300˚C and 500˚C have been investigated at nanometer length scales by using STEM-EDS, TEM and XRD techniques. Radiation-induced effects were isolated from purely thermal effects by also examining regions of samples that were not irradiated but experienced the same thermal history. At 300˚C, irradiation enhanced the extent of mixing between titanium and the alloy substrate, but the effect was not as pronounced for the titanium dioxide thin films. At 500˚C, an intermixed reaction layer consisting of Fe_2Ti intermetallic phase was observed for both thermally exposed and irradiated Ti-film samples, with irradiation enhancing Cr diffusion into the intermixed region. For the titanium dioxide film, irradiation had a marginal effect in enhancing mixing at

300˚C, but at 500˚C enhanced diffusion of Cr inside sub-stoichiometric regions of the oxide thin films was observed. Irradiation promoted the formation of Cr-rich nanoprecipitates in the oxide and a phase transformation in the film from anatase TiO_2 to the Ti_2O_3 phase.

CHAPTER 5

Stability and intermixing effects at the interface of Fe-12%Cr alloy and thin films of yttrium and yttrium oxide

This chapter is aimed at examining irradiation-induced morphological and compositional evolution, at the interface between a metallic substrate (Fe-12%Cr) and thin films yttrium oxide (Y_2O_3). Irradiations were performed with 5MeV Ni^{2+} ions at 300˚C, 500˚C and 700˚C. One of the outcomes of these experiments is that they shed light on the stability of interfaces between oxide nanoparticles and the ferritic steel matrix under radiation in oxide dispersion strengthened (ODS) steels. The results show that after high temperature exposure Cr diffuses to the metal/oxide interface, with the diffused Cr concentration increasing with increasing the temperature. After radiation, an amorphous intermixed region between the substrate and the thin film is observed. Additionally irradiation induced the formation of nanoscale intermetallic precipitates at the interface and grain growth in the oxide thin film.

5.1 Experimental Details

5.1.1 Sample preparation and thin film deposition

A Fe-12 wt. % Cr model alloy was used as a substrate for thin film deposition. This model alloy with its simplified chemistry precludes the formation of multiple phases as may be the case in multi-component alloy substrates. The composition of the model alloy was shown previously in **Table 3**.

Substrate samples sectioned to dimensions of 20 mm x3 mm in width were mirror polished with 0.5 µm diamond paste, rinsed in water, acetone, ethanol, and plasma cleaned prior to thin film deposition. Yttrium-oxide film depositions were performed using an RF sputter deposition system. The base pressure for deposition was less than 2x10^{-6} Torr. Argon inlet pressure of 1 mTorr was employed for deposition. A deposition rate of 0.1~Å/s was achieved.

5.1.2 Heavy Ion Irradiation

The samples were irradiated at the Environmental and Molecular Science Laboratory (EMSL) at Pacific Northwest National Laboratory (PNNL) using 5 MeV Ni^{2+} ions. The temperatures for irradiation were 300°C, 500°C and 700°C and the base pressure during radiation was in the 10^{-7} Torr range. The ion beam was rastered over an irradiated area of 3x3 mm^2, and this allowed for irradiation of selected regions of the sample, while also providing for neighboring regions that were not irradiated but experienced identical thermal effects as the irradiated regions. We refer to these regions as *thermally exposed* and *irradiation exposed*, respectively, in the text. The materials were irradiated to a dose of 8.74x10^{6} ions/cm^2 and the damage exposures, expressed in dpa (displacements per atom) were calculated from ion fluences with the Stopping Range of Ions in Matter (SRIM) software [19] according to the procedure described by Stoller *et al.* [20] with displacement energies of 40 eV for Fe and Cr, 25 for Y and 28 for O. The temperature of the samples was monitored using a K-type thermocouple that was kept in contact with the surface of the sample, but away from the region impinged by the beam. **Figure 5-1** shows the damage and nickel concentration profiles as determined by the SRIM calculation.

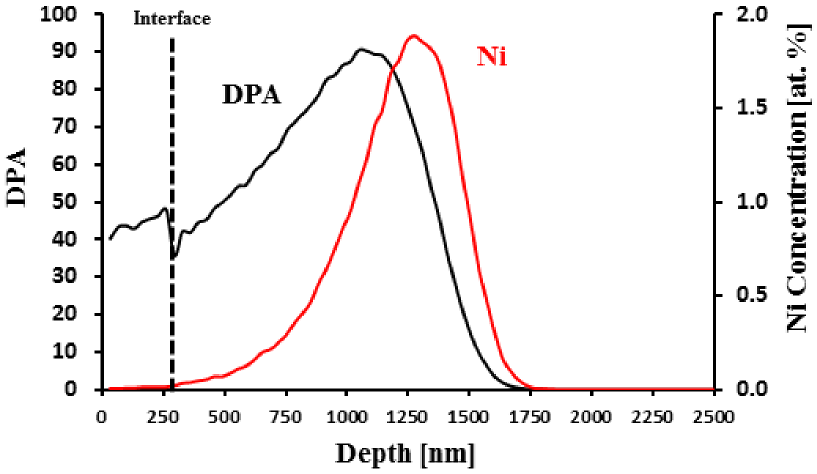

Figure 5-1: calculated SRIM damage and implantation profile for Ni into Y_2O_3/Fe-12%Cr bi-layers.

5.1.3 TEM sample preparation and samples characterization

TEM samples were prepared with conventional focused ion beam (FIB) technique and were analyzed by a FEI Titan S-Twin D2080 with an accelerating voltage of 200 KV. This microscope is equipped with EDAX energy dispersive x-ray spectroscopy (EDS) detector and spectrum image acquisition and quantification of acquired spectra was performed using FEI's TEM Imaging and Analysis software (TIA). Oxygen was excluded from the quantification process as EDS is not ideal for oxygen quantification. Beam drift was minimized to reduce position error over the duration of the scan. STEM investigations were performed using both high angle annular dark field (HAADF) and annular dark field (ADF) STEM imaging. The former provides a stronger Z-contrast (atomic number contrast), the latter a stronger diffraction contrast.

In-situ annealing was performed with a sample heating holder from Hummingbird Scientific. An as deposited sample was heated from room temperature (RT) to 400ºC, cooled to RT at the end of one experiment session, then in a later experiment, heated up to 500ºC and cooled to RT. EDS line scans were performed at RT after the annealed sample was placed into a different TEM holder (double tilt holder from Gatan).

Ex-situ x ray diffraction (XRD) experiments were carried out with a Bruker D8 x-ray diffractometer using Cu-Kα radiation in order to identify the phases formed after both thermal exposure and irradiation. A low angle (incident beam was kept at 2°) was used to maximize the signal from the thin films. Spectra were collected from the as-deposited thin film samples, as well as the thermally exposed and the irradiated regions of the samples.

5.2 Results and Discussion

The Bright Field (BF) and Dark Field (DF) TEM images and the diffraction pattern of the as-deposited yttrium oxide thin film are shown in **Figure 5-2**. The coating grows on the ferritic substrate with a nanocrystalline structure, with an average grain size of ~20 nm. The diffraction pattern, shown in the inset of **Figure 5-2** (a), confirms this observation. In the DP, the dominant internal ring corresponds to planes with a d spacing of 0.321 nm, slightly higher (~4%) than to the expected d spacing of 0.306 nm for {222} planes in cubic Y_2O_3. A very thin (~5nm) interlayer, showing a different contrast, is present between the thin film and the substrate. As expected for the low deposition temperature, the coating in the as-deposited condition exhibits porosity and voids [165]. STEM-EDS line scans across the interface of these samples showed a clearly defined interface with no intermixing between the substrate and the film (see **Figure 5-6** (a)).

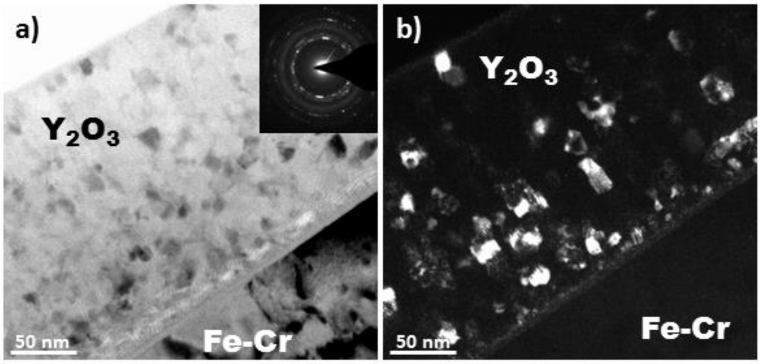

Figure 5-2: TEM bright field/dark field (BF/DF) micrographs of the yttrium oxide as deposited sample. (a) BF (b) DF. The yttrium oxide coating grows with nanocrystallinity (~20 nm). The spotty diffraction pattern (DP) in the inset of (a) confirms the presence of a crystalline thin films with small grain size.

In order to determine structural transformation in the coating after thermal exposure and irradiation and evaluate the eventual formation of reaction phases between the substrate and the thin film, XRD spectra were acquired and the results obtained are shown in **Figure 5-3**.

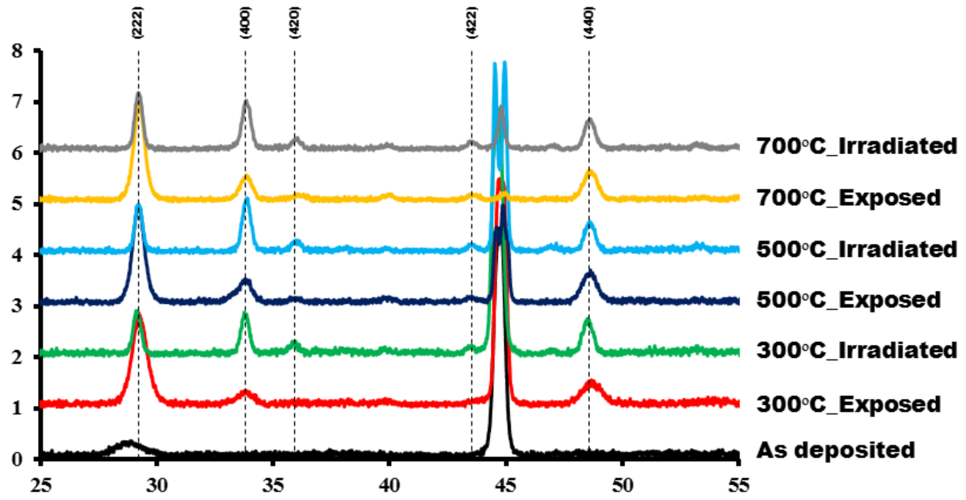

Figure 5-3: XRD spectra of the yttrium oxide coated samples, as deposited, thermally exposed and irradiated. All the indexed peaks correspond to cubic-Y_2O_3 according to PDF 00-041-1105. The peak positioned at a 2θangle of 44.8º is due to the substrate.

As can be seen, the thin films crystallize in the form of cubic Y_2O_3 (PDF 00-041-1105) with a preferred orientation along the (222) plane, as already seen by others for similar deposition conditions of Y_2O_3 [178]. One possible cause is that yttrium oxide with its bixbyite-type structure, similar to CaF_2, has ordered oxygen vacancies in which the (111) plane has the lowest surface energy, leading to a preferred growth in the [111] direction [179]. After thermal exposure at high temperatures, the (222) reflection slightly shifts toward higher 2 theta angles and increases its relative intensity. The shift toward higher 2 theta angles indicates a reduction of the lattice parameter. Other reflections, caused by the (400), (422) and (440) planes, appear after thermal exposure. The structure of the thin films remains cubic-Y_2O_3. The sharpening of the peaks is an indication of grain growth in the thin film, while their relative increase in intensity indicates an increase in crystallinity. Upon irradiation, the series of the (420) reflections appear in the spectrum.

In order to characterize the structure of the system and to study any eventual intermixing between the substrate and the thin film at a nanometer scale, STEM-EDS analysis was performed on the samples. **Figure 5-4** shows the results obtained for the samples thermally exposed at 300ºC, 500ºC and 700ºC.

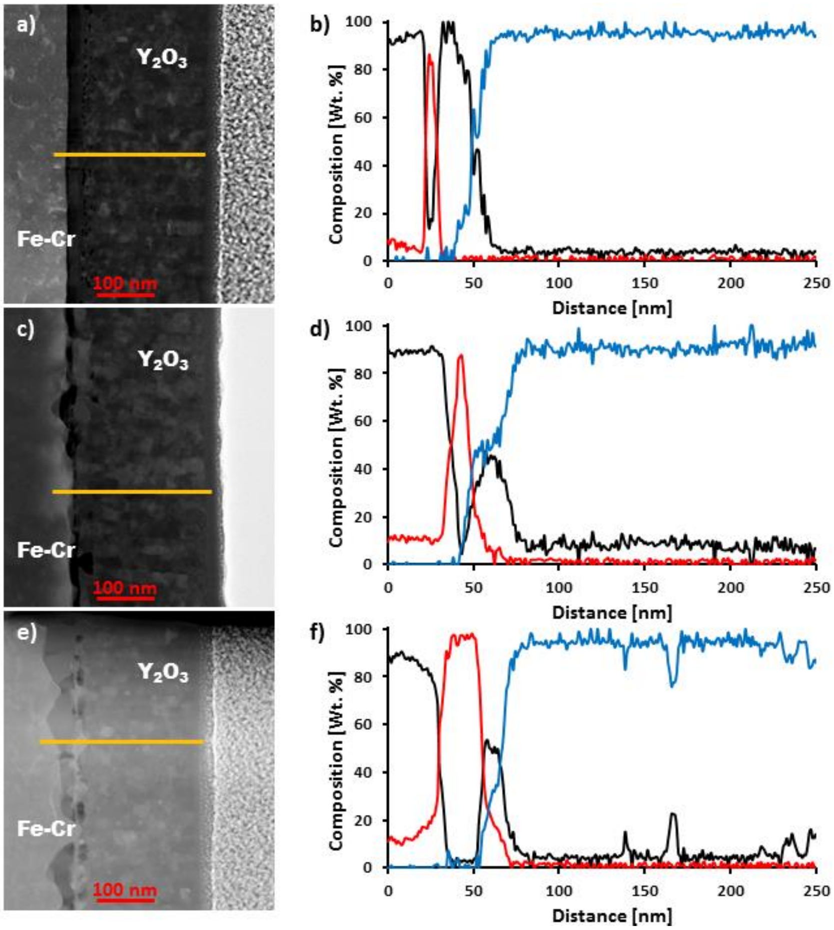

Figure 5-4: STEM-EDS elemental concentrations profiles across the Fe-12%Cr substrate – Y_2O_3 thin film interface in the thermally exposed at (a and b) 300˚C, (b and (c) 500˚C and (e and f) 700˚C. Compositional line scans were acquired along the orange line indicated in the ADF images.

The STEM images show that the interface between the substrate and the thin film is still visible and looks intact after thermal exposure however the EDS lines scans acquired across the interface indicate two notable findings. The first is the formation of a chromium enriched region at the substrate thin film interface - this region appears even after the thermal exposure at 300ºC, as indicated by the spike in the chromium concentration just below the substrate thin film interface. After exposures at 500ºC the spatial extent of this chromium enriched region grows in extent and in fact thin layer with a darker contrast is visible at the metal oxide interface. Furthermore, at this temperature, Fe also diffuses into the coating. At 700ºC chromium forms an even larger layer at the interface. The diffusion of iron inside the coating causes formation of iron enriched precipitates, as indicated by spikes in the iron concentration visible in the EDS line scan.

Figure 5-5 shows a higher magnification HAADF-STEM micrograph of the metal/oxide interface in the case of the sample thermally exposed at 300ºC.

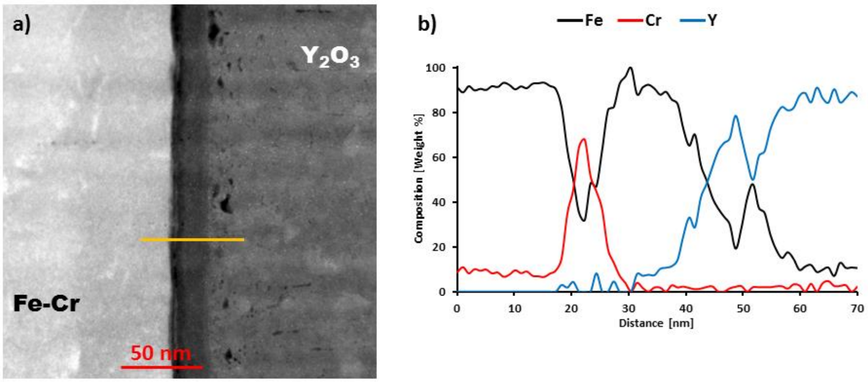

Figure 5-5: STEM-HAADF micrographs and experimental elemental profiles across the substrate-thin film interface in the thermally exposed samples at 300ºC. Compositional line scans were acquired along the orange line indicated in the HAADF image.

The pronounced Z-contrast of the image allows the identification of two different regions, characterized by a different average Z-number of the iron-based substrate and the Y_2O_3 coating. The inner region, darker in contrast, is the region enriched in chromium, while the lighter one is more enriched in iron. To better understand the diffusion of chromium and iron in this system during the initial stages of exposure at high temperature, in-situ TEM annealing of as-deposited sample was performed. **Figure 5-6** shows STEM-HAADF images and the relative EDS line scans of the sample in the as-deposited condition, and after TEM in situ annealing at 400ºC and 500ºC for one hour. Heat treatment was performed at 400ºC and 500ºC in order hasten the diffusion of iron and chromium as compared to what would normally occur during an annealing performed at 300ºC.

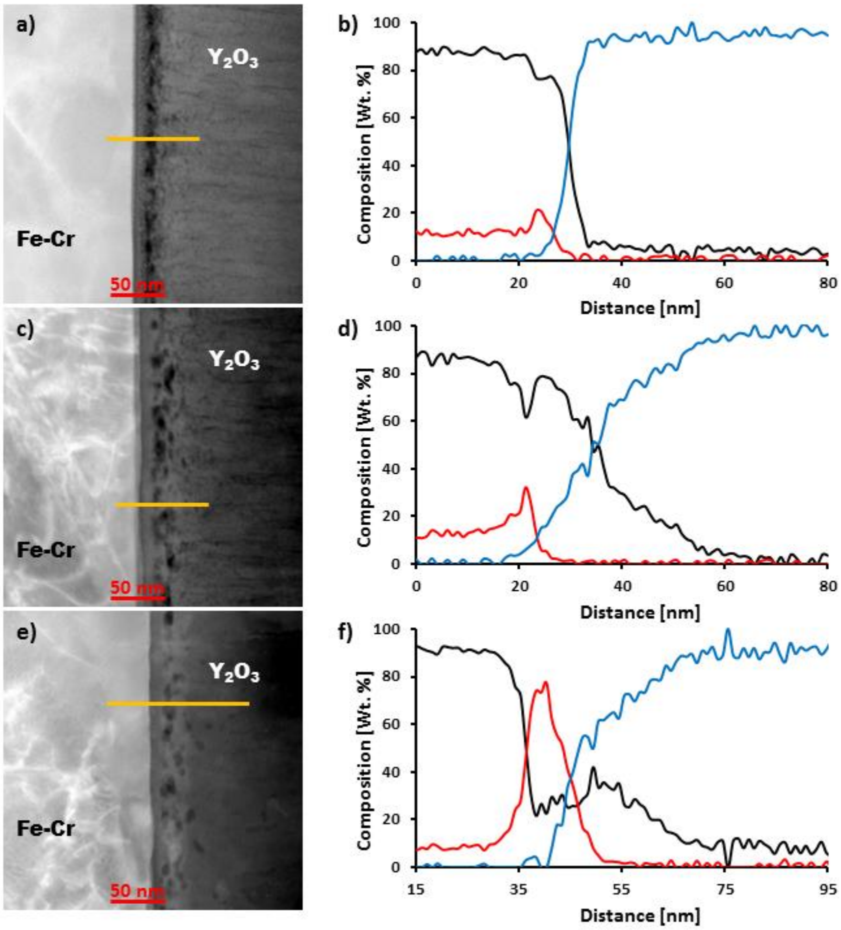

Figure 5-6: STEM-HAADF micrographs and experimental elemental profiles across the substrate-thin film interface in the Fe12%Cr-Y_2O_3 sample (a and b) as deposited sample (c and d) in situ annealed at 400ºC and (e and f) in situ annealed to 500ºC. Compositional line scans were acquired along the orange line indicated in the HAADF images.

As can be seen from **Figure 5-6** (b), there is an observable presence of a chromium peak at the metal/oxide interface and some porosity as indicated by dark spots in the film. During the first stages of annealing (at 400ºC), iron starts to diffuse into the film, while chromium diffuses to the metal/oxide interface. This trend is maintained at 500ºC. After annealing at this temperature chromium continues to accumulate at the metal/oxide interface and iron continues to diffuse inside the Y_2O_3 layer. These observations are consistent with the observation of **Figure 5-5**, namely at higher temperatures the diffusion of iron toward the film is more severe and at the same time chromium continues to diffuse toward the metal/oxide interface, increasing the chromium concentration at this region. At the same time, porosity in the coating is reduced, confirming the observation of increased crystallinity as revealed by the XRD analysis (**Figure 5-3**.

Recently, Choudhury et al. [23] performed DFT studies on Y_2O_3-Fe interfaces in the $[001]_{Fe}||[100]_{Y_2O_3}$ and $(010)_{Fe}||(011)_{Y_2O_3}$ orientation relationships. They pointed out that when chromium is present in the iron lattice, it will segregate to the metal/oxide interface depending on the local oxygen content, which in turn is affected by the misfit dislocation structure at the interface. In our samples, we observed already a slight enrichment of chromium at the metal/oxide interface in the as deposited sample. At high temperature chromium continues to segregate to the interface, to form first a thin continuous layer which, with increasing temperature, grows spatially in extent. There are some differences between our observation and the DFT results presented in [117]. While DFT simulations predict that chromium segregates at the interface starting at preferential positions (where misfit dislocations are located), we observed a more homogenous segregation of chromium at the interface. The differences between our observations and the DFT results might be rationalized based on the several differences between our systems and the system studied in these calculations. First, the DFT calculations were performed on a single orientation relationship, which corresponds to the case of two single crystals facing each other. In our experiments, on the other hand, the small size (~20 nm) of the Y_2O_3 crystallites in the as deposited condition causes the presence of multiple grains of the thin film to be in contact with grain of the substrate, which causes a variety of different orientation relationships to be present at the same time. Second, the abundance of grain boundaries in the thin film (and to some extent also in the Fe12%Cr substrate) provides preferential route for faster elemental diffusion, as compared to diffusion in the interior of grains. Third, the deposition process was performed at room temperature and at a very slow rate (0.1 Å/s), both factors contributing to form voids, which can favor diffusion processes inside the coating.

A drastically different behavior was observed in the irradiated samples. **Figure 5-7** shows the STEM-EDS results for the irradiated samples.

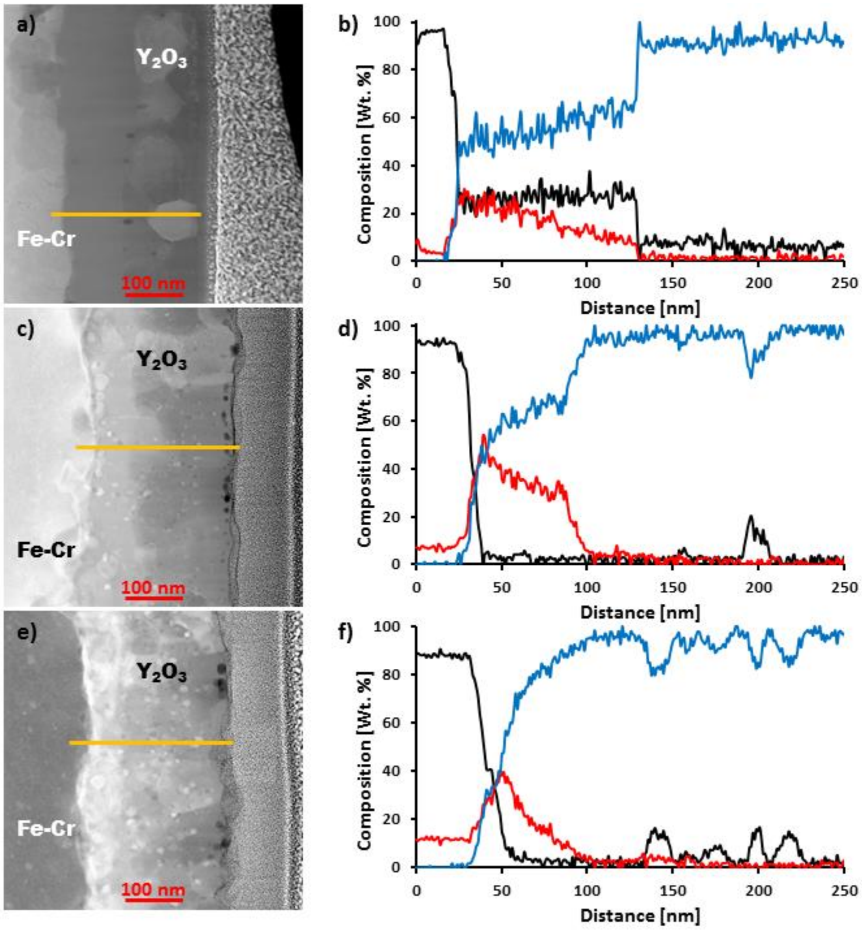

Figure 5-7: STEM-EDS elemental concentrations profiles across the Fe-12%Cr substrate – Y_2O_3 thin film interface in the thermally exposed at (a and b) 300˚C, (b and c) 500˚C and (e and f) 700˚C. Compositional line scans were acquired along the orange line indicated in the ADF images.

An interesting observation is the formation of an intermixed region between the substrate and the thin film. While at 300ºC this region is enriched in both Cr and Fe, and has a spatial extent of ~100nm, at 500ºC and 700ºC, its spatial extent gradually diminished and most notably, it appears that this region is enriched only of Cr and not of Fe. **Figure 5-8** shows a BF-STEM micrograph from the sample irradiated at 300ºC along with a Selected Area Diffraction Patterns (SADP) acquired from the intermixed region and EDS line scans of small precipitates.

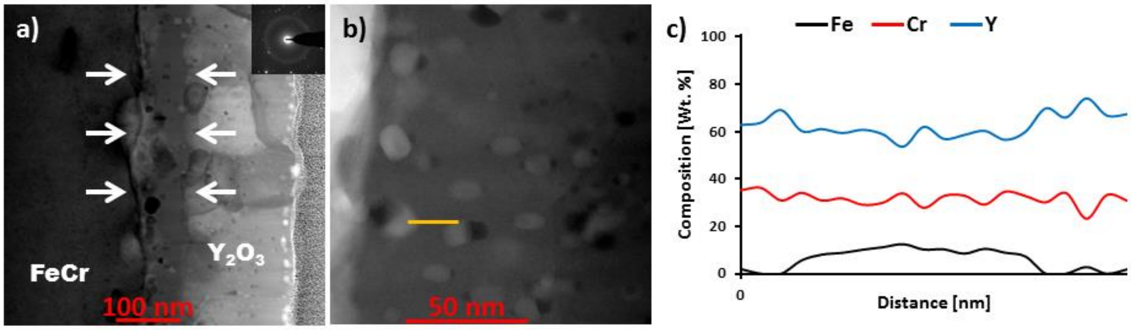

Figure 5-8: STEM micrographs and EDS analysis of the intermixed region between the substrate and the thin film in the sample irradiated at 300ºC (a) BF-STEM and DP (b) HAADF-STEM (c) EDS line scan. Compositional line scan was acquired along the orange line indicated in the ADF image.

As can be seen from **Figure 5-8**, EDS line scans performed on the fine precipitates in the intermixed regions show that they are enriched in iron. The diffusion of iron is enhanced at high temperature, as can be seen in the thermally exposed samples, and the irradiation facilitates the formation of small precipitates. It is interesting to note that a similar behavior was observed when similar set of alloys was coated with thin films of TiO_2 [180], where exposure at high temperature caused the diffusion of chromium into sub-stoichiometric regions of the thin films and then irradiation (similar to observations in this work) caused the diffused element to form a fine precipitation inside the thin film. It is interesting to note that the SADP acquired from the intermixed region shows diffuse ring features, typical of amorphous structures. This is a clear indication of radiation induced amorphization of the intermixed region between the substrate and the thin films. This was observed also in the samples irradiated at 500ºC and 700ºC, although the spatial extent of the amorphized region decreases at with increasing irradiation temperature. Liu et al [181] have identified rules for amorphization induced by ion beam mixing in pure metal/metal but no such studies have been performed on metal/oxide systems. Xu. et al. [112] also observed amorphization of sub-stoichiometric TiO_{2-x} when FeCr-TiO_2 bilayers were irradiated with Ni ions at 500ºC. The reason for the observed amorphization was speculated to be the Cr diffusion into the film and occupying substitutional positions, thus suppressing the bond strength between oxygen and the metal ions (causing increased defect production during irradiation) and retardation of the recombination process. Although an analysis of the stoichiometry of the films was not performed XRD analysis showed only the presence of cubic-Y_2O_3 in the thin film. A similar process might be speculated in this case as well, where irradiation is seen to promote not only diffusion of chromium but also of iron inside the ceramic film. Our results however are very interesting as they show that amorphization is possible at the metal/oxide interface of this bi-layered system which in turn is expected to have a strong impact on the radiation resistance of oxide nanoparticles in ODS steels.

Finally, as was already observed in XRD spectra (**Figure 5-3**), irradiation causes also grain growth in the films. ADF-STEM images of the samples after irradiation are shown in **Figure 5-9**.

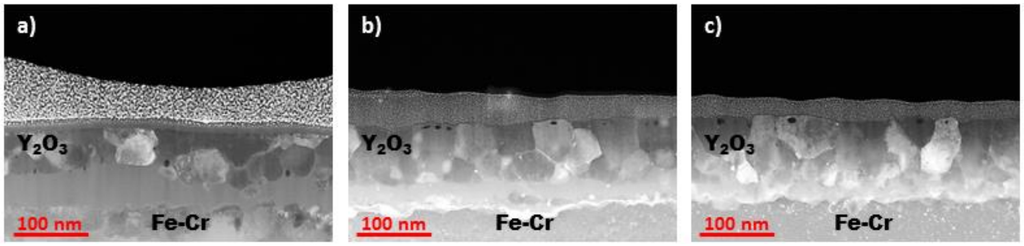

Figure 5-9: STEM-ADF images of the irradiated coatings (a) 300˚C (b) 500˚C (c) 700˚C. Irradiation clearly causes grain growth as compared to the as deposited and thermally exposed coating.

Qualitative grain size analysis (only few tens of grains are found in each sample) was performed by analyzing ADF- and BF-STEM micrographs. In the as deposited condition, the film is characterized by the presence of porosity and very small grains (~20 nm). After irradiation at 300ºC, the gran size becomes approximately 59 ±21.2 nm, at 500ºC 75±24 nm and at 700ºC 73±16 nm. Grain growth in ceramic thin films have been already observed after irradiation of thin films of ceria, [182–184], zirconia [184], yttria stabilized zirconia [185] and Al_2O_3 [186]. In other irradiated oxides the grain growth has been explained by an interaction of region with high local disorder, caused by the incident ions and grain boundaries. This interaction releases the excess free energy and leads to a self-limiting process of grain growth [182–185]. Finally, the outermost grains have an average size which is higher than the inner-most grains. This can be rationalized by taking into consideration the electronic-to-nuclear stopping power ratio (ENSP) of the irradiating particles. ENSP ratios are not uniform throughout the thickness of the samples, with higher values closer to the surface, as shown in **Figure 5-10**.

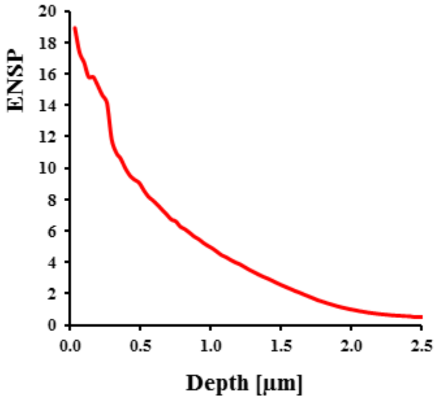

Figure 5-10: Electronic to nuclear stopping power for 5 MeV nickel irradiation. The ENSP values are higher in the outer regions of the films, which might explain bigger grain sizes in this region.

In other words, the fraction of the incident ion's energy lost through ionization rather than displacement cascades is higher in the near surface region. Because ionization enhances point defect diffusion in oxide ceramic insulators [187–190], the local *effective* temperature in such region must be higher than in the region close to the substrate thin film interface. This hypothesis could explain the observation that larger grains are usually observed in the outer regions of the films.

5.3 Conclusions

Film-substrate interface mixing effects in Y_2O_3 thin films deposited on Fe-12%Cr alloy substrates due to 5 MeV Ni^{2+} ion irradiations at 300˚C, 500˚C and 700˚C have been investigated at nanometer length scales by using STEM-EDS, TEM and XRD techniques. Radiation-induced effects were isolated from purely thermal effects by also examining regions of samples that were not irradiated but experienced the same thermal history. TEM in-situ annealing was also performed in order to study the evolution of the system during the first stages of temperature exposure. High temperature exposure causes diffusion of chromium to the metal/oxide interface, and diffusion of iron into the film. Irradiation has been shown to have multiple effects in the interfacial evolution of the system. First, it promoted the formation of an amorphous layer at the metal/oxide interface. The spatial extent of this amorphous layer decreased as the irradiation temperature was increased. Second, irradiation facilitated the formation of small Fe-rich nanoprecipitates in the film. Third, it resulted in grain growth in the Y_2O_3 film. Both chromium diffusion to the metal/oxide interface and amorphization at the interface after irradiation can have potential impact on in-service performance of ODS steels particularly in regards to mechanical properties, corrosion resistance, and radiation sink effect.

CHAPTER 6

Helium Implantations into Epitaxial non-Epitaxial Y_2O_3-Fe Interfaces

In this facet of the thesis, epitaxial and non-epitaxial Y_2O_3/Fe interfaces were grown as thin films in order to study the nucleation of helium bubbles at the metal/oxide interface. The long term goal was to emulate helium bubble nucleation and growth at metal/oxide interfaces in ODS steels. As the metal/oxide interface can constitute a preferential nucleation site for He bubbles, the questions addressed include :

1. Are there preferential orientation relationships (ORs) in the metal/oxide systems that favor He bubbles nucleation?
2. Do the bubbles grow inward toward the oxide or outward toward the matrix?

These are fundamental questions to answer as the existence of preferential orientation relationships (ORs) to nucleate helium bubbles could drive to the synthesis of materials with a large fraction of these ORs, in order to maximize the beneficial role of the small oxide particles in sequestrating He. Also, knowledge of the exact location of the nucleation of helium bubbles at the interface is useful. Bubbles nucleating at the metal/oxide interface and growing toward the matrix could potentially grow bigger in size as opposed to bubbles growing inward toward the oxide particle, as their size could be expected to be limited by the oxide particle size.

The experiments described in this chapter were indeed designed to answer the above questions. Epitaxial thin films of Y_2O_3 were deposited by Pulsed Laser Deposition (PLD) on single crystals of YSZ, purchased from the company MTI and oriented along the <100>, <110> and <111> directions. On top of the Y_2O_3 layer, thin Fe films were grown by Molecular Beam Epitaxy (MBE). Helium implantations were then performed at room temperature of thin TEM samples with a helium microscope at the University of California Berkeley.

Several bubbles nucleating in both the films and at the metal/oxide interface were imaged. Bubbles growing on interfaces with different ORs were all similar in size. Moreover, bubbles nucleating at the metal/oxide interface were seen to nucleate at random locations, and not in correspondence of misfit dislocations, which DFT and MD simulations predict to be as preferential nucleation sites. Nonetheless this study showed some very interesting results. First, a statistical analysis on the bubble size clearly showed that bubbles nucleating at the interface were significantly larger in size than bubbles growing within the individual layers. This observation confirms experimental results for bubbles seen to nucleate on metal/oxide interfaces in ODS steel and NFAs. All the bubbles imaged at the interface are located on the oxide side and only "wet" a small area of the interface. Conversely, bubbles nucleating at gran boundaries in the iron layer were seen to symmetrically overlap across the boundaries, revealing the different character of the metal/oxide interface.

The differences between the observations made in this work and some results predicted by theories are likely to be due to the temperature at which helium implantations were performed. It is expected that implantations performed at high temperature would have yielded results more close to those predicted by simulations. Nonetheless, these results are significant and we expect they will help develop first principle models of metal/oxide interfaces, which can eventually be translated to predicting helium bubble distribution in ODS and NFA steels.

6.1 Experimental Details

Interfaces with various crystallographic orientations between Y_2O_3 and Fe were synthesized using thin film deposition technologies at EMSL at Pacific Northwest National Laboratory. As a first step, epitaxial thin films of Y_2O_3 were deposited on yttria-stabilized zirconia (YSZ, zirconia containing 8% yttria) single crystal substrates with <100>, <110>, and <111> orientations, that were purchased from the company MTI. Depositions were performed by pulsed laser deposition from a pure Y_2O_3 target, using a KrF laser operating at 248 nm, 4 Hz, and a fluence of ~2.4 x 10^4 J/m^2 on the target. The substrate was maintained in a background oxygen pressure of 1.33 Pa and at a temperature of 750ºC. The films were deposited to a thickness of ~300 nm. After the Y_2O_3 deposition the samples were loaded into an ultra-high vacuum (UHV) MBE system. Any potential carbon contamination was cleaned by exposure to activated oxygen generated in an electron cyclotron resonance microwave plasma source at room temperature for 30 minutes. Samples were then heated to ~550°C for deposition of Fe film (to a nominal thickness of 40 nm) from an effusion cell (flux rate 0.012 nm/s). Reflection high energy electron diffraction (RHEED) patterns were monitored to observe the crystalline order of the cleaned Y_2O_3 surface and the subsequent Fe deposition. HR-XRD patterns were also collected to determine any epitaxial relationship between the Y_2O_3 and the Fe films. After deposition and initial characterization, the samples were coated with a thin film (~10 nm) of gold by sputter deposition. This served the purpose of not only protecting the very thin Fe film from oxidation, but also to improve the electrical conductivity of the samples, in order to facilitate TEM sample preparation by the FIB technique.

As the main focus of this work is based on TEM analysis, results from the RHEED spectra and pole figure analysis are not shown. Their interpretation would not yield any information not encompassed in the TEM analysis. In fact, due to the small size of the individual Fe grains growing on the Y_2O_3 thin film, actual ORs between the Fe and theY_2O_3 layers had to be determined by TEM analysis, by acquiring High Resolution images and then using their Fast Fourier Transform (FFT) to determine the relative orientation of planes within the two layers. In the helium implanted samples, bubbles were imaged with a STEM-HAADF detector using an aberration corrected Titan (S)TEM from FEI with a probe size of less than 1 Å. Due to a smaller Z-number for He, as compared to Y_2O_3 and Fe, He bubbles manifested as dark spots in the micrographs. This imaging technique for voids and bubbles was preferred over the conventional Fresnel contrast method as the identification of small bubbles close to interphase boundaries in C-TEM is complicated by spherical aberration and defocus effects [191].

6.1.1 As-deposited samples

Figure 6-1 shows high resolution images of the Y_2O_3 film grown on the three YSZ substrates. As can be seen, Y_2O_3 forms an epitaxial film on the YSZ substrate. However, RHEED spectra, pole figure analysis and HR-STEM revealed that the Y_2O_3 thin film grew with a very rough morphology on top of the YSZ (111) single crystal. As a consequence, the Fe deposited on top of the Y_2O_3 layer for this sample was completely nano crystalline and no ORs between the two film materials were observed. As a result, this sample was excluded from further analysis.

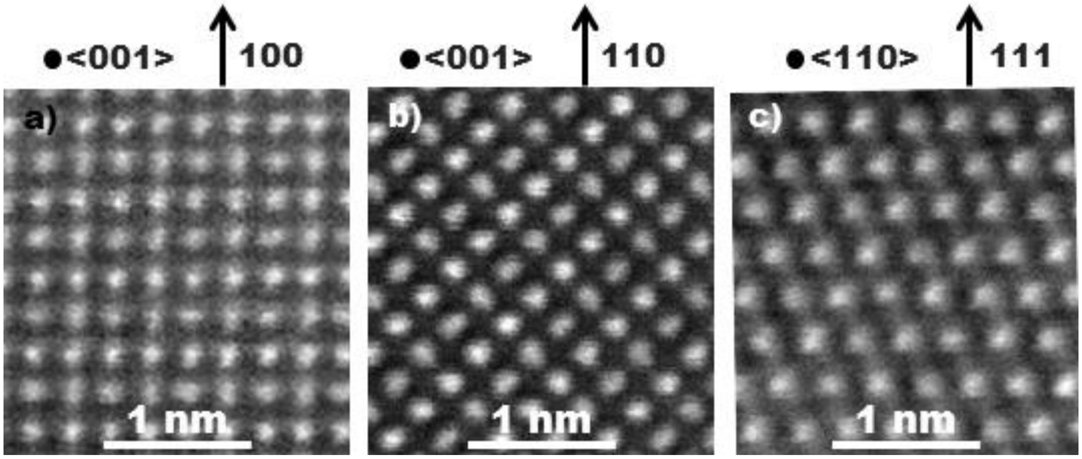

Figure 6-1: High resolution images of the Y_2O_3 thin films grown on YSZ oriented along (a) (100) (b) (110) and (c) (111) directions.

Figure 6-2 shows low magnification BF-STEM micrographs of the Y_2O_3/Fe grown on the (100) YSZ and (110) YSZ substrates. On the YSZ (100) substrates, the Y_2O_3 film grows as a mostly flat and epitaxial layer, while on top of the Y_2O_3 film, Fe grows as a continuous film. However, only very small patches of the Fe layer (such as the small dark grain of **Figure 6-2** (a)) had a defined orientation relationship to the substrate. On the other hand, in the Y_2O_3/Fe interfaces grown on the YSZ (110) substrate, Y_2O_3 grows again as a flat epitaxial thin film, while Fe grows in the form of ~150 nm wide islands. Many of the Fe islands exhibit specific ORs with the underlying Y_2O_3 layer.

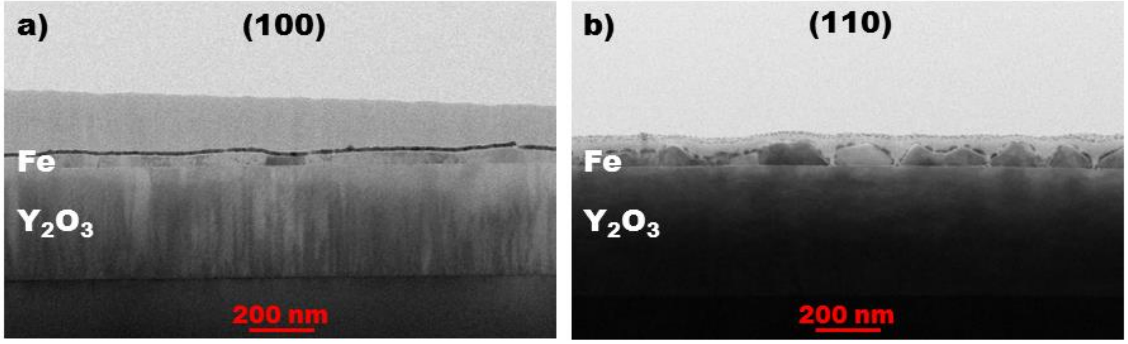

Figure 6-2: Low magnification BF-STEM images of the Y_2O_3/Fe bilayer grown on the (a) YSZ (100) and (b) YSZ (110) substrates. On the YSZ(100)/Y_2O_3 Fe grows with a continuous, relatively flat film and very small patches which had a defined ORs with the Y_2O_3 film. On the YSZ(110)/Y_2O_3, Fe grows mostly with ~150 nm wide islands, many of which had an orientation relationship with the Y_2O_3 film.

Therefore there is a general difference in the Fe film morphology, with the Fe grown on the YSZ/Y_2O_3(100) sample which exhibits a Frank–van der Merwe (FM) growth mode (2D morphology, layer-by-layer growth) and the Fe film grown on the YSZ/Y_2O_3 (110) sample which exhibits the Volmer–Weber (VW) growth mode (3D morphology with island growth). Several factors play a role in the determination of the growth mode, but typically thermodynamic considerations can aid in understanding some basic principles [192]. The F-M mode will be dominant when the surface energy γ for various interfaces obeys the following relationship:

$$\gamma_{s,f} \geq \gamma_{s,v} + \gamma_{f,v} \qquad \text{Equation 6-1}$$

where the subscript *s* stands for substrate, *f* for film and *v* for vacuum and γ represents surface energy. There is also a competition between the film–substrate atom interactions and the film atom-atom interactions. Typically these quantities are expressed by the isosteric heat of absorption V_0 and the lateral adatom attraction e_1. The expected growth mode will depend also on the lattice misfit defined as in Equation 6-2:

$$\Delta = \frac{n d_{film} - d_{substrate}}{d_{substrate}} \times 100$$ Equation 6-2

where Δ is the lattice mismatch in %, d_{film} is the interatomic distance of the thin film (Fe in this case) and $d_{substrate}$ is the interatomic distance in the substrate (Y_2O_3 in this case) and n is an integer number to keep the lattice mismatch <50%. Small lattice misfit and high V_0/e_1 ratios will yield to the FM growth [192]. Because both V_0 and e_1 are expected to be similar for the two different systems, the different growth modes can be attributed to either a different lattice mismatches or a different Y_2O_3 surface energy. Y_2O_3 has a cubic bixbyite structure, based on a slightly distorted FCC array of yttrium cations with 3/4 of the tetrahedral sites occupied by oxygen ions [193]. Based on this observation, it is tempting to estimate the surface energies in this case using simple models such as the "bond breaking model", in which the surface energies are estimated from the number of bonds that are needed to be broken when a certain surface is created. This model allows at least a first order comparison of the surface energies of low index surfaces for metals. In the case of oxides however an additional complication arises from the presence of oxygen. **Figure 6-3** shows a schematic cross sectional illustration of two Y_2O_3 surfaces. As can be seen, the formation of $\{100\}_{Y_2O_3}$ surfaces through the separation of adjacent Y layers would cause the formation of two different surfaces, one which terminates in oxygen atoms, the other which terminates in Y atoms. Consequently the two surfaces will have very different energies. Conversely the formation of $\{110\}_{Y_2O_3}$surfaces would lead to the formation of two equivalent surfaces. Thus, while breaking bond model considerations (for FCC structures) predict the $\{100\}_{Y_2O_3}$ surface to be more stable than the $\{110\}_{Y_2O_3}$surface, the determination of the surface energy for the entire structure in this case is not trivial and cannot be performed without the use of DFT calculations.

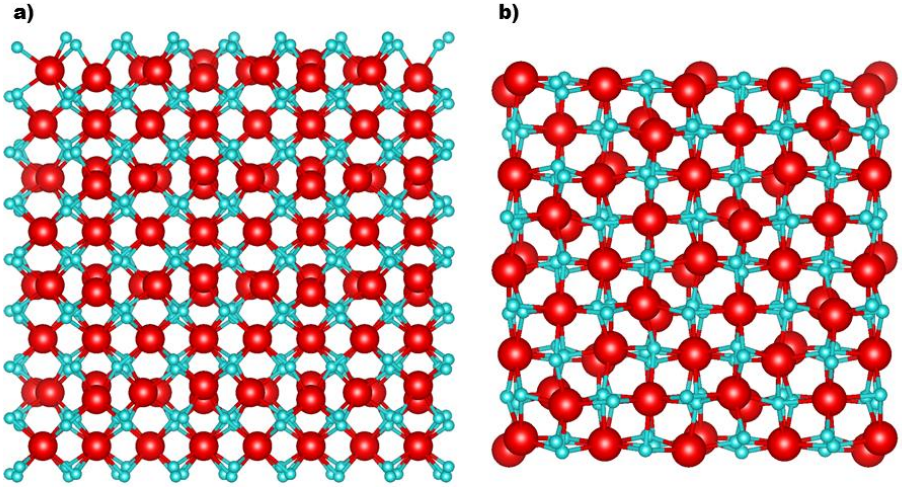

Figure 6-3: Schematic cross section view of (a) $\{100\}_{Y_2O_3}$ and (b) $\{110\}_{Y_2O_3}$ surfaces. Red spheres are Y atoms and light blue spheres are O atoms.

Aberration corrected STEM images for the Y_2O_3/Fe interfaces grown on the YSZ (100) and YSZ (110) substrates are shown in **Figure 6-4**.

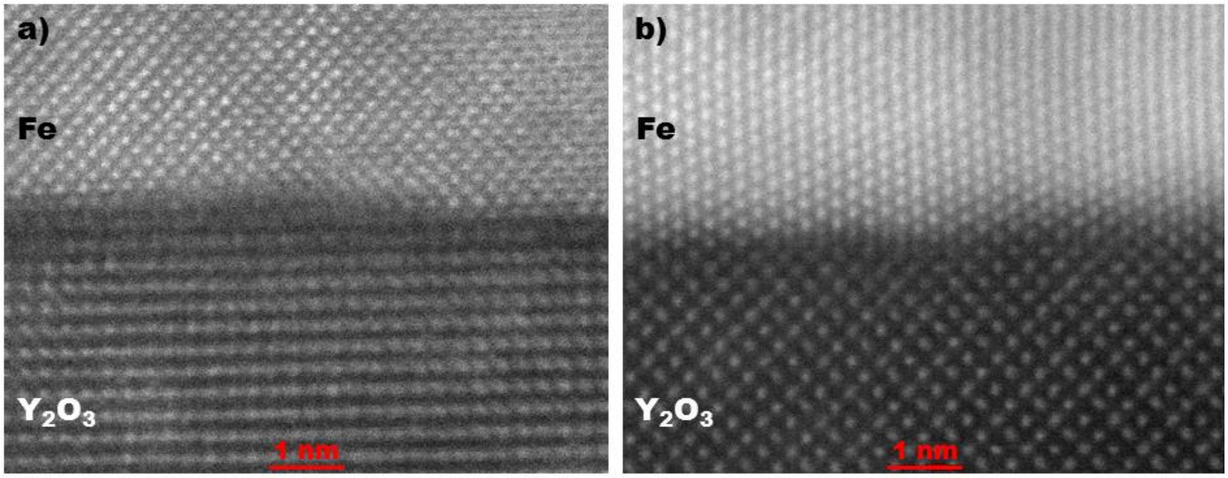

Figure 6-4: Aberration corrected STEM images of the as-deposited films (a) YSZ(100)/Y_2O_3/Fe and (b) YSZ(110)/Y_2O_3/Fe interfaces.

As can be seen both samples have regions of epitaxy between the Y_2O_3 and the Fe layers. HR images from epitaxial regions of the interface were acquired, and the ORs were determined analyzing the FFTs of the acquired images. As an example of the procedure adopted for determining ORs in the samples, the $\{001\}_{Y_2O_3}||\{111\}_{Fe}$ & $(110)_{Y_2O_3}||(\bar{1}2\bar{1})_{Fe}$ OR, which is also the most common for the YSZ(110)/Y_2O_3/Fe sample, is shown in **Figure 6-5**.

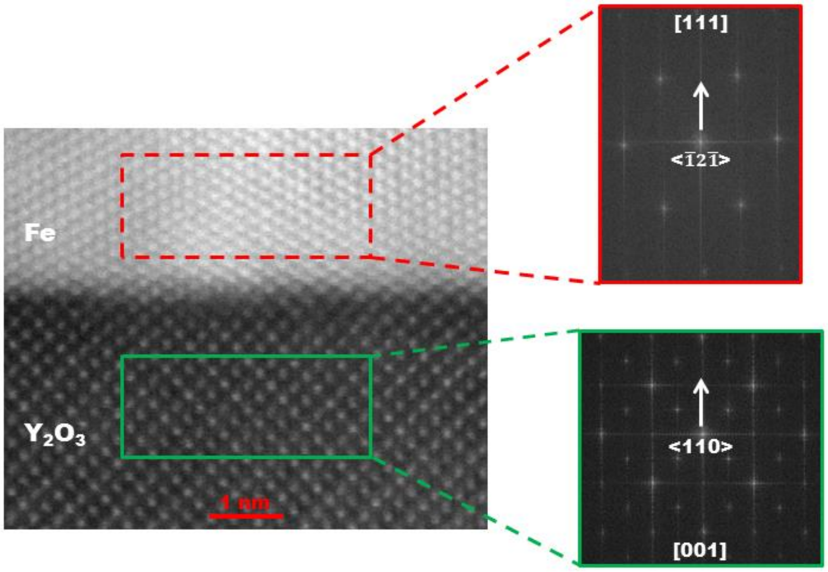

Figure 6-5: OR determination for one Fe grain in the YSZ(110)/Y_2O_3/Fe sample. FFT of the Y_2O_3 layer corresponds to the $\{001\}_{Y_2O_3}$ zone axis and for Fe it corresponds to the $\{111\}_{Fe}$ zone axis. $(110)_{Y_2O_3}$and $(\bar{1}2\bar{1})_{Fe}$ directions are indicated by arrows in the FFT image.

Once the HR image is acquired, its FFT, which contains information of the crystal structure, can be indexed as a diffraction pattern. Therefore, by determining the relative zone axis and two parallel planes, the OR can be readily determined. By employing this approach, ORs for various samples were analyzed and are summarized in **Table 4**. TEM analysis showed that an acceptable degree of epitaxy was reached only for samples grown on the <110> oriented YSZ substrates, meaning that several Fe islands were found to have a well-defined OR with the underlying Y_2O_3 layer, with the OR3 (in Table 4) found to be the most common case. For the <100> a lower degree of epitaxy was achieved, meaning that in every TEM sample, only very few small Fe grains had a defined OR with the underlying Y_2O_3 layer.

Table 4. Different ORs observed between Fe and Y_2O_3 for the films grown on the YSZ(100) and YSZ(110) samples.

	YSZ(100)/Y_2O_3/Fe
OR1	$[001]_{Y_2O_3}\|\|[111]_{Fe}$ & $(100)_{Y_2O_3}\|\|(10\bar{1})_{Fe}$
OR2	$[001]_{Y_2O_3}\|\|[001]_{Fe}$ & $(100)_{Y_2O_3}\|\|(0\bar{1}\bar{1})_{Fe}$

	YSZ(110)/Y_2O_3/Fe
OR3	$[001]_{Y_2O_3}\|\|[111]_{Fe}$ & $(110)_{Y_2O_3}\|\|(\bar{1}2\bar{1})_{Fe}$
OR4	$[001]_{Y_2O_3}\|\|[111]_{Fe}$ & $(110)_{Y_2O_3}\|\|(10\bar{1})_{Fe}$

As discussed in **Section 2.5.2**, the semi-coherent interfaces have a structural non uniformity that leads to a non-uniformity in interfacial energies. Interfacial energy will be higher near misfit dislocation intersections and lowest near the regions of coherency [98,194]. Helium bubbles forming at these interfaces will preferentially wet regions of high energy and might not wet at all regions with low energy [98,195]. In order to study misfit dislocation structure of the samples analyzed, the FFT approach was used. **Figure 6-6** shows misfit dislocations at the interface of the YSZ(110)/Y_2O_3/Fe sample in the OR3 configuration. **Figure 6-6** (b) shows an image obtained as FFT reconstructed with only the spots circled in **Figure 6-6** (a), which corresponds to a set of planes perpendicular to the interface.

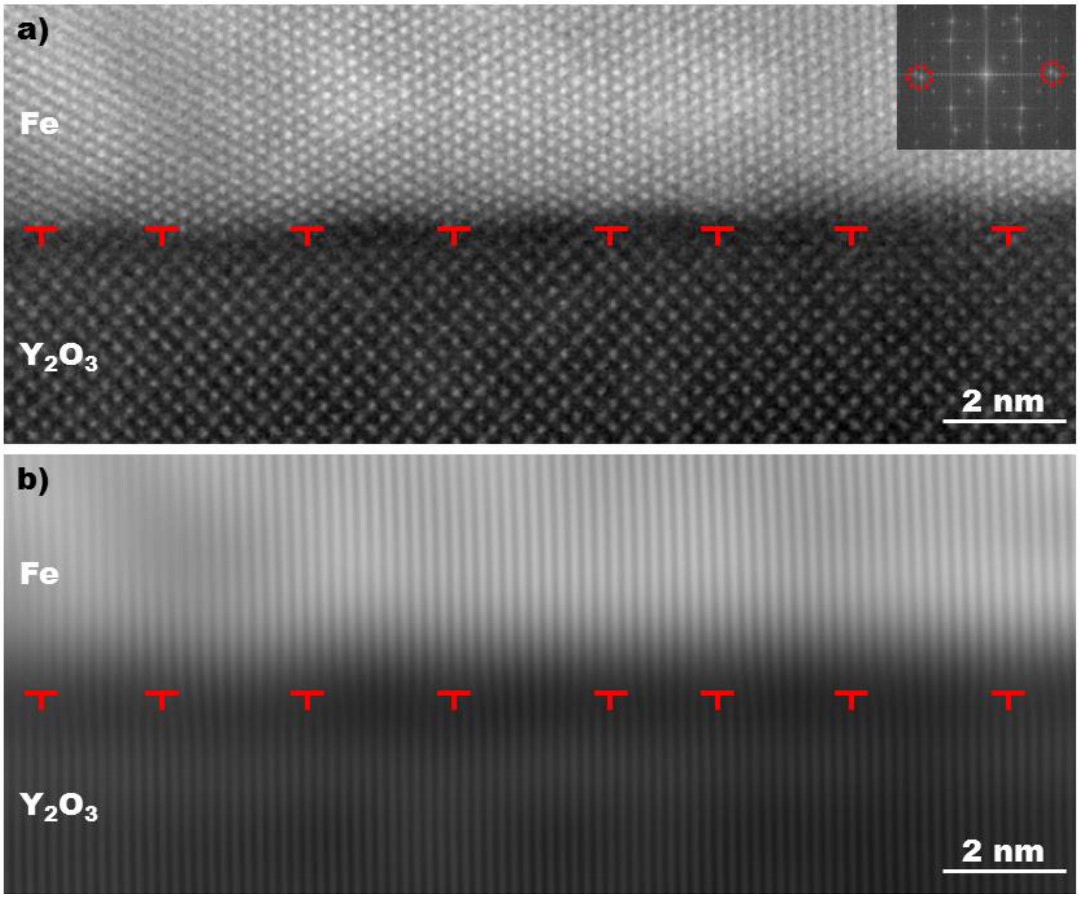

Figure 6-6: Misfit dislocations at the interface of the YSZ(110)/Y_2O_3/Fe sample in the OR3 configuration.

The procedure adopted in **Figure 6-6** serves only as a visual aid to identify MDs. The same information can be obtained from the original image by connecting with straight lines the Y_2O_3 planes to Fe planes across the interface to identify extra planes in the Y_2O_3 layer. As can be seen MDs are not regularly spaced and a MD is typically found every 7 to 13 planes of Y_2O_3. As the YSZ (110)/Y_2O_3/Fe sample was the one which exhibited the stronger epitaxy, with OR3 being the dominant orientation, a 3-D reconstruction of the interface was performed with VESTA software, as shown in **Figure 6-7**. Oxygen was excluded in this analysis due to its low atomic number as compared to Y, which makes it barely visible with conventional aberration corrected STEM imaging.

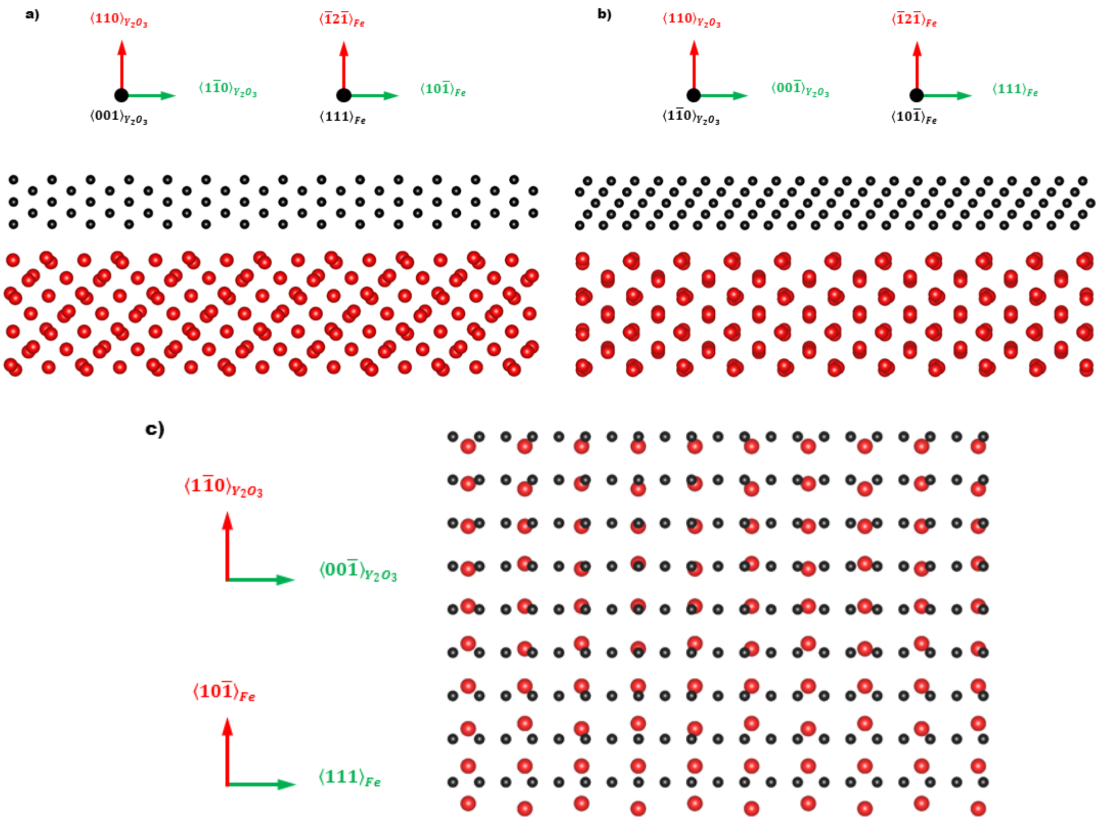

Figure 6-7: Views of the Y_2O_3/Fe interface in the OR3 configuration, (a) cross section as in **Figure 6-5**, (b) cross sectional view after 90° rotation around the $\langle 110\rangle_{Y_2O_3}$direction, and (c) top view. Red spheres are Y atoms and black spheres are Fe atoms.

As can be seen a reasonable lattice match is achieved when the $\langle 1\bar{1}0\rangle_{Y_2O_3}$direction is parallel to $\langle 10\bar{1}\rangle_{Fe}$. In fact, on the $(110)_{Y_2O_3}$ surface the Y-Y interatomic distance varies between 3.53 Å and 4.01 Å. On the $(\bar{1}2\bar{1})_{Fe}$ the Fe-Fe distance is 4.05 Å. By using **Equation 6-2** the lattice mismatch can be calculated to be between 1.34% and 15.4% when the $\langle 1\bar{1}0\rangle_{Y_2O_3}$direction is parallel to the $\langle 10\bar{1}\rangle_{Fe}$ direction and -6.4 % and -7.1%, respectively, when the $\langle 00\bar{1}\rangle_{Y_2O_3}$ direction is parallel to the $\langle 111\rangle_{Fe}$ direction (Y-Y interatomic distance varies between 5.30 Å and 5.35 Å and the Fe-Fe distance is 2.48 Å). Variation in Y-Y distances might also explain the change in spacing between misfit dislocations at the interface. **Figure 6-8** shows top view images of selected planes of Fe along with the Fe-Fe distances. Because both the $(100)_{Y_2O_3}$ and the $(110)_{Y_2O_3}$ surfaces have atoms in a distorted rectangular lattice, among the low index surfaces of Fe, the ones allowing to minimize the lattice misfit are indeed the ones of the $\{112\}_{Fe}$ family. Other possible matches could be obtained on the $(111)_{Y_2O_3}$ surface which, unfortunately, grew very irregular in our depositions.

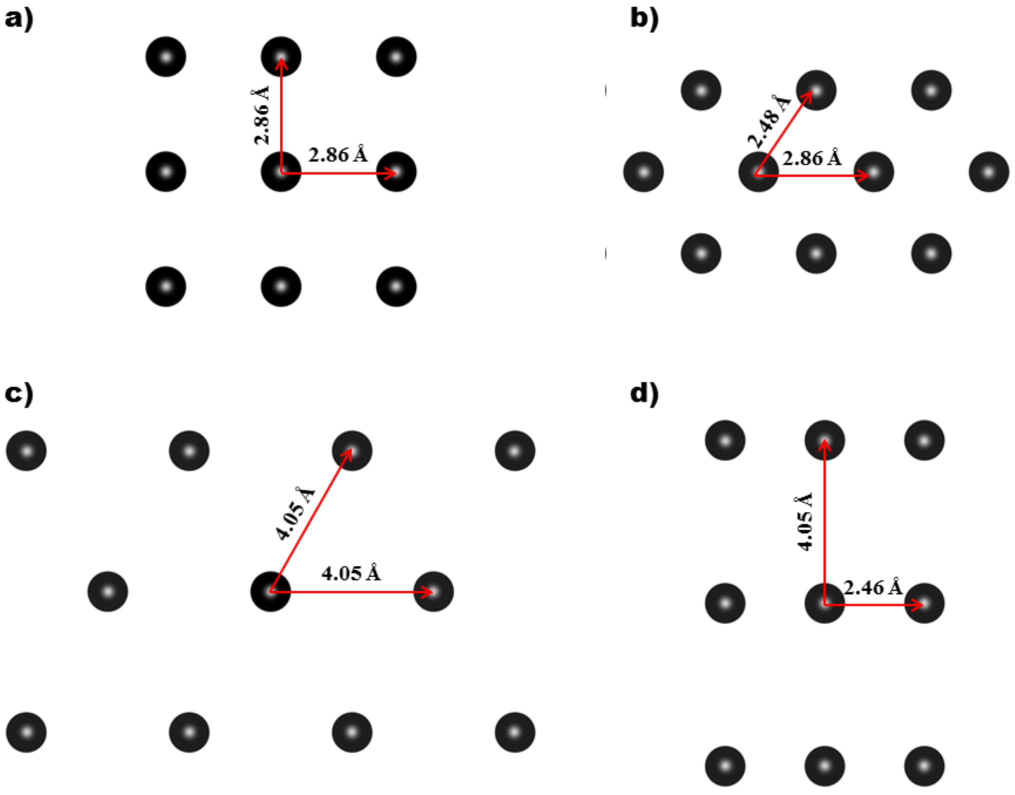

Figure 6-8: Top view of selected planes of iron and relative Fe-Fe distances (a) (100), (b) (110), (c) (111), and (d) (211) planes.

The lower degree of epitaxy for the $(100)_{Y_2O_3}$ surface may possibly be due to the high energy of this surface, in the case of oxygen rich terminations, as shown in **Figure 6-3** (b). It may be possible to achieve further improvements in epitaxy by controlling deposition parameters such as for example using higher deposition temperature; nevertheless interfaces synthesized in this study provided a valuable template for studying the nucleation of helium bubbles.

6.2 Helium implantations

Helium implantations were performed with a Zeiss Helium microscope at the University of California, Berkeley. Several attempts were made to optimize parameters for helium implantations. Initially, two batches of samples with thicknesses of ~200 nm and ~130 nm were investigated. In order to maximize the amount of He implanted inside the TEM foils, the first set of samples was irradiated with 25 keV He ions, while the second set was irradiated with 15 KeV He ions. **Figure 6-9** shows an SEM view of the irradiated samples, indicating the irradiation area. In the image, the Y_2O_3/Fe interface is at the top of the sample, therefore the irradiation area largely encompasses the interface to be irradiated.

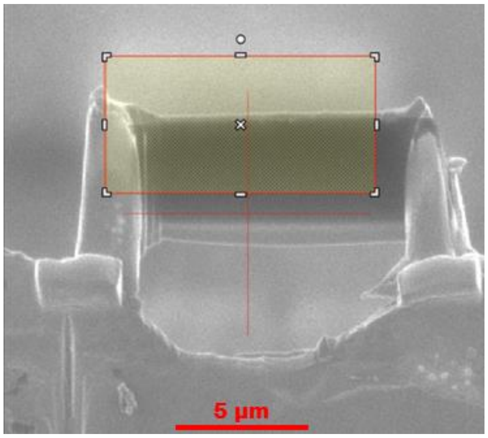

Figure 6-9: SEM micrograph of a 130 nm thick YSZ(100)/Y_2O_3/Fe sample showing the helium implanted area (red rectangle) .

In both the implantations the microstructure of the samples was severely damaged and TEM analysis became overwhelmingly challenging. A very large number of extremely small bubbles could be identified in both the Y_2O_3 and the Fe layers, along with numerous defects and blisters in the YSZ substrate. In some regions of the Y_2O_3/Fe interface, it appears that He accumulation causes swelling or possible de-bonding between the two layers, or a combination of the two effects. Moreover, the surface of the Y_2O_3 films appeared to have become rough after implantation and structural investigations were complicated by the fact that Kikuchi lines in the Y_2O_3 layers – fundamental to properly tilting and aligning the sample along the right direction to achieve optimal imaging conditions – could not be clearly identified. **Figure 6-10** shows a YSZ(100)/Y_2O_3/Fe sample, originally 130 nm thick, before and after 15 KeV He implantation up to a nominal dose of 10^{18} ions/cm^2.

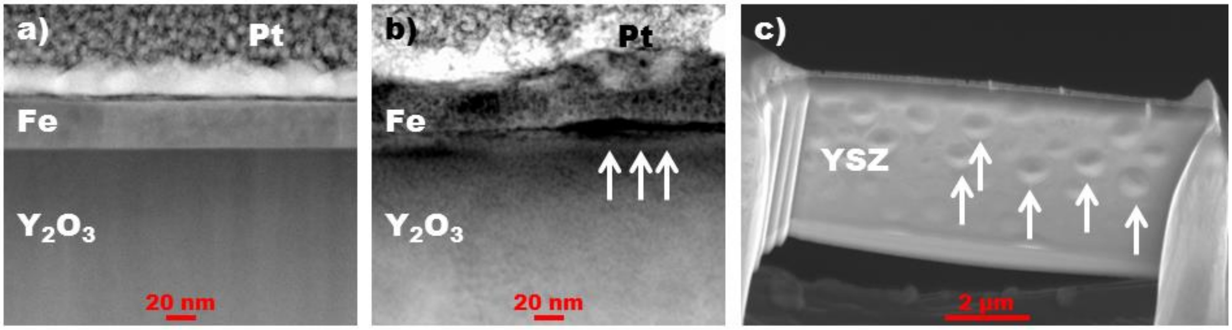

Figure 6-10: TEM and SEM images of a YSZ(100)/Y_2O_3/Fe sample, initially 130 nm thick, before and after He implantation with 15 KeV He ions (a) HAADF-STEM image before He implantation (b) HAADF-STEM image after implantation (c) SEM Inlens image after implantation. Arrows in (b) indicate regions of voids accumulation or de-bonding at the Y_2O_3/Fe interface and in (c) blisters in the YSZ layer.

Therefore, in order to determine the best parameters to employ for further implantations several samples of different thickness were implanted with He. It was observed that when samples were irradiated with He ions having a sufficient energy to completely penetrate the TEM foils, bubbles were more readily visible without incurring damage effects in samples. Therefore, thin samples (with a thickness lower ~70nm) were implanted with 25 KeV He ions. As revealed by SRIM generated data for ions range in solids, the projected range of 25 KeV He is 95 nm in Fe and 143 nm in Y_2O_3. The effect of decreasing the sample thickness is therefore equivalent to a reduction of the dose rate, and promotes formation of bubbles in the samples. The irradiation current was kept at ~18 pA, the lowest achievable on the instrument, as it was also observed that samples irradiated at higher currents (~90 pA) to the same dose did not show bubbles in their structure. Even though the two material films exhibit differences in the projected range of helium ions, SRIM simulations [19] indicated that the average He concentration in both the layers was comparable (**Figure 6-11**). Parameters for the simulations were displacement energies of 40 eV for Fe, 25 for Y and 28 for O and a sample thickness of 65 nm for both Fe and Y_2O_3.

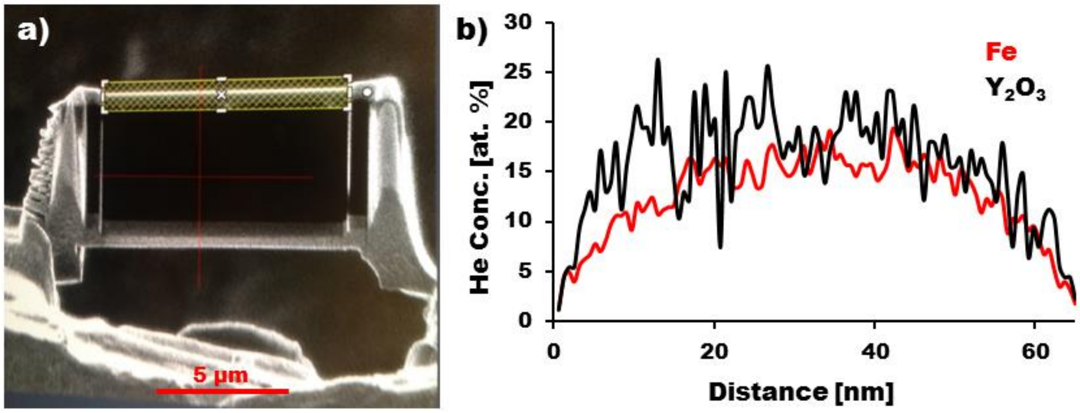

Figure 6-11: He implantation of a YSZ(100)/Y_2O_3/Fe sample initially 65 nm thick (a) SEM image with implantation area indicated in yellow and (b) He concentration profile as determined by SRIM simulations.

Several bubbles were identified in both the Fe and Y_2O_3 layers, and at interfaces with different ORs. **Figure 6-12** shows high resolution images of bubbles (manifested as contrasting black spots) that form in the Fe and the Y_2O_3 films as well as at the grain boundaries of the Fe film. A statistical analysis the bubble size yielded a value of 1.55 ± 0.28 nm in the Fe film and 1.45 ± 0.31 nm in the Y_2O_3. It must be noted that bubble identification was more challenging in the oxide layer due to a generally weaker contrast exhibited by the bubbles, due most likely to the lower average Z-number of the oxide layer, as compared to iron. Other authors, investigating He implantation from the top surface on Fe/$Y_2Ti_2O_7$ bilayers, could not identify helium bubbles in the oxide layer, but were able to identify them in the metal layers. They attributed this to either (i) a diffusion of He out of the $Y_2Ti_2O_7$ layer,(ii) its dissolution throughout the structure, or (iii) inability to image the bubbles due to their fine size [191].

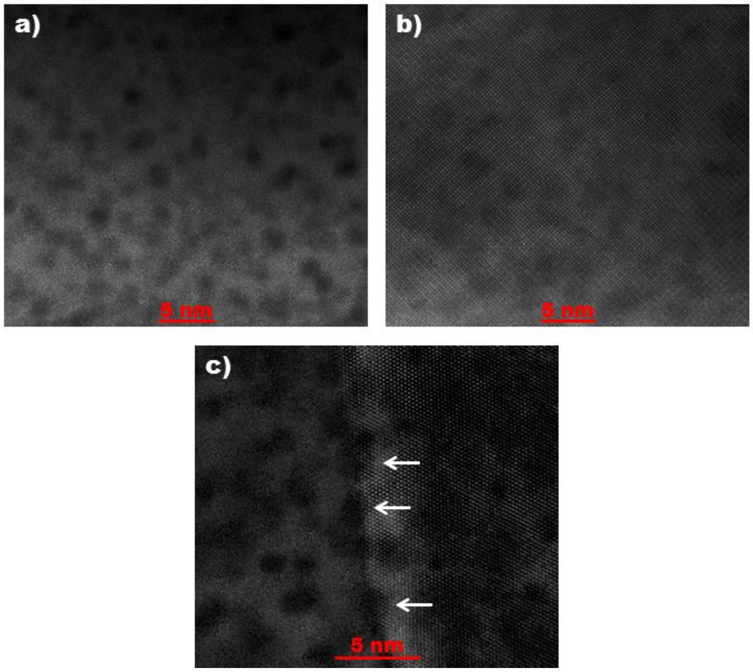

Figure 6-12: HAADF-STEM micrographs of a He implanted YSZ(110)/Y_2O_3/Fe sample initially 65 nm thick showing helium bubbles at (a) Fe grain (b) Y_2O_3 film, and (c) along a Fe grain boundary. Arrows in (c) indicates bubbles overlapping across the grain boundary.

Figure 6-13 displays a relatively large section of the Y_2O_3/Fe interface grown on an YSZ (100) sample and was obtained by combining 4 STEM-micrographs. BF images are also displayed because changes in the contrast in the Fe film can be correlated to changes in the relative orientation of the Fe grains. Therefore, because the orientation of the Y_2O_3 layer with respect to the electron beam is mostly uniform, changes in the orientation of the Fe grains corresponds to changes in the ORs between the Fe and the Y_2O_3 layers. The changes in contrast still visible in the Y_2O_3 film are likely to be due to local changes in thickness and with only slight variation of orientation with respect to the electron beam.

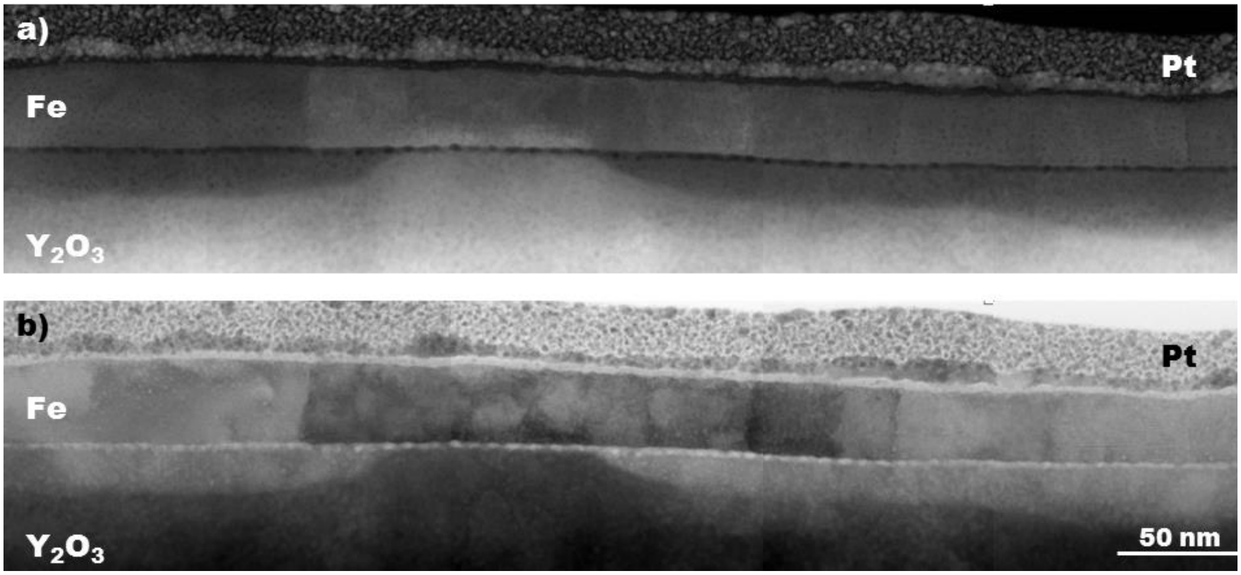

Figure 6-13: STEM micrographs of a He implanted YSZ(100)/Y_2O_3/Fe initially 65 nm thick (a) HAADF (b) BF. Variation in contrast in the BF images in the Fe film correspond to variation in the relative orientation while contrast variation in the Y_2O_3 layer is likely due to local thickness variations.

Careful analysis of **Figure 6-13** reveals, as already seen in **Figure 6-12** that small bubbles form in both the Fe and the Y_2O_3 layer and, most notably, larger He bubbles are clearly visible along the Y_2O_3 interface. **Figure 6-14** shows a relatively large section of a different irradiated TEM sample of a Y_2O_3/Fe interface grown on a YSZ (100) sample. This image was also obtained by combining several STEM-micrographs.

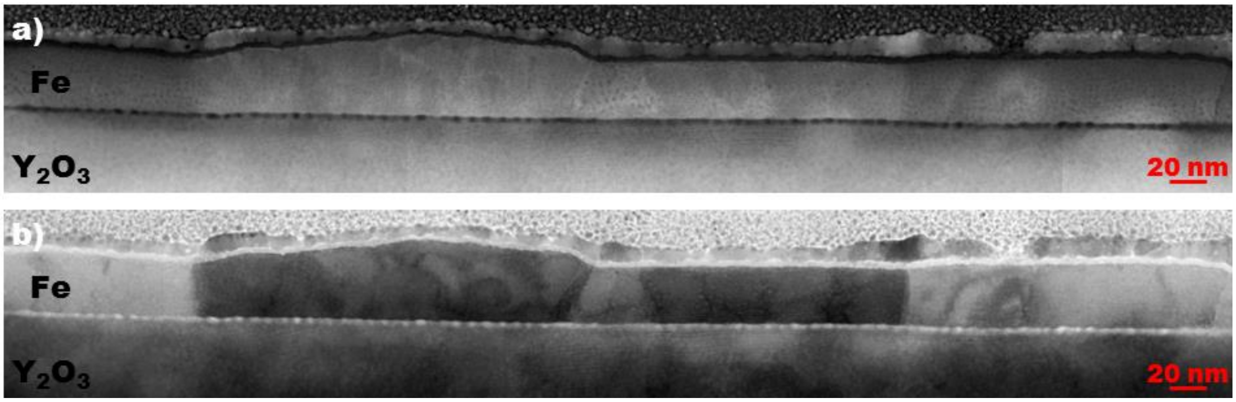

Figure 6-14: STEM micrographs of a He implanted YSZ(100)/Y_2O_3/Fe initially 75 nm thick (a) HAADF and (b) BF. Variation in contrast in the BF images in the Fe layer corresponds to variation in the relative orientation of the Fe grain.

Figure 6-14 and **Figure 6-13** indicate similar results, namely, across differently oriented Fe grains (and therefore with different ORs with respect to the Y_2O_3 layer) the bubble size distribution looks uniform. Several interface patches were analyzed in order to determine the average bubble size along different regions of the interface. It was observed that most of the bubbles nucleating at the interface have a spherical shape. A few bubbles were ellipsoidal, but this shape might derive from the juxtaposition of two or more smaller spherical bubbles. **Figure 6-15** shows an aberration corrected STEM image of He bubbles nucleated at a Y_2O_3/Fe interface with different ORs.

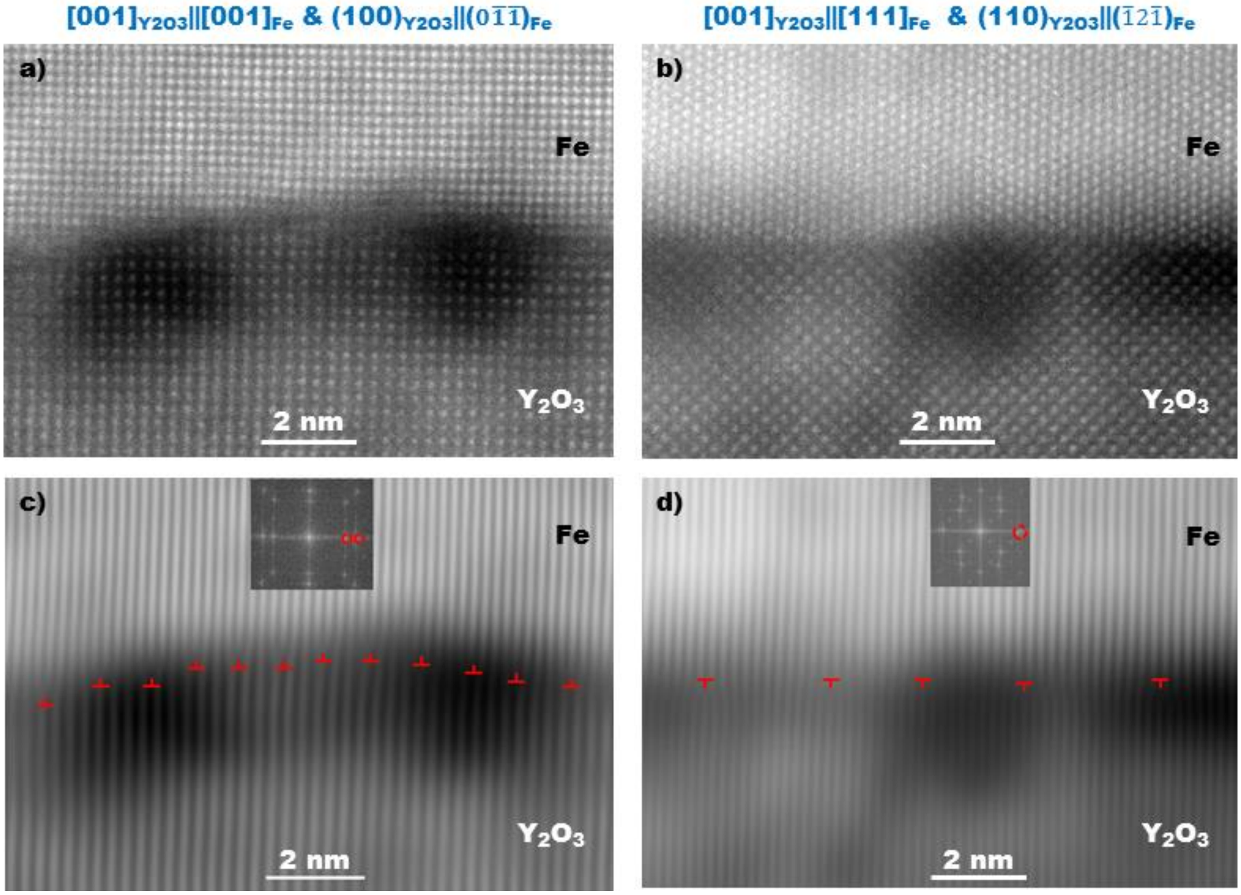

Figure 6-15: High resolution image of He bubbles nucleating at (a) YSZ(100)/Y_2O_3/Fe interface with OR2 (c) YSZ(110)/Y_2O_3/Fe with OR3. (c and d) are the iFFT images obtained with the spots shown in inset. The bubbles preferentially nucleate on the oxide film side, even when misfit dislocations are located in the Fe layer, as shown in (c).

As can be seen, the lattice mismatch between the two films causes the formation of a very high density of MDs on the Fe side. Nonetheless, the interface bubbles clearly nucleate at the oxide side of the interface. Moreover, it appears from the high resolution images that the interface, initially flat, becomes wavy as a result of the presence of the bubbles. Even in this case, bubbles do not overlap across the interface, as can be seen by the bubble surface which clearly terminates where the atoms of the Y_2O_3 terminate at the interface.

Bubble size was also investigated for bubbles along different orientation relationships, but a conclusive difference in bubble size was not found. An analysis on several bubbles imaged along metal/interfaces with different orientations led to an average size of 2.23 ± 0.31 nm. **Figure 6-16** shows the average bubble in the Y_2O_3 and Fe interlayer, and on the metal/oxide interface.

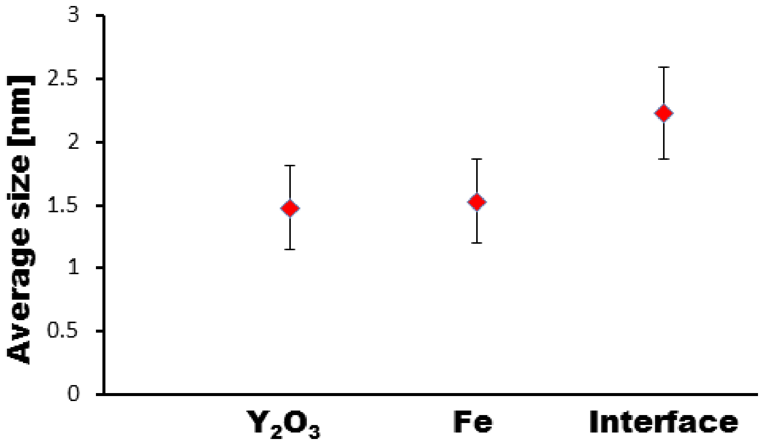

Figure 6-16: Average bubble size in Y_2O_3 layer, Fe layer and metal/oxide interface.

The specific ORs between Fe and the Y_2O_3 layers can be readily determined from HR images (by indexing the corresponding FFT). However, the misalignment angle between the Y_2O_3 and the Fe films at patches of interfaces without specific ORs cannot be determined in this manner. Misalignment angles could be eventually determined by indexing Convergent Beam Electron Diffraction (CBED) patterns. However, because no differences in bubble size at the interface were observed between different ORs and between patches with a defined OR and without, relative misalignment angles in patches without a defined ORs were not determined.

Figure 6-12 c) shows several bubbles nucleating on a general grain boundary in the Fe film. A detailed analysis of the bubble nucleation on these sites was not performed, but it was clear that when bubbles nucleate on a grain boundary, they symmetrically overlap across the boundary. This is an interesting observation and in drastic contrast with what was observed at the metal/oxide interface, where the bubbles nucleated on the oxide side and only wet the interface. No overlap of the bubbles across the interface was observed in all the analyzed bubbles at the metal/oxide interface. Moreover, bubbles nucleating at the grain boundaries are not significantly bigger than bubbles nucleating in the grain interior. An increase in bubble size is observed only at the metal/oxide interface.

To understand the reasons for which bubbles close to the interface nucleate on the oxide side and only wet a small part of the interface, rather than overlapping across it, wetting arguments can be used. Considering the three different phases A, B and C in contact, the contact angle of their surfaces is determined by the ratio of their interfacial energies γ_{AB}, γ_{BC} and γ_{AC} where the condition $\gamma_{ij} < \gamma_{ik} + \gamma_{jk}$ must be obeyed, indicating that no one interfacial energy can be larger than the sum of the other two. When the interfacial energy is uniform, and A and B are the same phase, the bubbles would overlap across the boundary, as seen for the bubbles nucleating at grain boundaries in the Fe layer.

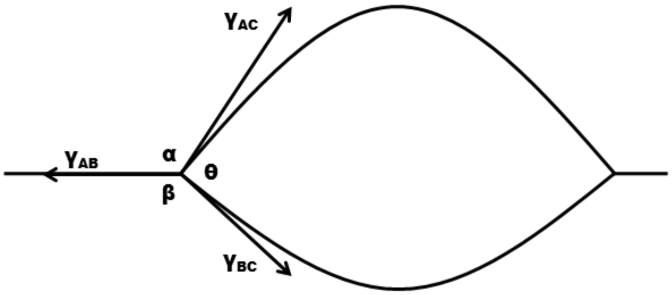

Figure 6-17: Schematic illustration of wetting for interface with uniform surface energy.

However the situation is different when the two constituents of the interface have different surface energies, as in the case of Y_2O_3 and Fe. We can define a wetting energy parameter W [196] as:

$$W = \gamma_A + \gamma_{AB} - \gamma_B \qquad \text{Equation 6-3}$$

with $\gamma_A < \gamma_B$. Thermodynamics favor wetting when W > 0, and the bubble or void will nucleate inside phase A, in contact with the interface. On the other hand when W < 0 wetting is not favored and the void can minimize its energy by nucleating entirely inside the phase. Experimentally determined values of the surface energy of iron varies between 2.36 J/m^2 [197] and 2.47 J/m^2 [198], while DFT simulations yield values ranging between 2.22 J/m^2 and 2.73 J/m^2 [199], depending on the specific surface. Surface energy of Y_2O_3 is instead quoted as 1.66 J/m^2 [138]. It is this difference in surface energy which explains why the bubbles nucleate at the interface from the oxide side, without overlapping across the interface. Nucleation of bubbles contained in both the individual layers is then most likely due to the very high dose injected inside the sample and the existence of only one interface. If a multilayer is to be synthesized, with a relatively small individual layer thickness, it is likely that bubbles would nucleate at the metal/oxide interfaces alone. Alternatively, a lower dose irradiation performed at high temperature might have yielded the same result, as demonstrated in Ref. [196]. It is also interesting note that independently by the character of these metal/oxide interfaces (semi-coherent or incoherent), the experimental observation of wetting at the metal/oxide interface allows, from Equation 6-3, to set a lowest value for the interfacial energy of 0.7 J/m^2. This energy value is consistent with the value of semi-coherent interfaces. The observation of bubble wetting at the interface from the oxide was made independently of the relative ORs of the samples. **Figure 6-18** shows HR images of helium bubbles nucleating at an interface with OR2 grown on YSZ(100), OR3 grown on YSZ(110) and with no OR grown on YSZ(100). It can be also observed that bubble sizes are comparable and independent of the samples' ORs.

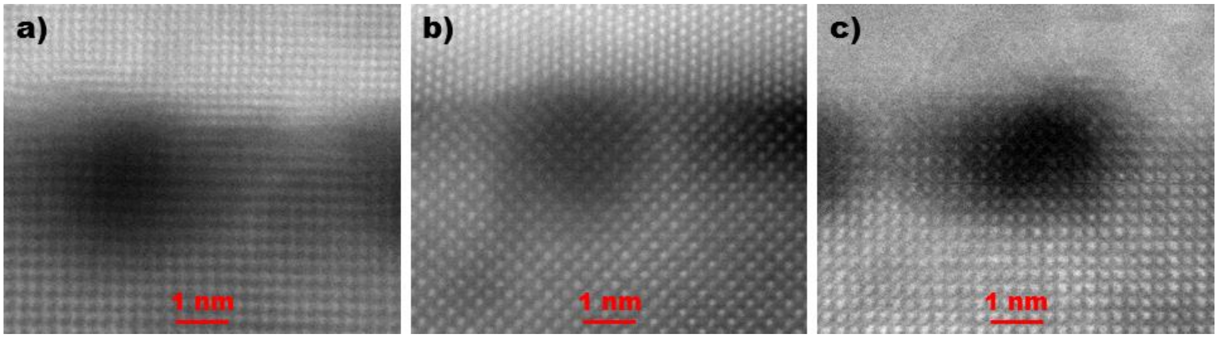

Figure 6-18: HR images of bubbles at Y_2O_3/Fe interface (a) YSZ(100)/Y_2O_3/Fe OR2 (b) YSZ(110)/Y_2O_3/Fe OR3 and (c) YSZ(100)/Y_2O_3/Fe random orientation.

6.3 Conclusions

This section of the thesis focused on nucleation of helium bubbles at differently oriented Y_2O_3/Fe interfaces. The bilayer film samples were prepared by first growing Y_2O_3 as flat epitaxial thin films on the YSZ substrate and subsequently Fe films were deposited on these samples. For the samples grown on the YSZ(100) substrate, the deposited iron formed a continuous, relatively flat film. For the samples grown on the YSZ(110) substrate, the deposited iron formed mostly 150 nm wide islands. Because the two depositions were performed under similar conditions, differences in the film morphology may be due to differences in either surface energies of the two Y_2O_3 layers, or the fact that the Fe follows the geometry of the underlying Y_2O_3 layer (flat for the (100) surface, irregular for (110) surface). Once metal/oxide interfaces with different ORs are synthesized, they can be readily used as valid templates for helium implantation studies.

Statistical analysis on the bubbles did not yield a significant difference, in regards to bubble size for different ORs and between interfaces with specific ORs and incoherent interfaces. Moreover, bubbles were seen to nucleate at random locations at the interface, and not in specific sites such as MDs, which theory predicts to be preferential nucleation sites. However it must be noted that for the synthesized interfaces, MDs density was extremely high, so it would not be probable for bubbles to nucleate at every MD. Detailed high resolution TEM examination showed the metal/oxide interface to be preferential nucleation site for helium bubbles. Although a difference in bubble size was expected to be observed is function of the interface character, the fact that every metal/oxide interface is effective in sequestrating He is a valuable observation. Real ODS steels and NFAs, for example, will in fact have a population of oxide particles possessing interfaces with different characters. The observation that all interfaces can be potentially effective He nucleation sites, independently of their interfacial character, suggests the ability of these alloys to effectively resist helium embrittlement and swelling. Moreover, bubbles observed at grain boundaries in iron were observed to have a size comparable to bubbles observed in the interior of the grains. This is a very interesting observation. These observations confirm the metal/oxide interface to be very efficient sites for He bubbles nucleation, more than grain boundaries. Finally, bubbles nucleating at the metal/oxide interface nucleate from the oxide side and only wet the interface, never growing across this boundary. This is due to the different surface energies of the oxide and the metal films, and confirms the intrinsically different character of these interfaces, as compared from example to grain boundaries. These observations have important implications on the expected behavior of the commercial alloys - bubbles nucleating at the metal/oxide interface and growing inward to the oxide will have a maximum size limited by the size of the oxide particles, which in turns is limited in most cases to few nanometers. Thus the presence of a great number of oxide particles inside the matrix is indeed very beneficial in sequestering He and retarding or even suppressing embrittlement caused by He formation and accumulation at various sites.

CHAPTER 7

Radiation endurance in Al_2O_3 nanoceramics

In order to increase power conversion efficiencies, Gen IV nuclear reactors will operate at higher temperatures than conventional Gen II and III nuclear reactors. In order to access the high temperature range (i.e. between 400°C-1000°C), coolants other than water must be utilized. The most promising coolants in this regard include supercritical water, high temperature helium gas, molten salts, and liquid metals such as lead, and lead-bismuth or lead-lithium eutectics and sodium. These coolants are also expected to improve neutronics of the reactor system. On the other hand, most of these coolants are very corrosive and detrimental to the reliability of in-core components [5], and their inherently corrosive effects are augmented by high temperatures and high degree of radiation damage that these reactors are expected to experience [10]. In this context, ceramics represent a promising class of materials due to their high temperature strength and relatively high chemical inertness in several corrosive environments. The main issue with monolithic ceramics is their lack of plasticity at low homologous temperatures, which makes them inherently brittle. This fact excludes their utilization as structural materials due to concerns of catastrophic failure. Even though extrinsic toughening is an appealing route to overcome brittleness [72], the widespread utilization of ceramics for structural components is difficult. On the other hand, the deposition of ceramic coatings or thin films on metallic structural materials can provide corrosion resistance without affecting structural requirements. It is worth highlighting that protective coatings are already being considered for accident tolerant fuel cladding for LWRs [76]. In the case of Generation IV concepts and fusion systems, coatings could be used to mitigate high temperature corrosion [5,15] and tritium permeation [200]. The dimensional changes induced by thermal creep, radiation damage, and their synergistic interactions can produce large stresses and strains at the coating-substrate interface. Therefore, an ideal coating must be able to accommodate such conditions while retaining both adhesion and structural integrity. For this reason, the mechanical performance of a given ceramic coating, particularly toughness is extremely important. Room temperature processing would be an asset, in order to avoid microstructural changes in the substrate material. Furthermore, in order to ensure the longevity of structures, an ideal coating must also be designed to withstand unparalleled radiation damage levels, particularly if they are used for in-core components such as cladding. On account of their fine grain size, *nanoceramic* coatings may benefit from the strength and chemical inertness of ceramics, combined with many favorable deformation modes [201–203] and with the generally high radiation tolerance already demonstrated in nanomaterials due to large internal interfacial area [68–70,95,204–207]. Oxide nanoceramics in particular are a promising class of coating materials owing to their compatibility with a wide range of environments, including light water, liquid metals and high temperature helium[5,15,76]. The structural response of oxide nanoceramics to irradiation is usually characterized by an increase in the average grain size, as demonstrated for irradiated ceria thin films [182–184], zirconia thin films [184] and bulk yttria-stabilized zirconia [185]. However, the mechanical response of irradiated oxide nanoceramics remains largely unexplored. In this chapter, the evolution of the nanometer-scale structural features as a function of radiation and their correlation to mechanical properties in Al_2O_3 nanoceramic thin films are studied. The damage exposures tested are 20, 40 and 150dpa with irradiations being conducted at 600°C. Such high levels of radiation damage approach or even exceed the damage exposures anticipated for next generation nuclear systems. Scientifically speaking, thin films are convenient model systems and are often used to study the fundamental effects of radiation on bulk nanocrystalline materials, as has also been demonstrated earlier in this research.

7.1 Film Design Considerations

An important factor that must be taken into consideration when designing coatings is the mismatch of the thermal properties with the substrate, especially mismatches in coefficient of thermal expansion (CTE). While an investigation on the CTE of the coatings is beyond the scope of this work, generally, in the case of ferritic/martensitic steels used for cladding material such as T91, the mismatch with alumina films is probably not large enough to cause concerns. For austenitic alloys, the CTE is higher, [208] and in this case heating or thermal cycling could compromise the substrate-coating system. Improvements in this regard can be can be achieved using interfacial bond layer of the type MCrAlY (M usually stands for Fe, Ni, or Ni+Co). This approach has been used for applications such as gas turbines, where thermal cycling and thermal shock are significant challenges [209,210]. The primary function of the interlayer or the bond layer is to provide plasticity at the interface to accommodate strain and provide graded film-substrate system. The bond layer itself should be quite resistant to corrosion should there be a breach of the top layer and this regard bond layers comprising Al are frequently used so as to form a protective scale of α-Al_2O_3 to avoid oxidation of the substrate, and maintain cohesion with the coating. Similarly, the use of FeCrAlY alloys as bond-coats in LFRs can provide a defense-in-depth approach to the challenge of corrosion protection. Provided the thermodynamic conditions were favorable, the bond layer could form a protective Al_2O_3 scale upon a hypothetical breach of the ceramic topcoat during operation. Oxygen injection could also be used to passivate potential defect sites in the as-deposited state, or zones damaged during transport and handling. As far as radiation damage is concerned, FeCrAlY bonding layers could be expected to behave as bulk FeCrAlY alloys which are being considered for accident tolerant claddings in LWRs, for example. Nevertheless, features like nano-porosity might further enhance the radiation tolerance of this class of swelling resistant alloys [211]. A systematic investigation on the role of composition, structure and thickness of the bond layer is beyond the scope of the study.

Last, but not least, residual stresses may have a detrimental effect on adhesion strength,. Such stresses can be managed mainly by adjusting temperature or thickness, if the former is to be kept low (i.e. the higher the thickness, the greater the compressive stress state). For amorphous-Al_2O_3 grown by PLD at room temperature (samples used in this research), the residual stresses are known to be highly compressive, with a value of -500 MPa for a thickness of 1 µm [212]. On one hand, compressive stresses may provide a safety margin from undesirable tensile conditions from strain in the fuel cladding. On the other hand, excessive compressive stresses must be avoided, since it could cause buckling and/or delamination. In addition, the minimum coating thickness should be limited by the requirement of uniformity. The experience gained in the frame of previous investigations shows that a good compromise can be achieved by selecting the thickness between 1 µm and 10 µm.

To sum up the system, the architecture of the coating comprises a compact Al_2O_3 top-film and a columnar FeCrAlY bonding layer in the case of 1515Ti and 316L austenitic alloy substrates. The structure of the ceramic topcoat is amorphous by design. This amorphous phase is expected to evolve towards a nanocrystalline state during irradiation, and to stabilize in a condition in which radiation damage is totally or partially self-healed through interaction with grain boundaries. The bond layer is processed by RF-sputtering or PLD, while the ceramic top film is grown by PLD. **Figure 7-1** shows a SEM cross sectional image of a coated steel substrate.

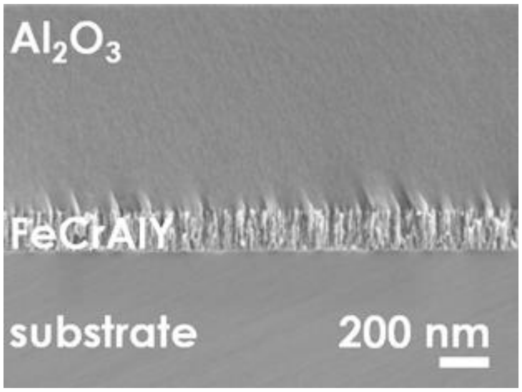

Figure 7-1: SEM cross sectional image of a 1515Ti steel coated with a 200 nm bond layer of FeCrAlY and 2 μm of Al_2O_3 nanoceramic top film.

7.2 Materials and Methods

The alumina films were grown by PLD in a stainless steel vacuum chamber on stainless steel substrates (10 x 25 x 1 mm^3) at room temperature. The steel plates were polished using successively finer grits of SiC grinding paper (final step 1200 grit), ultrasonically cleaned in acetone and isopropanol, and rinsed in isopropanol. Further cleaning procedures included in situ by pre-sputtering. The substrates were austenitic steel plates, either grade 316L or 1515Ti. The plates were 3 cm long, 1 cm wide, and 1 mm thick. The nominal composition of the 316L plates was 16.8Cr-10.2Ni-2.1Mo-1.8Mn-0.6Si-0.02C-balance Fe (wt.%). The nominal composition of the 1515Ti plates was 14.9Cr-15.1Ni-1.6Mn-1.4Mo-0.8Si-0.4Ti-0.09C-balance Fe (wt.%). In all cases, a 200 nm thick FeCrAlY film was used as an interlayer (i.e., bond layer) to buffer dimensional changes due to swelling of the substrate The exact composition of the FeCrAlY interlayer was16.9Cr-6.4Al-0.1Y-balance Fe (wt.%). This layer was deposited at room temperature by a RF sputtering source operated at 5 W/cm^2 in an Ar environment (5 Pa, with an initial base pressure of 1.5.10^{-3} Pa), with an incidence angle of 45° and a target-to-substrate distance of 70 mm. The oxide films were deposited with a GSI Lumonics (USA) KrF pulsed laser system in the UV range (248 nm) to ablate a 99.99% pure polycrystalline alumina target with an incidence angle of 40° and a pulse repetition rate of 20 Hz. Thickness of the film was in the range between 1.3-1.5 μm.

7.2.1 Heavy Ions Irradiations

In this study, the ion energies were chosen to implant and irradiate to depths beyond the thickness of the thin films and into the substrate, avoiding chemical and interstitial injection effects. Sets of four samples were irradiated at the JANNUS-Saclay platform [213]. Two ion beams are employed simultaneously, namely 12 MeV Au^{5+} ions and 18 MeV W^{8+} ions. This was done in order to maximize the injected dose in the allotted time. The angle of incidence was 15° for both beams, and the total irradiated area was 3.14 cm^2 (≈0.78 cm^2 for each sample). The irradiation was carried out in vacuum (10^{-5} Pa) at 600°C. This temperature was in the typical range of operating temperatures for Generation IV reactors [5]. The temperature was continuously monitored, and was held constant throughout the experiment. In order to obtain results consistent with the model employed in the SPECTER code (which is used to calculate dpa levels from neutron irradiations), the damage exposures were calculated from the ion fluences with the Stopping Range of Ions in Matter (SRIM) software [19] according to the procedure recently described by Stoller et al [20]. The ion fluences were calculated by integrating the flux measured by Faraday cups that were periodically interposed between the ion beams and the samples. The damage levels reached were 20 dpa $(1.20 \cdot 10^{16}\, W^{8+}cm^{-2} + 1.74 \cdot 10^{16}\, Au^{5+}cm^{-2})$, 40 dpa $(2.13 \cdot 10^{16}\, W^{8+}cm^{-2} + 2.76 \cdot 10^{16}\, Au^{5+}cm^{-2})$ and 150 dpa $(4.52 \cdot 10^{16}\, W^{8+}cm^{-2} + 1.2 \cdot 10^{17}\, Au^{5+}cm^{-2})$. **Figure 7-2** shows the sample stage configuration for these irradiatons.

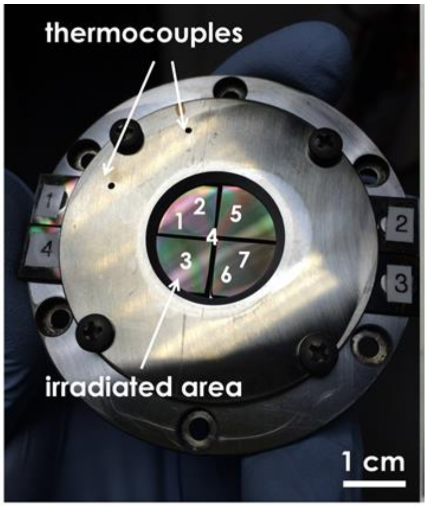

Figure 7-2: Sample stage configuration for the heavy ion irradiations of alumina nanoceramic films.

7.2.2 Characterization

7.2.3 Nano indentations

Quasi-static load-controlled indentations were performed at room temperature using a Micromaterials Nanotest system equipped with a Berkovich diamond tip. The indentations were applied in multiple arrays of nine indentations each. The maximum load was 10 mN, corresponding to penetration depths below one tenth of the thickness of the thin films. In all the tests, the maximum load was held constant for 5 seconds, in order to allow creep strain to develop. A 60 second holding was set at 20% of the unloading curve to measure thermal drift. Machine compliance and thermal drift were taken into account by assuming a constant rate throughout the test. The mechanical properties of the material (e.g. the Young's modulus E and hardness H) were assessed from the load-displacement curves following the Oliver and Pharr approach. E is computed from the reduced Young's modulus E_r through the equation:

$$\frac{1}{E_r} = \frac{(1-\upsilon^2)}{E} + \frac{(1-\upsilon_d^2)}{E_d} \qquad \text{Equation 7-1}$$

where υ, υ_d and $E_d$and are the Poisson's ratio of the material, and the Poisson's ratio and the Young's modulus of the diamond tip, respectively. The Young's modulus E was deduced from E_r assuming that υ decreases inversely as E_r (due to crystallization and grain growth). Note that variations of ±10% on the assumptions of υ yield variations of E of roughly 5 %.

7.2.4 Electron Microscopy Observations

Samples for TEM and ADF-STEM analysis were fabricated by cutting a thin lamella using conventional FIB (Focused Ion Beam) techniques. The last step of the sample preparation involved low energy (2 KV) low current (100 pA) polishing of the lamella at ±6º (with respect to the ion beam) to minimize the damage caused during the previous steps. TEM and ADF-STEM observations were performed with a FEI Titan (S)TEM from FEI. The diffraction contrast dominated image formation of ADF is preferred over the mass contrast dominated imaging provided by HAADF imaging, resulting in clear imaging of the GBs in the nanoceramic film.

For each damage level, the grain size was obtained from the measurement of the length of fifty randomly selected grains along two directions, namely coincident and orthogonal to the direction of the maximum length of each grain.

The crystalline phases present in the irradiated nanoceramic were analyzed by x-ray diffraction (XRD). The data were obtained using a Bruker D8 X-ray diffractometer, with Cu-Kα radiation in the Bragg-Brentano geometry.

7.3 Results and Discussion

7.3.1 Radiation Response of the Coatings

The Bright-Field TEM micrographs shown in **Figure 7-3** display the nanostructure of the as-deposited Al_2O_3 thin films. The dark contrast spots correspond to randomly-oriented ultra-fine nanocrystalline γ-Al2O3 domains (6 ± 4 nm), and consequently a large internal interface area, whereas the bright contrast results from the presence of the amorphous phase of Al_2O_3. The appearance of a relatively sharp ring, together with a diffused intensity halo in the diffraction pattern (DP) confirms that the material consists of a dual phase structure, with the amorphous phase dominating the overall structure. The volume fraction of γ-Al2O3 nanocrystalline domains is very low at approximately 1 vol. %.

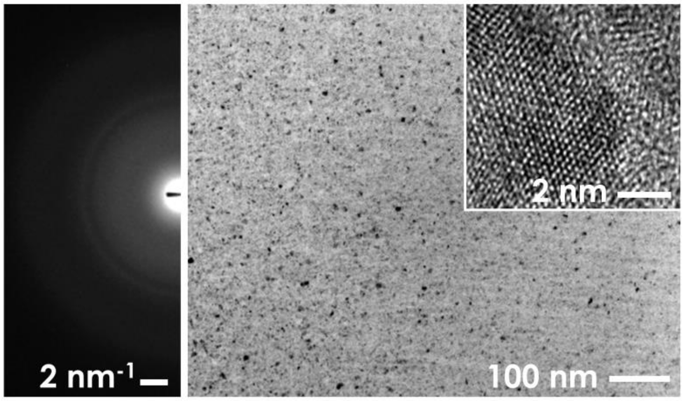

Figure 7-3: BF-TEM micrograph, and high-resolution (HR) close-up (inset) of the nanostructure of the as-deposited Al_2O_3 thin films showing a homogeneous dispersion of a low volume fraction of randomly-oriented nanocrystalline Al_2O_3 domains in an amorphous Al_2O_3 matrix.

The crystalline phase present in the as-deposited thin film was analyzed by DP indexing in samples grown directly onto TEM grids with an amorphous carbon support. The films were 50 nm thick. **Figure 7-4** shows a dark field DF micrograph of the structure of the as-deposited pristine nanoceramic (**Figure 7-4** (a)), together with the corresponding DP and the azimuthally integrated profile (**Figure 7-4** (b)). The profile is consistent with γ-Al2O3 according to card ICSD 30267. Based on the DF-TEM micrograph shown, the volume fraction of the γ-Al2O3 domains dispersed in the amorphous matrix is about 0.34%. However, since not all the nanocrystalline domains diffract under the particular condition used for the micrograph (which is obtained by selecting just a fraction of the most intense rings in the DP, roughly 120° wide), the actual volume fraction is higher –at least by a factor of 3. Thus, it is estimated that the actual volume fraction of the γ-Al2O3 domains is about 1%.

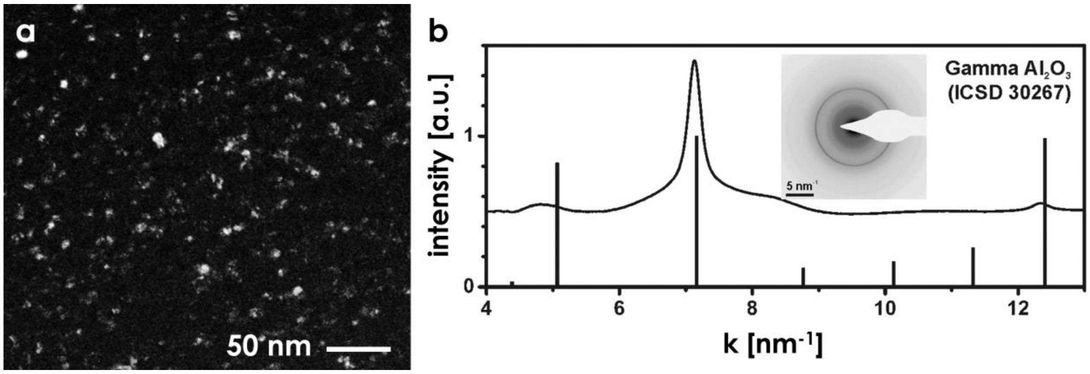

Figure 7-4: (a) DF-TEM micrograph of the as-deposited pristine alumina nanoceramic and (b) azimuthally integrated DP profile which is compatible with γ-Al2O3.

Figure 7-5 shows the implantation depth profiles for the 12 MeV^{5+} Au and 18 MeV W^{8+} ions as simulated by SRIM, together with the resulting radiation damage profile of the irradiation. As can be seen, peaks for the 12 MeV Au^{5+} ions and the 18 MeV W^{8+} ions are beyond 1.6 μm and 2 μm from the surface of the samples, respectively.

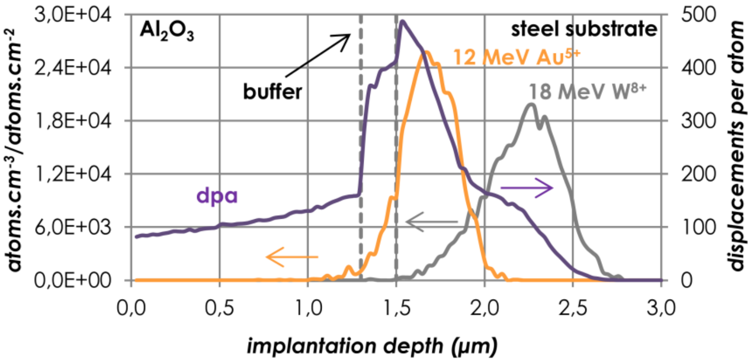

Figure 7-5: Implantation depth for 12 MeV Au^{5+} and 18 MeV W^{8+} ions, together with the resulting damage profile. Note that the ions are implanted beyond the thickness of Al_2O_3 thin film and into the substrate.

High-angle annular dark-field – scanning TEM (HAADF-STEM) observations coupled with energy-dispersive X-ray spectroscopy (EDS) confirm that the 12 MeV Au^{5+} ions are implanted beyond the thickness of the nanoceramic film and into the substrate, as shown in

Figure 7-6. The 18 MeV W^{8+} ions are lighter and more energetic than gold ions. Therefore, these ions can be expected to be implanted beyond the thickness of nanoceramic film. This statement cannot be verified directly with reasonable reliability by EDS mapping due to the superimposition of the relevant EDS peaks for W with the ones from other elements present in the sample (e.g. Au).

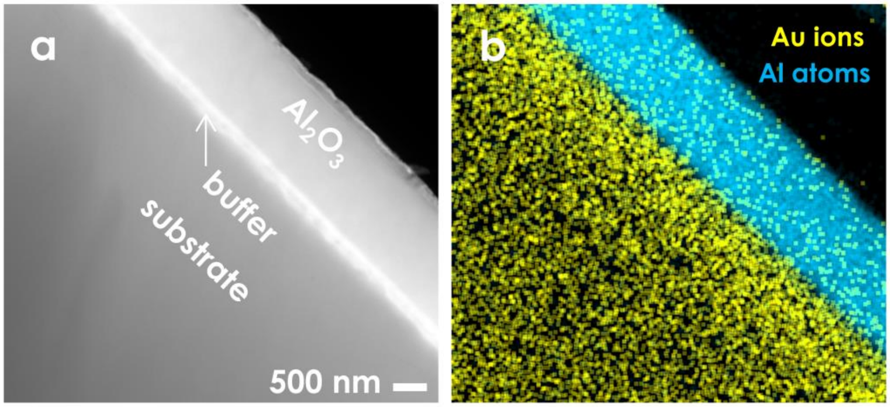

Figure 7-6: (a) HAADF-STEM micrograph and (b) EDS map showing that Au ions are implanted beyond the thickness of the nanoceramic thin film. In (b), the implanted Au ions are shown in yellow, whereas the Al atoms of the Al_2O_3 thin films are shown in blue.

Figure 7-7 shows the XRD spectra collected from pristine samples, and after 20 dpa, 40 dpa and 150 dpa. The as-deposited thin films are amorphous, and the only peaks observed are attributed to the austenitic steel substrate (card ICCD PDF 04-002-1864). However, the XRD spectra of the irradiated samples reveal the presence of crystalline peaks of γ-Al2O3 (card ICCD PDF 00-050-0741). Only the XRD spectrum of samples exposed to 150 dpa reveals the presence of a new phase –namely, α-Al2O3 (card ICCD PDF 00-011-0661). A systematic study is necessary to establish is the mechanism for this phase transition.

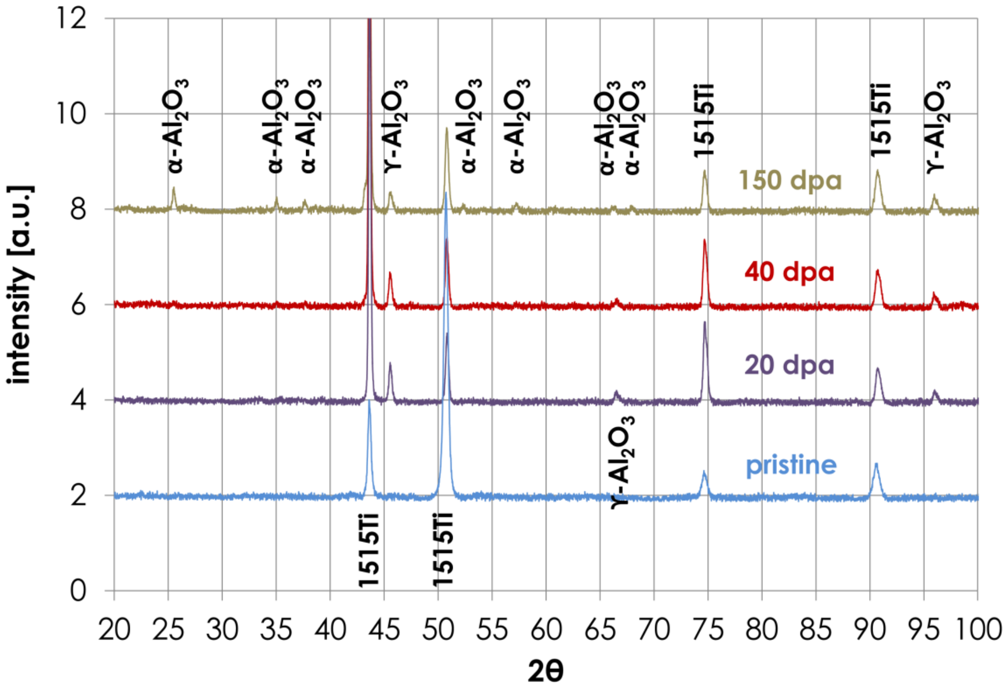

Figure 7-7: XRD spectra of the as-deposited pristine and the irradiated Al_2O_3 thin films. The pristine material is amorphous. The irradiated samples exhibit peaks corresponding to γ-Al2O3. α-Al_2O_3 was also observed in samples exposed to 150 dpa.

The main advantage of this type of dual structure (amorphous and gamma alumina) over a fully nanocrystalline structure is that it confers an unusual ensemble of metal-like mechanical properties (Young's modulus $E = 195 \pm 9$ GPa, $\upsilon = 0{,}29 \pm 0{,}02$) and moderate hardness ($H = 10 \pm 1$ GPa) to the Al_2O_3 thin films. In particular, the amorphous matrix precludes grain boundary interface sliding, enables plastic deformation and inhibits crack nucleation [214]. Despite the lower hardness compared to single crystal sapphire ($Hsapphire = 27.6 \pm 2$ GPa) [215], the Al_2O_3 thin films are still significantly harder than most metallic materials. Moreover, the resulting H/E ratio (i.e. 0.051) is comparable with the H/E ratios of superhard nanocomposite coatings for tribological applications [216]. This may be beneficial for example during fuel rod insertion or grid-to-rod failure during operation.

The ADF-STEM micrographs in **Figure 7-8** show the structural features of the as-deposited and the irradiated thin films.

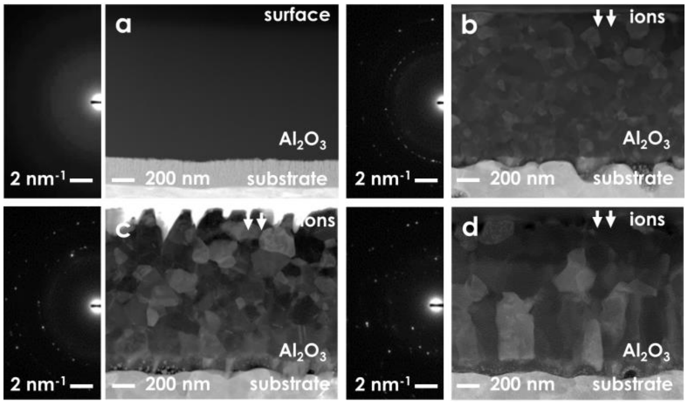

Figure 7-8: (a) ADF-STEM micrographs and DPs showing how an initially metastable form of Al_2O_3 (b) undergoes nanocrystallization and growth after irradiation at 600°C up to 20 dpa, (c), 40 dpa, and (d) and 150 dpa. The coarsening induced by irradiation releases excess free energy and occurs due to the interaction between point defects and GBs [217]. The scale-bars are 200 nm for the STEM micrographs and 2 nm^{-1} for the DPs.

These images indicate that a fully nanocrystalline structure is realized upon irradiation, and that extended irradiations induce grain growth as the dpa levels are increased. The average grain size increases from 6 ± 4 nm to 101 ± 56 nm at 20 dpa, 153 ± 62 nm at 40 dpa and 293 ± 85 nm at 150 dpa (**Figure 7-8** (b-d)). The crystallization and grain growth observed manifest as evolution of DPs with a diffused intensity halo to rings and eventually to isolated spots. The crystalline phases present in the irradiated nanoceramic are γ-Al_2O_3 up to 40 dpa, and both γ-Al_2O_3 and α-Al_2O_3 at 150 dpa. Phase analysis was performed on the film using TEM. **Figure 7-9** shows aberration corrected STEM micrograph from external and internal grains of the film. Several of these grains were imaged and several DPs were collected and analyzed. This analysis showed that the most internal grain of the coating are α-Al_2O_3 while the most external grains are γ-Al_2O_3.

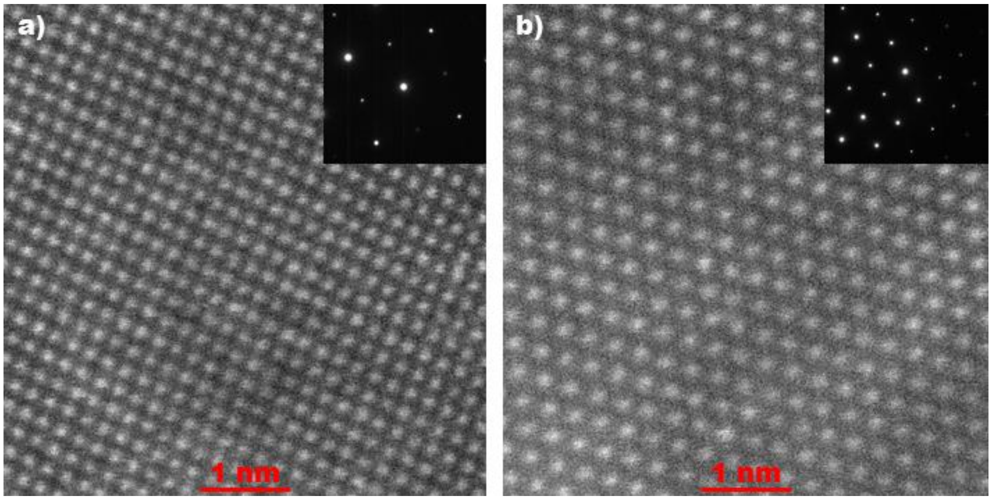

Figure 7-9: Phase analysis in the Al_2O_3 coating irradiated to 150 dpa (a) aberration corrected STEM image of external grain of the Al_2O_3 coating and (b) internal grain of the Al_2O_3 coating with relative DPs in inset. Internal grains of the coating are identified as α-Al_2O_3, while the most external ones are γ-Al_2O_3.

It is worth highlighting that the irradiation did not induce any loss of adhesion or delamination effects at the thin film-substrate interface. The combined effect of irradiation and strain imposed by the substrate (for instance, due to thermal and irradiation creep or swelling) is beyond the scope of this study, and warrants further investigation. It is likely that temperature plays an important role in determining the kinetics of the structural evolution. However, it is possible to attribute crystallization and grain growth to the sole effect of irradiation, based on *in-situ* TEM annealing and ion irradiation at the JANNUS platform of CNRS-Orsay. Structural details on a nanoscale were performed with a 200 kV Tecnai G20 TEM equipped with a custom polar piece, coupled to an ion accelerator. Both annealing and the irradiation were performed in vacuum (10^{-5} Pa) at 600°C, and the irradiation was performed with 150 keV Ni^{2+} ions up to a fluence of 2.88×10^{16} ions/cm^2, which corresponds to about 25 dpa. The samples were prepared by depositing 30 nm thick Al_2O_3 films directly onto 200 µm thick silicon TEM grids with a 20 nm thick amorphous Si_3N_4 membrane support. **Figure 7-10** how structure of the nanoceramic evolves.

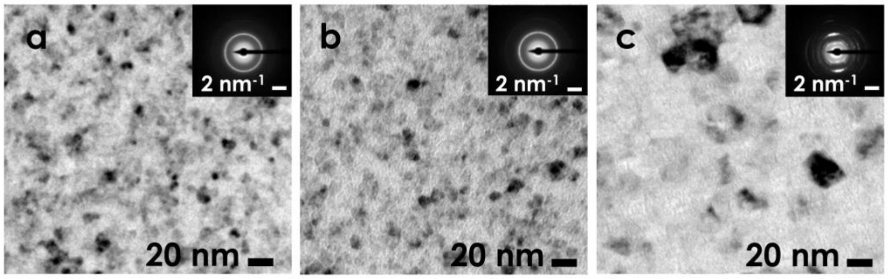

Figure 7-10: TEM micrographs and DP insets showing the structure of the nanoceramic in (a) its pristine condition (b) after annealing for 90 minutes at 600°C, and (c) and after irradiation for 90 minutes (roughly 25 dpa) at 600°C. Crystallization and grain growth are observed only in the irradiated sample.

The maximum grain size is below 12 nm. No discernible crystallization or grain growth was observed during annealing for 90 minutes at 600°C (**Figure 7-10** (b). This observation is also confirmed by the fact that the DPs shown as insets remain unchanged. By contrast, irradiation at 600°C for 90 minutes induces crystallization and coarsening, as shown in **Figure 7-10** (c). The maximum grain size after irradiation exceeds 20 nm. The discretization and the appearance of new rings in the DP (inset of **Figure 7-10** (c) provide further evidence of the onset of structural rearrangements following irradiation. Conclusive evidence of the observation that crystallization and grain growth are only due to irradiation is provided by systematic observations of the masked region (e.g. an unirradiated region) of irradiated samples. The TEM observations show that no crystallization occurs at the irradiation temperature (600 °C) for the entire duration of the experiments. **Figure 7-11** shows a TEM micrograph of the unirradiated region of a sample exposed to 150 dpa. In this case, the duration of the irradiation is roughly 24 hours. The micrograph does not reveal any appreciable structural rearrangement, as also confirmed by the DP, which remains basically unchanged compared to the pristine DP.

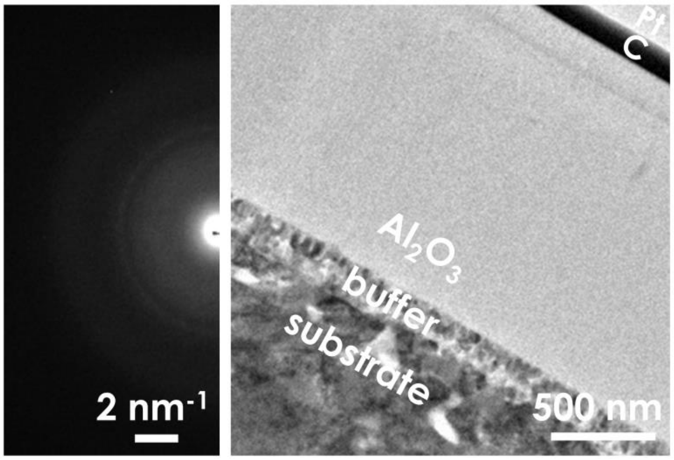

Figure 7-11: TEM micrograph and DP of an unirradiated region of a sample exposed to 150 dpa at 600°C. No structural rearrangements are caused by the thermal annealing in the nanoceramic.

The initial crystallization is expected to occur readily upon irradiation, and may be homogeneous [218], epitaxial [219,220] or both. The subsequent coarsening effect can be explained in terms of a fast disorder-driven mechanism, which is available even below room temperature [182,183], and which is governed by the capture of interstitials by GBs [69,70,207]. The incident ions introduce a large amount of local disorder through atomic displacement cascades. The disordered regions interact with GBs, releasing excess free energy and leading to an overall growth. It is also interesting to note that the extent of grain growth is strongly influenced by the total amount of energy injected by the ions into the material [184]. In the energy range investigated, the energy of the ions is transferred to the material both by electronic excitations and displacive damage (i.e. nuclear collisions). The effect of these different types of energy loss may be additive, synergistic or even competing. In the case of oxide nanoceramics, the effect is generally additive [184]. The plot in **Figure 7-12** shows the dependence of grain growth both on the total amount of energy injected into the material (KeV per target atom), and on displacive radiation damage (displacements per atom). The plot indicates that radiation-induced grain growth is a self-limiting process, which follows a sublinear dependence on damage exposure, in good agreement with previous results on other nanocrystalline oxides [182–185].

In the irradiated material, grain growth is accompanied by the formation of planar defects with two parallel flat boundaries. These defects are found occasionally, and their presence is independent of damage exposure. The defects are identified as twins, and an example is shown in **Figure 7-12** (b and c). The presence of a mirror-plane both in the high-resolution TEM (HR-TEM) micrograph and in the DP inset in **Figure 7-12**c confirms that the defects observed are indeed twins.

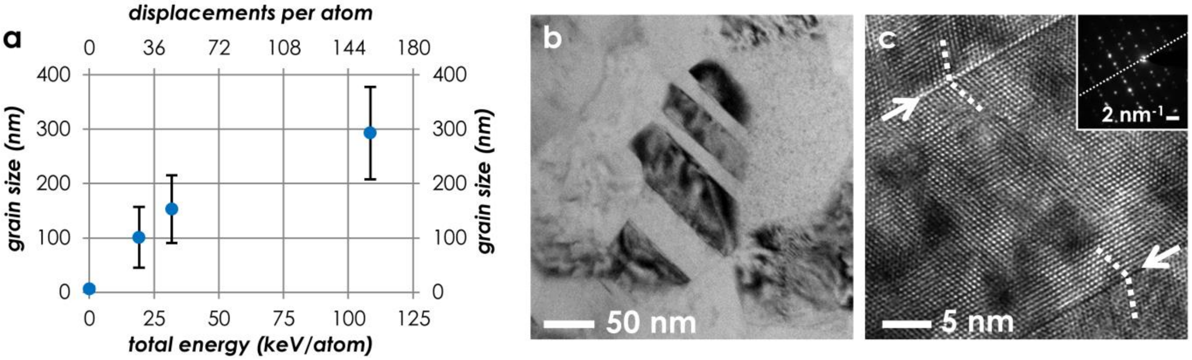

Figure 7-12: (a) Grain growth in the Al$_2$O$_3$ thin films as a function of total energy injection and displacive radiation damage. (b) The grain coarsening is accompanied by (b) the formation of twin boundaries, which release accumulated mechanical energy. (c)The presence of a mirror plane in both the HR-TEM micrograph (indicated by arrows), and in the DP inset confirms the twin relationship of the adjacent grains.

The formation of twins in nanocrystalline solids can be typically understood in terms of such mechanisms as nanoscale multiplane shear [221] or stacking fault formation led by Shockley partial dislocations [222]. From an energy perspective, the formation of twins during the irradiation of the nanoceramic thin film may be explained by the need to release the excess mechanical energy accumulated during incoherent grain coarsening.

It is worth emphasizing that the energy injection associated with the irradiation process is effectively dissipated through structural rearrangements that lead the material towards a more stable structural configuration, including crystallization, grain growth and twinning. Importantly, these rearrangements yield an improvement of the mechanical properties of the material. The changes in the mechanical properties as a function of radiation damage exposure were studied using nanoindentation, and the results are plotted in **Figure 7-13**.

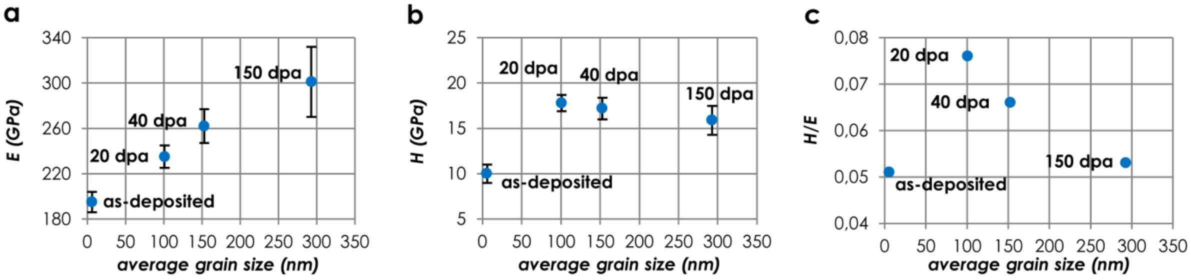

Figure 7-13: Effect of radiation-induced grain growth on the mechanical properties of Al_2O_3 nanoceramic thin films, namely (a) the Young's modulus E (b) the hardness H and (c) the hardness to Young's modulus ratio H/E . The trend of hardness is well-described by the Hall-Petch relationship, due to the increase of grain size with increasing damage exposures.

The reduced Young's modulus E_r increases monotonically with grain size,(i.e. $E_{r,20dpa}$ 205 ± 7 GPa to $E_{r,40dpa}$ 222 ± 10 GPa and $E_{r,150}$ 245 ± 19 GPa). Accordingly, the Young's modulus E increases from E_{20dpa} 235 ± 10 GPa to E_{40dpa} 262 ± 15 GPa and E_{150} 301 ± 31 GPa. The hardness H peaks at moderate damage exposures, varying from $H_{20dpa} = 17.8 \pm 0.9$ GPa, to $H_{40dpa} = 17.2 \pm 1.2$ GPa, and $H_{150dpa} = 15.9 \pm 1.6$ GPa. Notably, the trend is well described by the Hall-Petch relationship, whereby a material's strength and hardness decrease as the average grain size increases. The Hall-Petch relationship describes the measured hardness H_v according to the formula $H_v = H_0 + kD^{-1/2}$, where H_0 is the intrinsic hardness dependent on frictional lattice resistance to dislocation motion, k is the material-specific strengthening coefficient, and D is the average grain size. In this work, the best linear fit of H_v as a function of $D^{-1/2}$ yields $H_0 = 13.255$

GPa and k = 46.638 GPa.nm$^{1/2}$, with a coefficient of determination equal to $R^2 = 0.9756$. Below the so-called *strongest grain size* (typically in the range 10-20 nm [223]), the strengthening effect is balanced by GB shear (so mechanical properties are related to interfaces), which yields a reduction of hardness for decreasing grain size. This effect is usually referred to as the inverse Hall-Petch effect. A detailed overview of the mechanisms that yield an enhancement of hardness in nanoceramics has been recently reported by Veprek [223].

A direct comparison between the mechanical properties of the irradiated thin films and polycrystalline α-Al_2O_3 is difficult. The mechanical properties of the latter vary depending on the grain size, the presence of impurities and on the processing route [224]. However, comparisons can be made with bulk nanocrystalline (bnc) α-Al_2O_3. The reported hardness and stiffness for bnc-alumina with a grain size of 150 nm are $H_{bnc-alumina} = 25.5 \pm 0.3$ GPa and $E_{bnc-alumina} = 403$ GPa [225,226]. Here, the maximum hardness is reached when the average grain size is 101 nm ($H_{20dpa} = 17.8 \pm 0.9$ GPA). The corresponding Young's modulus is $E_{20dpa} = 235 \pm 10$ GPa. The differences observed are probably due to: (i) the presence of different phases (γ-Al2O3 versus α-Al2O3), (ii) the measurement method (Berkovich nanoindentation versus Vickers microindentation), (iii) the presence of radiation induced point defects, or (iv) combinations thereof. Another important implication of the observed irradiation-induced crystallization is that the H/E ratio of the thin films is enhanced in response to irradiation. The H/E ratio peaks at moderate damage exposures (when the volume fraction of GBs is the highest), varying from 0.051 for the as-deposited condition, to 0.076, 0.066 and 0.053 for 20, 40 and 150 dpa, respectively (Fig. 4c). These results suggest an improvement in service of the robustness of the thin films against wear. This may be of particular interest in applications such as liquid metal erosion [227] or rod-to-grid fretting [228].

Fracture toughness of ceramic materials is typically determined from nanoindentation tests by measuring the length of surface radial cracks emanating from the corner of indents. This type of measurement is not possible here because cracks were not observed due to the low load and the low film thickness. However, an indirect estimation of fracture toughness is provided by the *H*/*E* ratio [216]. The as-deposited material lacks long-range order and nanostructural defects (such as dislocations) that may shield stress and suppress crack openings. Thus, the attainable plasticity in the wake of a crack tip is limited, and any opening would be likely accommodated by unstable crack propagation. Accordingly, the *H*/*E* ratio of the pristine material is comparatively low. In contrast, the mechanical response of the irradiated material is mainly driven by GBs. The large volume fraction of GBs makes new energy dissipation mechanisms available (e.g., twinning). The resulting *H*/*E* ratio is higher, which suggests an enhancement of fracture toughness. Although coatings of thin films are not structural components, an enhancement of fracture toughness in service would be desirable. In this regard, a certain extent of cracking may be acceptable during the extended exposure to neutron radiation fields, while unstable crack propagation would certainly not be an option.

Additional qualitative evidence in support of the enhancement of fracture toughness is provided experimentally by nanoimpact tests. In these tests, a cube-corner diamond tip is periodically tapped against the surface of the thin films. The nanoimpact tests performed in this study provided qualitative evidence on the enhancement in-service of the fracture toughness of the Al_2O_3 nanoceramic. The results of the tests are plotted in **Figure 7-14** in terms of impact depth as a function of the number of impacts.

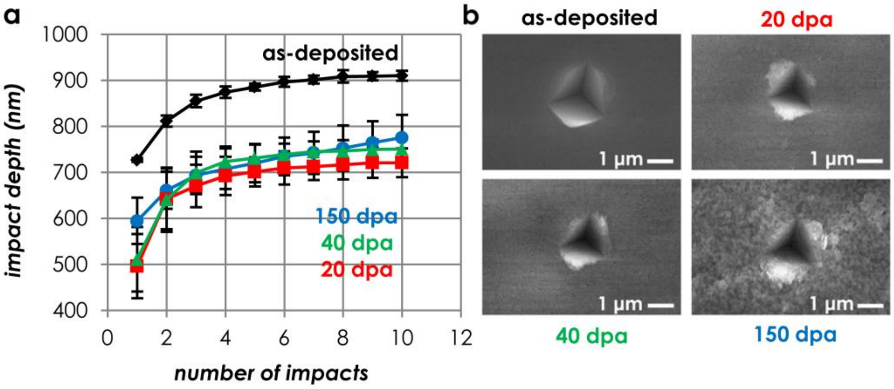

Figure 7-14: (a) Displacement curves for nanoimpact testing of the Al_2O_3 nanoceramic at 1 mN before and after irradiation up to 20 dpa, 40 dpa and 150 dpa (b) SEM micrographs on the right show the nanoimpact imprints.

The impact depth is the highest for the as-deposited thin films, suggesting that the impact energy is dissipated more efficiently in the irradiated samples. The absence of sharp variations in all the nanoimpact curves indicates that no major failure takes place in any of the tested samples, as confirmed by SEM analyses of the nanoimpact zones (**Figure 7-14** (b)). The evolution of impact depth is similar in all cases, meaning that similar mechanisms govern the impact response suggesting that the toughness is comparable. Regardless, the penetration is larger in the pristine material, which can be attributed in part to the lower hardness. In addition, the impact energy seems to be dissipated more effectively for samples irradiated up to 20 or 40 dpa, in good agreement with the trend for the *H/E* ratio (**Figure 7-13** c)). This fact is particularly clear during the first impact. Note that saturation is reached after several impacts because the applied force is distributed over increasing contact areas. In other words, the contact pressure decreases as the number of impacts increases.

The impact response of the as-deposited and the irradiated thin films is radically different. **Figure 7-15** displays the cross-sectional images of representative nanoimpact imprints for as-deposited and irradiated samples. Two SADPs are acquired for each cross-section, both distant from (white box) and within (yellow box) the impact zone (below and in the vicinity of the impact imprint). In the unirradiated samples (**Figure 7-15** (a)), impact energy is dissipated through shear banding, and no major structural rearrangements are induced by impact loading. This observation is confirmed by the fact that the SADPs gathered distant from and within the impact indent appear identical, as shown in **Figure 7-15** (d). **Figure 7-15** (b) **Figure 7-15** (c) show the cross-section of nanoimpact indents in samples exposed to 20 dpa (corresponding to the peaks of *H* and *H/E* ratio **Figure 7-13**) and 150 dpa (end-of-life exposure), respectively.

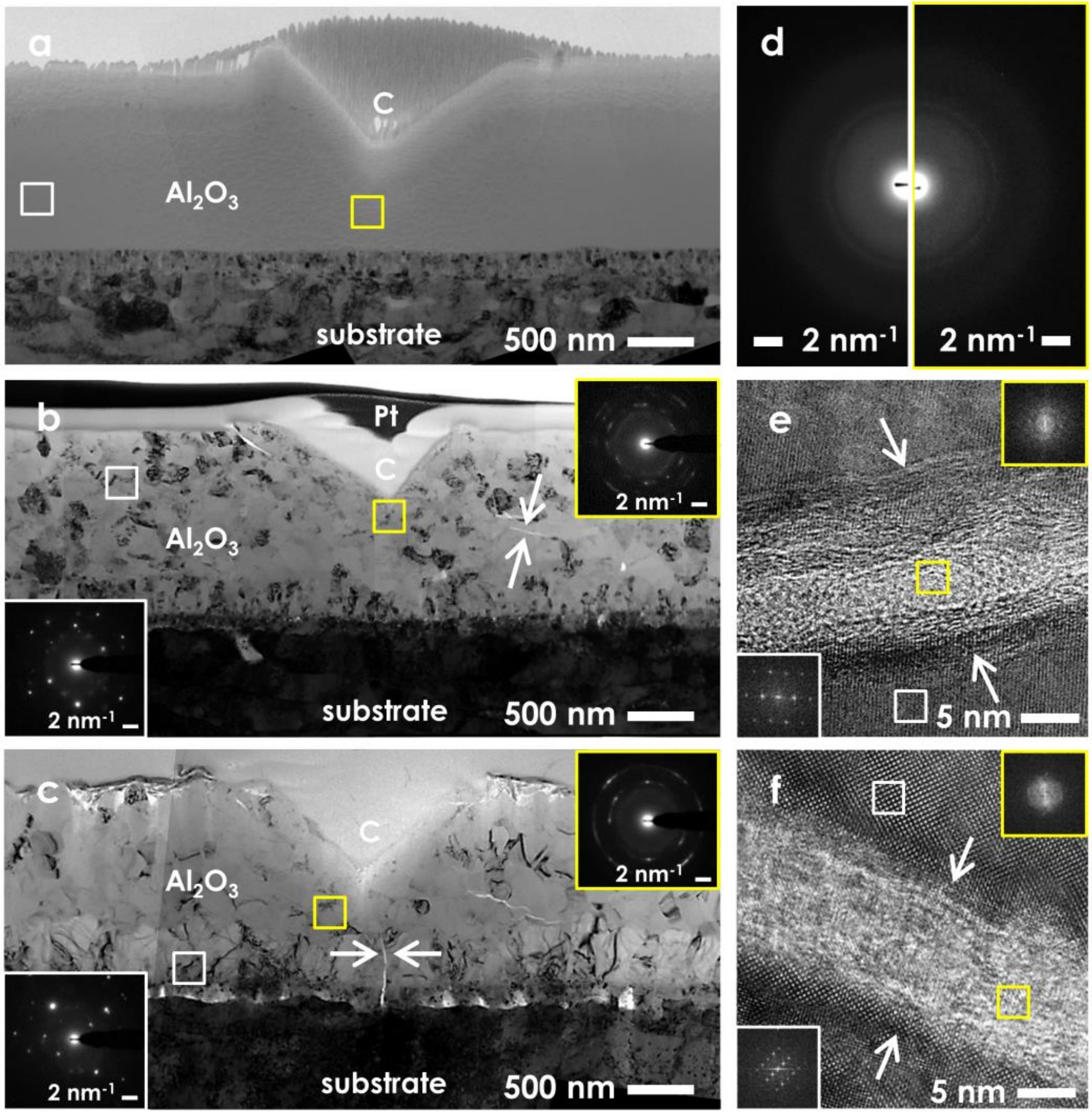

Figure 7-15: Cross-sectional TEM micrographs of representative nanoimpact imprints on the Al_2O_3 nanoceramic thin films (a) before and after irradiation up to (b) 20 dpa and (c) 150 dpa. No major structural rearrangements are induced by impact loading in the unirradiated samples, as confirmed by the identical SADPs gathered (d) distant from and below the impact indent. The appearance of arcs and rings in the SADPs beneath the impact zones in the irradiated samples is due to energy dissipation through bending of the lattice planes. Another energy dissipation mode at play is localized amorphization, which is indicated by arrows in (b and c), and shown in high-resolution in (e and f). The FFT insets in (e and f) confirm that the bright contrast corresponds to the amorphous phase, and that the dark contrast corresponds to the crystalline phase.

The appearance of arcs and rings in the SADPs beneath the impact zones is due to the bending of lattice planes, which denotes plastic strain as one of the main energy dissipation mechanisms. Another energy dissipation mechanism present is localized amorphization. Notably, crystalline-to-amorphous phase transitions are often described as toughening mechanisms [9]. The HR-TEM micrographs in figures **Figure 7-15** (e) and **Figure 7-15** (f) show the localized amorphization indicated by arrows in **Figure 7-15** (b) and **Figure 7-15** (c), respectively. The FFT insets show a diffused halo where the contrast is bright, and diffraction spots where the contrast is dark, confirming the amorphous nature of the bright contrast band, and the long-range order of the contiguous zone. The close alignment of the crystal lattice on either side of the amorphous band rules out the formation and subsequent rebonding of two cracked surfaces. Localized amorphization has been observed in sapphire [229] and in other unirradiated ceramics exposed to shock loading, such as B_4C [230,231], SiO_2 [232], $Y_2Si_2O_7$ [233] or B_6O [234]. The onset of the phenomenon has been explained by shock-induced plastic waves [229] and shear instability [231,232]. These phenomena are relevant at the extremely high stresses and strain rates induced by shock loading. Other mechanisms include the coalescence of dislocation loops under high shear stresses, as would occur under quasi-static mechanical load [233,234], and by adiabatic shear, which is governed by elastic strain energy in brittle solids [235]. Arguably, both the high strain rate induced by impact loading and the coalescence of defects and defect clusters formed during irradiation may play an important role in the amorphization process observed here. However, the impact speed in this study ($\approx$ 500 µm/s) is several orders of magnitude lower than the impact speed in shock loading experiments ($\approx$18 km/s) [229–232]. This fact suggests that shock-induced plastic waves and shear instability are unlikely as the main driving forces. It is worth noting that the utility of oxide nanoceramics as radiation tolerant materials is often thought to be limited by grain growth. Indeed, GBs are usually considered as the actual source of *radiation tolerance* due to their efficient behavior as defect sinks. The problem is that the density of GBs decreases inexorably as grain growth proceeds. Thus, the radiation tolerance of oxide nanoceramics is expected to fade away for increasing radiation damage exposures. However, radiation tolerance can be defined in many ways. For example, radiation tolerance can also be conceived in terms of the expected lifecycle of a given component. From this stand-point, nanoceramic thin films can be utilized as radiation tolerant coatings. In fact, the thin films in this work are able to withstand radiation damage up to 150 dpa without suffering catastrophic failure or delamination. It is also worth noting here that coarse-grained polycrystalline α-Al_2O_3 suffers void swelling and releases the resulting stresses through cracking at much lower damage exposures [236,237].

In conclusion, the results of this work may be extended to other amorphous or nanoceramic oxides in bulk or thin film form, or even to other compounds. First, it is well-established that radiation-induced crystallization occurs in a range of amorphous compounds, not just in Al_2O_3. For example, radiation-induced crystallization has been reported for InP and InAs seminconductors [238] and $MgAl_2O_4$ spinel [239]. The onset of crystallization in such compounds (and perhaps in Al_2O_3, as well) is given by a tradeoff between temperature, dose and dose rate [238]. Second, the transformation of an amorphous compound into a nanocrystalline material should always make new energy dissipation mechanisms available, such as twinning or grain rotation, among others. The specific mechanisms are likely material-dependent. Third, radiation-induced grain growth is commonly observed in bulk oxide nanoceramics, in ceramics other than oxides, and in metals [240]. Since the Hall-Petch relationship describes a fundamental effect that holds for a wide variety of materials, we expect that grain growth should generally be accompanied by an initial increase of hardness according to the inverse Hall-Petch effect. This stage should be followed by Hall-Petch softening for grain sizes above the strongest grain size. Because the strongest grain size is usually rather low (in the range 10-20 nm), it is reasonable to expect for Hall-Petch softening effect to take hold at low radiation damage levels. This effect may be influenced by the presence of radiation-induced point defects and defect clusters, depending on the material under consideration. Last, but not least, the effect of high radiation damage levels may vary depending on the class of material considered, making it unreasonable to directly extrapolate our findings to other classes of materials exposed to extended irradiations.

CHAPTER 8

Conclusions

This thesis has focused on radiation effects in interfaces and thin films of materials of interest to nuclear reactors. Research in recent years has shown that one of the most effective approaches for developing radiation damage resistant materials is to increase areal fraction of internal interfaces. A practical example of this approach are ODS steels and NFAs, where nanoscale oxide precipitate particles, in addition to imparting high temperature creep strength, also confer higher radiation damage resistance due the interfaces between the oxide nanoparticles and the surrounding ferritic matrix. The efficacy of these nanoparticles to act as sinks to radiation damage defects relies on the compositional and morphological stability of the interfaces between the nanoparticles and the matrix, under radiation. Knowledge of the fundamental response of this metal/oxide interface to radiation is of utmost importance to predict the in-service behavior of these alloys. Studying irradiation effects at the interfaces of thin film-substrate systems provides for a more fundamental understanding than for example studying irradiation effects in very fine nanoparticles embedded in a multi-component system such as ODS steels where substrate effects can often complicate the fundamental understanding of these effects.

Several films and film substrate effects were investigated in this study. First, film-substrate interface mixing effects in titanium and titanium dioxide thin films deposited on Fe-

12%Cr alloy substrate after 5 MeV Ni^{2+} ion irradiations at 300˚C and 500˚C were investigated at nanometer length scales by using STEM-EDS, TEM and XRD techniques. Radiation-induced effects were isolated from purely thermal effects by also examining regions of samples that were not irradiated but experienced the same thermal history. High temperature exposure and irradiation clearly showed the metal/oxide system to be more resistant to intermixing than the metal/metal system. The titanium dioxide film initially grew as amorphous phase, and upon exposure at 300˚C transformed to TiO_2-anatase. After exposure at 500˚C, at least two different phases are observed to form in the film: TiO_2 anatase and a sub-stoichiometric form of TiO_{2-x}. Chromium was observed to diffuse from the substrate to the sub-stoichiometric oxide phase of the film, but not into the anatase phase. Moreover, radiation promoted the formation of sub-stoichiometric phases of titanium dioxide (Ti_2O_3). Thus the stoichiometry of the film influenced the diffusion of elements such as Cr, whose spatial distribution in the material may affect corrosion resistance and promote the formation of embrittling phases.

Film-substrate interface mixing effects were also investigated in Y_2O_3 thin films deposited on Fe-12%Cr alloy substrates and irradiated with 5 MeV Ni^{2+} ion at 300˚C, 500˚C and 700˚C. TEM in-situ annealing was also performed to study the evolution of the system during the initial stages of thermal exposure. It was observed that high temperature exposure causes diffusion of chromium to the metal/oxide interface, and diffusion of iron into the film. Irradiation promoted the formation of an amorphous layer at the metal/oxide interface and grain growth in the Y_2O_3 film. Both chromium diffusion to the metal/oxide interface and amorphization at the interface after irradiation have the potential impact the in-service performance of ODS steels particularly in regards to mechanical properties, corrosion resistance, and radiation sink effect.

Since embrittlement due the formation of helium from transmutations is known to cause embrittlement, the role of interfaces as sink for helium accumulation was investigated. For this study, Y_2O_3/Fe interfaces in various crystallographic orientations were synthesized by a combination of PLD and MBE techniques and implanted with helium. High resolution TEM studies clearly revealed a greater abundance of helium bubbles at the interfaces. A statistical analysis of the bubbles did not show significant differences in bubble size for various crystallographic orientations and incoherent interfaces. Moreover, bubbles were observed to nucleate at random locations at the interface, and not in specific sites such as misfit dislocations, which the theory predicts to be preferential nucleation sites. Finally, bubbles nucleating at the interface were observed to nucleate from the oxide side and only wet the interface, never growing across this boundary. This is due to the different surface energies of the two material films, and confirms the intrinsically different character of these interfaces, as compared from example to grain boundaries of Fe, where bubbles were seen to overlap across the boundary. This observation provides another confirmation that oxide nano particles in ODS steels can act as sinks for helium accumulation.

Finally, the radiation response of thin films of Al_2O_3 was investigated in detail. The as-deposited film in this case was amorphous. Initially, irradiation induced an amorphous-to-crystalline transformation resulting in a fully nanograined structure, while extended irradiations induced grain growth and softening in accordance with the Hall-Petch relationship. The initial increase in the hardness to Young’s modulus (H/E) ratio suggests a potential improvement in the fracture toughness of the irradiated thin films, which therefore benefits from the radiation environment. The application of a load to the films resulted in a stress-induced phase transformation from crystalline to amorphous phase and a concomitant improvement in fracture toughness. Overall the findings in this work point to the potential of nanoceramic materials as coatings for high radiation field in core components for corrosion resistance.

Bibliography

[1] UN, Concise Report on the World Population Situation in 2014, A Consise (2014) 30.

[2] world energy outlook 2014, (2014). http://www.iea.org/W/bookshop/477-World_Energy_Outlook_2014.

[3] J. Cook, D. Nuccitelli, S.A. Green, M. Richardson, B. Winkler, R. Painting, R. Way, P. Jacobs, A. Skuce, Quantifying the consensus on anthropogenic global warming in the scientific literature, Environ. Res. Lett. 8 (2013) 24024. doi:10.1088/1748-9326/8/2/024024.

[4] K. Caldeira, K. Emanuel, J. Hansen, T. Wigley, Top climate change scientists' letter to policy influencers, CNN. (2013). http://edition.cnn.com/2013/11/03/world/nuclear-energy-climate-change-scientists-letter/.

[5] S.J. Zinkle, G.S. Was, Materials challenges in nuclear energy, Acta Mater. 61 (2013) 735–758. doi:10.1016/j.actamat.2012.11.004.

[6] K. Kleiner, Nuclear energy: assessing the emissions, Nat. Reports Clim. Chang. 2 (2008) 130–131. doi:10.1038/climate.2008.99.

[7] OECD Nuclear Energy Agency, A Technology Roadmap Update for Generation IV Nuclear Energy Systems, (2014) 1–66. https://www.gen-4.org/gif/upload/docs/application/pdf/2014-03/gif-tru2014.pdf.

[8] GIF, GIF R&D Outlook for Generation IV Nuclear Energy, Nucl. Energy. (2010).

[9] R.W. Grimes, R.J.M. Konings, L. Edwards, Greater tolerance for nuclear materials, Nat. Mater. 7 (2008) 683.

[10] D. Feron, Nuclear Corrosion Science and Engineering, Woodhead Publishing Ltd, Oxford, 2012.

[11] Y. Guerin, G.S. Was, S.J. Zinkle, Materials challenges for advanced nuclear energy systems, MRS Bull. 34 (2009) 10–14.

[12] W. Xu, Y. Zhang, G. Change, W. Jian, P.C. Millett, C.C. Koch, S.N. Mathaudhu, Y. Zhu, In-situ atomic-scale observation of irradiation-induced void formation, Nat. Commun. 4 (2013) 1–6.

[13] G.S. Was, Fundamentals of Radiation Materials Science: Metals and Alloys, New York, 2007.

[14] L. Hsiung, M. Fluss, S. Tumey, J. Kuntz, B. El-Dasher, M. Wall, B. Choi, A. Kimura, F. Willaime, Y. Serruys, HRTEM study of oxide nanoparticles in K3-ODS ferritic steel developed for radiation tolerance, J. Nucl. Mater. 409 (2011) 72–79. doi:10.1016/j.jnucmat.2010.09.014.

[15] F. García Ferré, M. Ormellese, F. Di Fonzo, M.G. Beghi, Advanced Al2O3 coatings for high temperature operation of steels in heavy liquid metals: A preliminary study, Corros. Sci. 77 (2013) 375–378. doi:10.1016/j.corsci.2013.07.039.

[16] G.R. Odette, M.J. Alinger, B.D. Wirth, Recent Developments in Irradiation-Resistant Steels, Annu. Rev. Mater. Res. 38 (2008) 471–503. doi:10.1146/annurev.matsci.38.060407.130315.

[17] R.E. Stoller, G.R. Odette, B.D. Wirth, Primary damage formation in bcc iron, J. Nucl. Mater. 251 (1997) 49–60. doi:10.1016/S0022-3115(97)00256-0.

[18] D.R. Olander, Fundamental aspects of nuclear reactor fuel elements : prepared for the Division of Reactor Development and Demonstration, Energy Research and Development Administration, 1976.

[19] J.F. Ziegler, J. Biersack, U. Littmark, The Stopping and Range of Ions in Matter, Pergamon Press, New York, 1985.

[20] R.E. Stoller, M.B. Toloczko, G.S. Was, A.G. Certain, S. Dwaraknath, F.A. Garner, On the use of SRIM for computing radiation damage exposure, Nucl. Instruments Methods Phys. Res. Sect. B Beam Interact. with Mater. Atoms. 310 (2013) 75–80. doi:10.1016/j.nimb.2013.05.008.

[21] S. Matteson, B.M. Paine, M.G. Grimaldi, G. Mezey, M.-A. Nicolet, Ion beam mixing in amorphous silicon I. Experimental investigation, Nucl. Instruments Methods. 182–183 (1981) 43–51. doi:10.1016/0029-554X(81)90669-8.

[22] M. Nastasi, J.W. Mayer, Ion beam mixing in metallic and semiconductor materials, Mater. Sci. Eng. R Reports. 12 (1994) 1–52. doi:10.1016/0927-796X(94)90005-1.

[23] S.E. Matteson, M.-A. Nicolet, Principles of Ion Mixing, in: MRS Online Proceeding Libr., 1980.

[24] B.M. Paine, M.-A. Nicolet, R.G. Newcombe, D.A. Thompson, Comparison of ion beam mixing at room temperature and 40 K, Nucl. Instruments Methods. 182–183 (1981) 115–119. doi:10.1016/0029-554X(81)90678-9.

[25] P.G. Shewmon, Diffusion in Solids, New York, 1963.

[26] H. Westendorp, Z.-L. Wang, F.W. Saris, Ion beam mixing of Cu□Au and Cu□W systems, Nucl. Instruments Methods Phys. Res. 194 (1982) 453–456. doi:10.1016/0029-554X(82)90563-8.

[27] Rossum, Amorphization of thin multilayer films by ion mixing and solid state reaction, in: Ion Implant. Ion Beam Process. Mater., Materials Research Society symposium proceedings, Boston, 1984: pp. 127–132.

[28] W.L. Johnson, Y.T. Cheng, M. Van Rossum, M.-A. Nicolet, When is thermodynamics relevant to ion-induced atomic rearrangements in metals?, Nucl. Instruments Methods Phys. Res. Sect. B Beam Interact. with Mater. Atoms. 7–8 (1985) 657–665. doi:10.1016/0168-583X(85)90450-1.

[29] R.A. Swalin, Thermodynamics of Solids, New York, 1972.

[30] R.S. Averback, D. Peak, L.J. Thompson, Ion-beam mixing in pure and in immiscible copper bilayer systems, Appl. Phys. A Solids Surfaces. 39 (1986) 59–64. doi:10.1007/BF01177164.

[31] Y.-T. Cheng, M. Van Rossum, M.-A. Nicolet, W.L. Johnson, Influence of chemical driving forces in ion mixing of metallic bilayers, Appl. Phys. Lett. 45 (1984) 185–187.

[32] H.H. Anderson, The Depth Resolution of Sputter Profiling, Appl. Phys. 18 (1979) 131.

[33] M. Van Rossum, Y.-T. Cheng, M.-A. Nicolet, W.L. Johnson, Correlation between cohesive energy and mixing rate in ion mixing of metallic bilayers, Appl. Phys. Lett. 46 (1985) 610. doi:10.1063/1.95557.

[34] S. Matteson, J. Roth, M. Nicolet, No Title, Radiat. Eff. 42 (1979) 217.

[35] Y.-T. Cheng, X.-A. Zhao, T. Banwell, T.W. Workman, M.-A. Nicolet, W.L. Johnson, Correlation between the cohesive energy and the onset of radiation-enhanced diffusion in ion mixing, J. Appl. Phys. 60 (1986) 2615–2617.

[36] S.J. Zinkle, L.L. Snead, Designing Radiation Resistance in Materials for Fusion Energy, Annu. Rev. Mater. Res. 44 (2014) 241–267. doi:10.1146/annurev-matsci-070813-113627.

[37] S.J. Zinkle, Radiation-induced effects on microstructure, Elsevier, 2012. doi:10.1016/B978-0-08-056033-5.00003-3.

[38] A.F. Rowcliffe, J.P. Robertson, R.L. Klueh, K. Shiba, D.J. Alexander, M.L. Grossbeck, S. Jitsukawa, Fracture toughness and tensile behavior of ferritic–martensitic steels irradiated at low temperatures, J. Nucl. Mater. 258–263 (1998) 1275–1279. doi:10.1016/S0022-3115(98)00163-9.

[39] J.E. Pawel, A.F. Rowcliffe, D.J. Alexander, M.L. Grossbeck, K. Shiba, Effects of low temperature neutron irradiation on deformation behavior of austenitic stainless steels, J. Nucl. Mater. 233–237 (1996) 202–206. doi:10.1016/S0022-3115(96)00218-8.

[40] M.H. Mathon, Y. de Carlan, G. Geoffroy, X. Averty, A. Alamo, C.H. de Novion, A SANS investigation of the irradiation-enhanced α–α′ phases separation in 7–12 Cr martensitic steels, J. Nucl. Mater. 312 (2003) 236–248. doi:10.1016/S0022-3115(02)01630-6.

[41] K.G. Field, B.D. Miller, H.J.M. Chichester, K. Sridharan, T.R. Allen, Relationship between lath boundary structure and radiation induced segregation in a neutron irradiated 9wt.% Cr model ferritic/martensitic steel, J. Nucl. Mater. 445 (2014) 143–148. doi:10.1016/j.jnucmat.2013.10.056.

[42] J.P. Wharry, G.S. Was, The mechanism of radiation-induced segregation in ferritic–martensitic alloys, Acta Mater. 65 (2014) 42–55. doi:10.1016/j.actamat.2013.09.049.

[43] E.E. Bloom, Mechanical Properties of Materials in Fusion Reactor First-Wall and Blanket Systems, J. Nucl. Mater. 85&86 (1979) 795–804.

[44] H. Schroeder, U. Stamm, No Title, in: N.H. Packan, R.E. Stoller, A.S. Kumar (Eds.), Eff. Radiat. Mater. 14th Int. Symp., ASTM STP, Philadelphia, 1990: pp. 223–245.

[45] H. Trinkaus, B.N. Singh, Helium accumulation in metals during irradiation - Where do we stand?, J. Nucl. Mater. 323 (2003) 229–242. doi:10.1016/j.jnucmat.2003.09.001.

[46] H. Ullmaier, The Influence of Helium on the Bulk Properties of Fusion Reactor, Nucl. Fusion. 24 (1984) 1039. http://iopscience.iop.org/0029-5515/24/8/009.

[47] K.G. Field, L.M. Barnard, C.M. Parish, J.T. Busby, D. Morgan, T.R. Allen, Dependence on grain boundary structure of radiation induced segregation in a 9wt.% Cr model ferritic/martensitic steel, J. Nucl. Mater. 435 (2013) 172–180. doi:10.1016/j.jnucmat.2012.12.026.

[48] L.K. Mansur, Theory and experimental background on dimensional changes in irradiated alloys, J. Nucl. Mater. 216 (1994) 97–123. doi:10.1016/0022-3115(94)90009-4.

[49] J. Laakmann, P. Jung, W. Uelhoff, Solubility of helium in gold, Acta Metall. 35 (1987) 2063–2069. doi:10.1016/0001-6160(87)90034-4.

[50] K. Morishita, R. Sugano, B.D. Wirth, MD and KMC modeling of the growth and shrinkage mechanisms of helium–vacancy clusters in Fe, J. Nucl. Mater. 323 (2003) 243–250. doi:10.1016/j.jnucmat.2003.08.019.

[51] D.T. Hoelzer, J. Bentley, M.K. Miller, M.K. Sokolov, T.S. Byun, M. Li, Development of High-Strength ODS Steels for Nuclear Energy Applications, (2010).

[52] G.R. Odette, P.J. Maziasz, J.A. Spitznagel, Fission-fusion correlations for swelling and microstructure in stainless steels: Effect of the helium to displacement per atom ratio, J. Nucl. Mater. 104 (1981) 1289–1303. doi:10.1016/0022-3115(82)90779-6.

[53] V.F. Sears, Kinetics of void growth in irradiated metals, J. Nucl. Mater. 39 (1971) 18–26. doi:10.1016/0022-3115(71)90179-6.

[54] E.R. Stoller, G.R. Odette, Analytical Solutions for Helium Bubble and Critical Radius Parameters Using a Hard Sphere Equations of State, J. Nucl. Mater. 131 (1985) 118–125.

[55] Y. Dai, G.R. Odette, T. Yamamoto, The effects of helium in irradiated structural alloys, Elsevier, 2012. doi:10.1016/B978-0-08-056033-5.00006-9.

[56] L.K. Mansur, E.H. Lee, Theoretical basis for unified analysis of experimental data and design of swelling-resistant alloys, J. Nucl. Mater. 179–181 (1991) 105–110. doi:10.1016/0022-3115(91)90023-Z.

[57] N. Science, Status Report on Structural Materials for Advanced Nuclear Systems, (2013).

[58] F.A. Garner, M.B. Toloczko, Irradiation creep and void swelling of austenitic stainless steels at low displacement rates in light water energy systems, J. Nucl. Mater. 251 (1997) 252–261. doi:10.1016/S0022-3115(97)00260-2.

[59] C.E. Klabunde, R.R. Coltman, Fission neutron damage rates and efficiencies in several metals, J. Nucl. Mater. 108–109 (1982) 183–193. doi:10.1016/0022-3115(82)90486-X.

[60] C.H.M. Broeders, A.Y. Konobeyev, Defect production efficiency in metals under neutron irradiation, J. Nucl. Mater. 328 (2004) 197–214. doi:10.1016/j.jnucmat.2004.05.002.

[61] D.J. Bacon, F. Gao, Y.N. Osetsky, The primary damage state in fcc, bcc and hcp metals as seen in molecular dynamics simulations, J. Nucl. Mater. 276 (2000) 1–12. doi:10.1016/S0022-3115(99)00165-8.

[62] S.J. Zinkle, Fusion materials science: Overview of challenges and recent progress, Phys. Plasmas. 12 (2005) 1–8. doi:10.1063/1.1880013.

[63] D.T. Hoelzer, J. Bentley, M.K. Miller, M.K. Sokolov, T.S. Byun, M. Li, Development of High-Strength ODS Steels for Nuclear Energy Applications, (2010).

[64] A.D. Brailsford, R. Bullough, The rate theory of swelling due to void growth in irradiated metals, J. Nucl. Mater. 44 (1972) 121–135. doi:10.1016/0022-3115(72)90091-8.

[65] R.A. Johnson, N.Q. Lam, Solute segregation in metals under irradiation, Phys. Rev. B. 13 (1976) 4364–4375. doi:10.1103/PhysRevB.13.4364.

[66] H.R. Brager, The effects of cold working and pre-irradiation heat treatment on void formation in neutron-irradiated type 316 stainless steel, J. Nucl. Mater. 57 (1975) 103–118. doi:10.1016/0022-3115(75)90184-1.

[67] G.R. Odette, D.T. Hoelzer, Irradiation-tolerant nanostructured ferritic alloys: Transforming helium from a liability to an asset, Jom. 62 (2010) 84–92. doi:10.1007/s11837-010-0144-1.

[68] C. Sun, S. Zheng, C.C. Wei, Y. Wu, L. Shao, Y. Yang, K.T. Hartwig, S.A. Maloy, S.J. Zinkle, T.R. Allen, H. Wang, X. Zhang, Superior radiation-resistant nanoengineered austenitic 304L stainless steel for applications in extreme radiation environments., Sci. Rep. 5 (2015) 7801. doi:10.1038/srep07801.

[69] X.M. Bai, A.F. Voter, R.G. Hoagland, M. Nastasi, B.P. Uberuaga, Efficient Annealing of Radiation Damage Near Grain Boundaries via Interstitial Emission, Science (80-.). 327 (2010) 1631–1634. doi:10.1126/science.1183723.

[70] B.P. Uberuaga, L.J. Vernon, E. Martinez, A.F. Voter, The relationship between grain boundary structure, defect mobility, and grain boundary sink efficiency, Sci. Rep. 5 (2015) 9095. doi:10.1038/srep09095.

[71] Y. Katoh, L.L. Snead, I. Szlufarska, W.J. Weber, Radiation effects in SiC for nuclear structural applications, Curr. Opin. Solid State Mater. Sci. 16 (2012) 143–152. doi:10.1016/j.cossms.2012.03.005.

[72] M.E. Launey, R.O. Ritchie, On the fracture toughness of advanced materials, Adv. Mater. 21 (2009) 2103–2110. doi:10.1002/adma.200803322.

[73] J. Karch, R. Birringer, H. Gleiter, Ceramics ductile at low temperature, Nature. 330 (1987)

556–558.

[74] A. Inoue, Stabilization of metallic supercooled liquid and bulk amorphous alloys, Acta Mater. 48 (2000) 279–306. doi:10.1016/S1359-6454(99)00300-6.

[75] K.L. Murty, I. Charit, Structural materials for Gen-IV nuclear reactors: Challenges and opportunities, J. Nucl. Mater. 383 (2008) 189–195. doi:10.1016/j.jnucmat.2008.08.044.

[76] S.J. Zinkle, K.A. Terrani, J.C. Gehin, L.J. Ott, L.L. Snead, Accident tolerant fuels for LWRs: A perspective, J. Nucl. Mater. 448 (2014) 374–379. doi:10.1016/j.jnucmat.2013.12.005.

[77] I.J. Beyerlein, M.J. Demkowicz, A. Misra, B.P. Uberuaga, Defect-interface interactions, Prog. Mater. Sci. 74 (2015) 125–210. doi:10.1016/j.pmatsci.2015.02.001.

[78] B. Chalmers, Some Crystal-boundary Phenomena in Metals, in: Proc. Roytal Soc. London, Royal Society of London, 1949: pp. 64–73.

[79] N. Nita, R. Schaeublin, M. Victoria, Impact of irradiation on the microstructure of nanocrystalline materials, J. Nucl. Mater. 329–333 (2004) 953–957. doi:10.1016/j.jnucmat.2004.04.058.

[80] Y. Chimi, A. Iwase, N. Ishikawa, M. Kobiyama, T. Inami, S. Okuda, Accumulation and recovery of defects in ion-irradiated nanocrystalline gold, J. Nucl. Mater. 297 (2001) 355–357. doi:10.1016/S0022-3115(01)00629-8.

[81] M. Rose, A.G. Balogh, H. Hahn, Instability of irradiation induced defects in nanostructured materials, Nucl. Instruments Methods Phys. Res. Sect. B Beam Interact. with Mater. Atoms. 127–128 (1997) 119–122. doi:10.1016/S0168-583X(96)00863-4.

[82] M. Rose, A.G. Balogh, H. Hahn, Defect formation in irradiated nanostructured materials, Mater. Sci. Forum. 248–249 (1997) 213–216. doi:10.4028/www.scientific.net/MSF.248-249.213.

[83] C. Sun, K.Y. Yu, J.H. Lee, Y. Liu, H. Wang, L. Shao, S.A. Maloy, K.T. Hartwig, X. Zhang, Enhanced radiation tolerance of ultrafine grained Fe–Cr–Ni alloy, J. Nucl. Mater. 420 (2012) 235–240. doi:10.1016/j.jnucmat.2011.10.001.

[84] X. Zhang, N. Li, O. Anderoglu, H. Wang, J.G. Swadener, T. Höchbauer, A. Misra, R.G. Hoagland, Nanostructured Cu/Nb multilayers subjected to helium ion-irradiation, Nucl. Instruments Methods Phys. Res. Sect. B Beam Interact. with Mater. Atoms. 261 (2007) 1129–1132. doi:10.1016/j.nimb.2007.03.098.

[85] A. Misra, M.J. Demkowicz, X. Zhang, R.G. Hoagland, The radiation damage tolerance of ultra-high strength nanolayered composites, Jom. 59 (2007) 62–65. doi:10.1007/s11837-007-0120-6.

[86] H. Fredriksson, U. Akerlind, Solidification and Crystallization Processing in Metals and Alloys, John Wiley & Sons, 2012.

[87] J.H. Howe, Interfaces in Materials: Atomic Structure, Thermodynamics and Kinetics of Solid-Vapor, Solid-Liquid and Solid-Solid Interfaces, Wiley, 1997.

[88] P.W. Voorhees, G.B. McFadden, W.C. Johnson, On the morphological development of second-phase particles in elastically-stressed solids, Acta Metall. Mater. 40 (1992) 2979–2992. doi:10.1016/0956-7151(92)90462-N.

[89] A. Maheshwari, A.J. Ardell, Morphological Evolution of Coherent Misfitting Precipitates in Anisotropic Elastic Media, Phys. Rev. Lett. 70 (1993) 2305–2309.

[90] S. Onaka, N. Kobayashi, T. Fujii, M. Kato, Energy analysis with a superspherical shape approximation on the spherical to cubical shape transitions of coherent precipitates in cubic materials, Mater. Sci. Eng. A. 347 (2003) 42–49. doi:10.1016/S0921-

5093(02)00559-2.

[91] N. Li, J.J. Carter, A. Misra, L. Shao, H. Wang, X. Zhang, The influence of interfaces on the formation of bubbles in He-ion-irradiated Cu/Mo nanolayers, Philos. Mag. Lett. 91 (2011).

[92] E.G. Fu, A. Misra, H. Wang, L. Shao, X. Zhang, Interface enabled defects reduction in helium ion irradiated Cu/V nanolayers, J. Nucl. Mater. 407 (2010) 178–188. doi:10.1016/j.jnucmat.2010.10.011.

[93] K. Hattar, M.J. Demkowicz, A. Misra, I.M. Robertson, R.G. Hoagland, Arrest of He bubble growth in Cu–Nb multilayer nanocomposites, Scr. Mater. 58 (2008) 541–544. doi:10.1016/j.scriptamat.2007.11.007.

[94] T. Höchbauer, A. Misra, K. Hattar, R.G. Hoagland, The Influence of Interfaces on the Storage of Ion Implanted He in Multilayered Metallic Composites, J. Appl. Phys. 98 (2005) 123516.

[95] W. Han, M.J. Demkowicz, N.A. Mara, E. Fu, S. Sinha, A.D. Rollett, Y. Wang, J.S. Carpenter, I.J. Beyerlein, A. Misra, Design of Radiation Tolerant Materials Via Interface Engineering, Adv. Mater. 25 (2013) 6975–6979. doi:10.1002/adma.201303400.

[96] M.J. Demkowicz, A. Misra, A. Caro, The role of interface structure in controlling high helium concentrations, Curr. Opin. Solid State Mater. Sci. 16 (2012) 101–108. doi:10.1016/j.cossms.2011.10.003.

[97] M. Zhernenkov, M.S. Jablin, A. Misra, M. Nastasi, Y. Wang, M.J. Demkowicz, J.K. Baldwin, J. Majewski, Trapping of implanted He at Cu/Nb interfaces measured by neutron reflectometry, Appl. Phys. Lett. 98 (2011) 96–99. doi:10.1063/1.3600642.

[98] a. Kashinath, A. Misra, M.J. Demkowicz, Stable storage of helium in nanoscale platelets at semicoherent interfaces, Phys. Rev. Lett. 110 (2013) 1–5. doi:10.1103/PhysRevLett.110.086101.

[99] I.J. Beyerlein, A. Caro, M.J. Demkowicz, N.A. Mara, A. Misra, B.P. Uberuaga, Radiation damage tolerant nanomaterials, Mater. Today. 16 (2013) 443–449. doi:10.1016/j.mattod.2013.10.019.

[100] N. Li, E.G. Fu, H. Wang, J.J. Carter, L. Shao, S.A. Maloy, A. Misra, X. Zhang, He ion irradiation damage in Fe/W nanolayer films, J. Nucl. Mater. 389 (2009) 233–238. doi:10.1016/j.jnucmat.2009.02.007.

[101] N. Li, M.S. Martin, O.A. Anderoglu, A. Misra, L. Shao, H. Wang, He ion irradiation damage in Al/Nb multilayers, J. Appl. Phys. 105 (2009) 1323522–123528.

[102] K. Barmak, K.R. Coffey, D.A. Rudman, S. Foner, Phase formation sequence for the reaction of multilayer thin films of Nb/Al, J. Appl. Phys. 67 (1990) 7313–7322.

[103] K.R. Coffey, K. Barmak, D. a. Rudman, S. Foner, Thin film reaction kinetics of niobium/aluminum multilayers, J. Appl. Phys. 72 (1992) 1341–1349. doi:10.1063/1.351744.

[104] K. Barmak, C. Michaelsen, S. Vivekanand, F. Ma, Formation of the first phase in sputter-deposited Nb/Al multilayer thin films, Philos. Mag. A. 77 (1998) 167–185.

[105] F. Ernst, Metal-oxide interfaces, Mater. Sci. Eng. R Reports. 14 (1995) 97–156. doi:10.1016/0927-796X(95)80001-8.

[106] C. Noguera, Physics and Chemistry of Oxide Surfaces, Cambridge University Press, Cambridge, 1996.

[107] J. Goniakowski, F. Finocchi, C. Noguera, Polarity of oxide surfaces and nanostructures, Reports Prog. Phys. 71 (2008) 16501. doi:10.1088/0034-4885/71/1/016501.

[108] S. Choudhury, D. Morgan, B.P. Uberuaga, Massive interfacial reconstruction at misfit dislocations in metal/oxide interfaces., Sci. Rep. 4 (2014) 6533. doi:10.1038/srep06533.

[109] E.A.A. Jarvis, E.A. Carter, R. Benedek, M. Minkoff, L. Yang, Adhesive energy and charge transfer for MgO/Cu heterophase interfaces, Phys. Rev. B. 106 (2002) 7697–7700. doi:10.1103/PhysRevB.54.7697.

[110] R. Benedek, A. Alavi, D. Seidman, L. Yang, D. Muller, C. Woodward, First principles simulation of a ceramic /Metal interface with misfit, Phys. Rev. Lett. 84 (2000) 3362–5. doi:10.1103/PhysRevLett.84.3362.

[111] E.A.A. Jarvis, E.A. Carter, An atomic perspective of a doped metal-oxide interface, J. Phys. Chem. B. 106 (2002) 7995–8004. doi:10.1021/jp0257348.

[112] Y. Xu, J. a. Aguiar, S.K. Yadav, O. Anderoglu, J.K. Baldwin, Y.Q. Wang, J. a. Valdez, a. Misra, H.M. Luo, B.P. Uberuaga, N. Li, Solute redistribution and phase stability at FeCr/TiO2−x interfaces under ion irradiation, Acta Mater. 89 (2015) 364–373. doi:10.1016/j.actamat.2015.01.071.

[113] G.S. Was, J.P. Wharry, B. Frisbie, B.D. Wirth, D. Morgan, J.D. Tucker, T.R. Allen, Assessment of radiation-induced segregation mechanisms in austenitic and ferritic–martensitic alloys, J. Nucl. Mater. 411 (2011) 41–50. doi:10.1016/j.jnucmat.2011.01.031.

[114] J.T. Busby, G.S. Was, E.A. Kenik, Isolating the effect of radiation-induced segregation in irradiation-assisted stress corrosion cracking of austenitic stainless steels, J. Nucl. Mater. 302 (2002) 20–40. doi:10.1016/S0022-3115(02)00719-5.

[115] A.J. Arderll, Radiation-Induced Solute Segregation in Alloys, in: Mater. Issues Gener. IV Syst., Springer Netherlands, 2008: pp. 285–310.

[116] T. Allen, J. Busby, M. Meyer, D. Petti, Materials challenges for nuclear systems, Mater. Today. 13 (2010) 14–23. doi:10.1016/S1369-7021(10)70220-0.

[117] S. Choudhury, J.A. Aguiar, M.J. Fluss, L.L. Hsiung, A. Misra, B.P. Uberuaga, Non-uniform Solute Segregation at Semi-Coherent Metal/Oxide Interfaces, Sci. Rep. 5 (2015) 13086. doi:10.1038/srep13086.

[118] M.M. Peng, W.S. Lai, Interaction between vacancies and the α-Fe/Y2O3 interface: A first-principles study, Nucl. Instruments Methods Phys. Res. Sect. B Beam Interact. with Mater. Atoms. 352 (2015) 67–71. doi:10.1016/j.nimb.2014.12.056.

[119] H.J.T. Ellingham, Transactions and Communications, J. Soc. Chem. Ind. 63 (1944) 5.

[120] W. Hume-Rothery, B.R. Coles, Atomic Theory for Students of Metallurgy, 5th ed., The Institute of Metals, London, 1969.

[121] M.K. Miller, C.M. Parish, H. Bei, Controlling diffusion for a self-healing radiation tolerant nanostructured ferritic alloy, J. Nucl. Mater. 462 (2014) 422–427. doi:10.1016/j.jnucmat.2014.12.048.

[122] R.S. Averback, D.N. Seidman, Energetic Displacement Cascades and Their Roles in Radiation Effects, Mater. Sci. Forum. 15–18 (n.d.) 963–984.

[123] D.N. Seidman, R.S. Averback, K. Benedek, Displacement Cascades. Dynamics and Atomic Structure, Phys. Status Solidi B. 144 (1987) 85–104.

[124] T. Okuda, M. Fujiwara, Dispersion behaviour of oxide particles in mechanically alloyed ODS steel, J. Mater. Sci. Lett. 14 (1995) 1600–1603.

[125] M.J. Alinger, G.R. Odette, D.T. Hoelzer, The development and stability of Y–Ti–O nanoclusters in mechanically alloyed Fe–Cr based ferritic alloys, J. Nucl. Mater. 329–333 (2004) 382–386. doi:10.1016/j.jnucmat.2004.04.042.

[126] S. Ukai, M. Harada, H. Okada, M. Inoue, S. Nomura, S. Shikakura, K. Asabe, T. Nishida,

M. Fujiwara, Alloying design of oxide dispersion strengthened ferritic steel for long life FBRs core materials, J. Nucl. Mater. 204 (1993) 65–73.

[127] S. Ukai, M. Fujiwara, Perspective of ODS alloys application in nuclear environments, J. Nucl. Mater. 307–311 (2002) 749–757. doi:10.1016/S0022-3115(02)01043-7.

[128] S.Y. Zhong, J. Ribis, N. Lochet, Y. de Carlan, V. Klosek, M.H. Mathon, Influence of nano-particle coherency degree on the coarsening resistivity of the nano-oxide particles of Fe–14Cr–1W ODS alloys, J. Nucl. Mater. 455 (2014) 618–623. doi:10.1016/j.jnucmat.2014.08.045.

[129] C. a. Williams, G.D.W. Smith, E. a. Marquis, The effect of Ti on the coarsening behavior of oxygen-rich nanoparticles in oxide-dispersion-strengthened steels after annealing at 1200°C, Scr. Mater. 67 (2012) 108–111. doi:10.1016/j.scriptamat.2012.03.035.

[130] T. Hayashi, P.M. Sarosi, J.H. Schneibel, M.J. Mills, Creep response and deformation processes in nanocluster-strengthened ferritic steels, Acta Mater. 56 (2008) 1407–1416. doi:10.1016/j.actamat.2007.11.038.

[131] M.C. Brandes, L. Kovarik, M.K. Miller, G.S. Daehn, M.J. Mills, Creep behavior and deformation mechanisms in a nanocluster strengthened ferritic steel, Acta Mater. 60 (2012) 1827–1839. doi:10.1016/j.actamat.2011.11.057.

[132] S. Ukai, M. Fujiwara, R.L. Klueh, P.J. Maziasz, I.S. Kim, L. Heatherly, D.T. Hoelzer, N. Hashimoto, E. a. Kenik, K. Miyahara, Tensile and creep properties of an oxide dispersion-strengthened ferritic steel, J. Nucl. Mater. 307–311 (2002) 749–757. doi:10.1016/S0022-3115(02)01046-2.

[133] M.C. Brandes, L. Kovarik, M.K. Miller, M.J. Mills, Morphology, structure, and chemistry of nanoclusters in a mechanically alloyed nanostructured ferritic steel, J. Mater. Sci. 47 (2012) 3913–3923. doi:10.1007/s10853-012-6249-x.

[134] M.A. Subramanian, G. Aravamudan, G.V. Subba Rao, Oxide pyrochlores — A review, Prog. Solid State Chem. 15 (1983) 55–143. doi:10.1016/0079-6786(83)90001-8.

[135] J.D. Ault, WelchJ.E., The Yttrium Oxide - Titanium Oxide System, Acta Crystallogr. 20 (1966) 410.

[136] W.G. Mumme, A.D. Wadsley, The structure of orthorhombic Y2TiO5, an example of mixed seven- and fivefold coordination, Acta Crystallogr. Sect. B Struct. Crystallogr. Cryst. Chem. 24 (1968) 1327–1333. doi:10.1107/S0567740868004243.

[137] N. Mizutani, Y. Tajima, M. Kato, Phase Relations in the System Y2O3-TiO2, J. Am. Ceram. Soc. (1976).

[138] P. Zhang, A. Navrotsky, B. Guo, I. Kennedy, A.N. Clark, C. Lesher, Q. Liu, Energetics of Cubic and Monoclinic Yttrium Oxide Polymorphs: Phase Transitions, Surface Enthalpies, and Stability at the Nanoscale, J. Phys. Chem. C. 112 (2008) 932–938. doi:10.1021/jp7102337.

[139] L. Yang, Y. Jiang, Y. Wu, G.R. Odette, Z. Zhou, Z. Lu, The ferrite/oxide interface and helium management in nano-structured ferritic alloys from the first principles, Acta Mater. 103 (2016) 474–482. doi:10.1016/j.actamat.2015.10.031.

[140] D.J. Larson, P.J. Maziasz, I.-S. Kim, K. Miyahara, Three-dimensional atom probe observation of nanoscale titanium-oxygen clustering in an oxide-dispersion-strengthened Fe-12Cr-3W-0.4Ti + Y2O3 ferritic alloy, Scr. Mater. 44 (2001) 359–364. doi:10.1016/S1359-6462(00)00593-5.

[141] A. Mairov, K. Sridharan, Radiation Response in ODS steels, 2016.

[142] M.J. Swenson, J.P. Wharry, The comparison of microstructure and nanocluster evolution

in proton and neutron irradiated Fe–9%Cr ODS steel to 3 dpa at 500 °C, J. Nucl. Mater. 467 (2015) 97–112. doi:10.1016/j.jnucmat.2015.09.022.

[143] A. Certain, S. Kuchibhatla, V. Shutthanandan, D.T. Hoelzer, T.R. Allen, Radiation stability of nanoclusters in nano-structured oxide dispersion strengthened (ODS) steels, J. Nucl. Mater. 434 (2013) 311–321. doi:10.1016/j.jnucmat.2012.11.021.

[144] J. He, F. Wan, K. Sridharan, T.R. Allen, A. Certain, V. Shutthanandan, Y.Q. Wu, Stability of nanoclusters in 14YWT oxide dispersion strengthened steel under heavy ion-irradiation by atom probe tomography, J. Nucl. Mater. 455 (2014) 41–45. doi:10.1016/j.jnucmat.2014.03.024.

[145] G.R. Odette, HoelzerD.T., Irradiation-tolerant nanostructured ferritic alloys.pdf, JOM. (2010).

[146] A. Hirata, T. Fujita, Y.R. Wen, J.H. Schneibel, C.T. Liu, M.W. Chen, Atomic structure of nanoclusters in oxide-dispersion-strengthened steels, Nat. Mater. 10 (2011) 922.

[147] J. Xu, C.T. Liu, M.K. Miller, H. Chen, Nanocluster-associated vacancies in nanocluster-strengthened ferritic steel as seen via positron-lifetime spectroscopy, Phys. Rev. B. 79 (2009) 20204. doi:10.1103/PhysRevB.79.020204.

[148] Z.W. Zhang, L. Yao, X.-L. Wang, M.K. Miller, Vacancy-controlled ultrastable nanoclusters in nanostructured ferritic alloys, Sci. Rep. 5 (2015) 10600. doi:10.1038/srep10600.

[149] L.M. Huisman, A.E. Carlsson, C.D. Gelatt, H. Ehrenreich, Mechanisms for Energetic Vacancy Stabilization: TiO and TiC, Phys. Rev. B. 22 (1980) 991.

[150] M.K. Miller, C.L. Fu, M. Krcmar, D.T. Hoelzer, C.T. Liu, Vacancies as a constitutive element for the design of nanocluster- strengthened ferritic steels, Front. Mater. Sci. China. 3 (2009) 9–14. doi:10.1007/s11706-009-0001-8.

[151] C.L. Fu, M. Krčmar, G.S. Painter, X.Q. Chen, Vacancy mechanism of high oxygen solubility and nucleation of stable oxygen-enriched clusters in Fe, Phys. Rev. Lett. 99 (2007) 1–4. doi:10.1103/PhysRevLett.99.225502.

[152] G. Garcés, P. Pérez, P. Adeva, Precipitation hardening of Mg–12%Ti (wt.%) synthetised by physical vapour deposition, Scr. Mater. 45 (2001) 1001–1007. doi:10.1016/S1359-6462(01)01095-8.

[153] R.J. Grylls, C.D.S. Tuck, M.H. Loretto, Strengthening of a cupronickel alloy by an ordered L12 phase, Intermetallics. 4 (1996) 567–570. doi:10.1016/0966-9795(96)00050-7.

[154] F.J. Humphreys, M. Hatherly, Recrystallization and Related Annealing Phenomena, Pergamon Press, Oxford, 1995.

[155] J. Ribis, Y. de Carlan, Interfacial strained structure and orientation relationships of the nanosized oxide particles deduced from elasticity-driven morphology in oxide dispersion strengthened materials, Acta Mater. 60 (2012) 238–252. doi:10.1016/j.actamat.2011.09.042.

[156] X. Mao, K.H. Oh, S.H. Kang, T.K. Kim, J. Jang, On the coherency of Y2Ti2O7 particles with austenitic matrix of oxide dispersion strengthened steel, Acta Mater. 89 (2015) 141–152. doi:10.1016/j.actamat.2015.01.060.

[157] M. Klimiankou, R. Lindau, A. Möslang, HRTEM Study of yttrium oxide particles in ODS steels for fusion reactor application, J. Cryst. Growth. 249 (2003) 381–387. doi:10.1016/S0022-0248(02)02134-6.

[158] M. Klimiankou, R. Lindau, A. Moslang, TEM characterization of structure and composition of nanosized ODS particles in reduced activation ferritic-martensitic steels, J.

Nucl. Mater. 329–333 (2004) 347–351. doi:10.1016/j.jnucmat.2004.04.083.

[159] P.D. Edmondson, C.M. Parish, Y. Zhang, A. Hallén, M.K. Miller, Helium bubble distributions in a nanostructured ferritic alloy, J. Nucl. Mater. 434 (2013) 210–216. doi:10.1016/j.jnucmat.2012.11.049.

[160] P.D. Edmondson, C.M. Parish, Y. Zhang, A. Hallén, M.K. Miller, Helium entrapment in a nanostructured ferritic alloy, Scr. Mater. 65 (2011) 731–734. doi:10.1016/j.scriptamat.2011.07.024.

[161] L. Yang, Y. Jiang, G. Robert Odette, T. Yamamoto, Z. Liu, Y. Liu, Trapping helium in Y2Ti2O7 compared to in matrix iron: A first principles study, J. Appl. Phys. 115 (2014) 143508. doi:10.1063/1.4871282.

[162] Y. Jin, Y. Jiang, L. Yang, G. Lan, G. Robert Odette, T. Yamamoto, J. Shang, Y. Dang, First principles assessment of helium trapping in Y2TiO5 in nano-featured ferritic alloys, J. Appl. Phys. 116 (2014) 143501. doi:10.1063/1.4897503.

[163] Y. Gan, H. Zhao, D. Hoelzer, D. Yun, Energetic Study of Helium Cluster Nucleation and Growth in 14YWT through First Principles, Materials (Basel). 9 (2016) 17. doi:10.3390/ma9010017.

[164] G.W. Wicks, No Title, Crit. Rev. Solid State Mater. Sci. 18 (1993) 239.

[165] M. Ohring, Materials Science of Thin Films Deposition and Structure, Academic Press, 2002.

[166] NEC, Negative Ion Beam Sources, (n.d.). http://www.pelletron.com/negion.htm.

[167] J.G. Gigax, E. Aydogan, T. Chen, D. Chen, L. Shao, Y. Wu, W.Y. Lo, Y. Yang, F.A. Garner, The influence of ion beam rastering on the swelling of self-ion irradiated pure iron at 450 °C, J. Nucl. Mater. 465 (2015) 343–348. doi:10.1016/j.jnucmat.2015.05.025.

[168] F.R. de Boer, W.C.M. Mattens, A.R. Miedema, A.K. Niessen, Cohesion in Metal: Transition Metal Alloys, North-Holland, Amsterdam, 1989.

[169] B.O. Hong, W. Jiang, L. Duarte, C. Leinenbach, Thermodynamic re-assessment of Fe−Ti binary system, Trans. Nonferrous Met. Soc. China. 22 (2012) 2204–2211. doi:10.1016/S1003-6326(11)61450-7.

[170] M. Kopcewicz, J. Jagielski, T. Stobiecki, Structural transformations induced in Fe/Ti multilayers by Ar- and Kr-ion irradiation, J. Phys. Condens. Matter. 17 (2005) 2149–2165. doi:10.1088/0953-8984/17/13/013.

[171] Hirvonen 1986-Microstructure of ion-bombarded Fe–Ti and Fe–Ti–C multilayered films.pdf, (n.d.).

[172] R. Brenier, T. Capra, P. Thevenard, A. Perez, M. Treilleux, J. Rivory, J. Dupuy, G. Guiraud, Fe-Ti metastable-phase formation by ion-beam mixing.pdf, Phys. Rev. B. 41 (1990) 11784–11789.

[173] M.K. Lei, Z.L. Wu, T. Chen, B.S. Cao, Microstructural evolution of Fe/Ti multilayers submitted to in situ thermal annealing, Thin Solid Films. 500 (2006) 174–179. doi:10.1016/j.tsf.2005.11.054.

[174] T. Chen, Z.L. Wu, B.S. Cao, J. Gao, M.K. Lei, Solid state reaction of Fe/Ti nanometer-scale multilayers, Surf. Coatings Technol. 201 (2007) 5059–5062. doi:10.1016/j.surfcoat.2006.07.150.

[175] K. Tanaka, M. Otsuka, Structural change of Fe/Ti multilayer during annealing in vacuum and hydrogen atmosphere, Int. J. Hydrogen Energy. 24 (1999) 891–898. doi:10.1016/S0360-3199(98)00164-5.

[176] D.A.H. Hanaor, C.C. Sorrell, Review of the anatase to rutile phase transformation, J.

Mater. Sci. 46 (2011) 855–874.

[177] K. Lin, Phase Identification Using Series of Selected Area Diffraction Patterns and Energy Dispersive Spectrometry within TEM, (2014) 57–66.

[178] E.K. Evangelou, C. Wiemer, M. Fanciulli, M. Sethu, W. Cranton, Electrical and structural characteristics of yttrium oxide films deposited by rf-magnetron sputtering on n-Si, J. Appl. Phys. 94 (2003) 318–325. doi:10.1063/1.1580644.

[179] S. Zhang, R. Xiao, Yttrium oxide films prepared by pulsed laser deposition, J. Appl. Phys. 83 (1998) 3842. doi:10.1063/1.366615.

[180] A. Mairov, K. Sridharan, Irradiation-induced Intermixing Effects at the Interfaces of Titanium and Titanium- dioxide Thin Films and Fe-12%Cr Substrate, 2016.

[181] B.X. Liu, Ion Mixing and Metallic Alloy Phase Formation, Phys. Status Solidi A. 94 (1986) 11.

[182] P.D. Edmondson, Y. Zhang, S. Moll, F. Namavar, W.J. Weber, Irradiation effects on microstructure change in nanocrystalline ceria – Phase, lattice stress, grain size and boundaries, Acta Mater. 60 (2012) 5408–5416. doi:10.1016/j.actamat.2012.07.010.

[183] D.S. Aidhy, Y. Zhang, W.J. Weber, A fast grain-growth mechanism revealed in nanocrystalline ceramic oxides, Scr. Mater. 83 (2014) 9–12. doi:10.1016/j.scriptamat.2014.03.020.

[184] Y. Zhang, D.S. Aidhy, T. Varga, S. Moll, P.D. Edmondson, F. Namavar, K. Jin, C.N. Ostrouchov, W.J. Weber, The effect of electronic energy loss on irradiation-induced grain growth in nanocrystalline oxides., Phys. Chem. Chem. Phys. (2014) 8051–8059. doi:10.1039/c4cp00392f.

[185] S. Dey, J.W. Drazin, Y. Wang, J.A. Valdez, T.G. Holesinger, B.P. Uberuaga, R.H.R. Castro, Radiation Tolerance of Nanocrystalline Ceramics: Insights from Yttria Stabilized Zirconia, Sci. Rep. 5 (2015) 7746. doi:10.1038/srep07746.

[186] F. García Ferré, A. Mairov, L. Ceseracciu, Y. Serruys, P. Trocellier, C. Baumier, O. Kaïtasov, R. Brescia, D. Gastaldi, P. Vena, M.G. Beghi, L. Beck, K. Sridharan, F. Di Fonzo, Radiation endurance in Al 2 O 3 nanoceramics, 2016.

[187] S.J. Zinkle, Effect of irradiation spectrum on the microstructural evolution in ceramic insulators, J. Nucl. Mater. 219 (1995) 113–127. doi:10.1016/0022-3115(94)00662-8.

[188] S.J. Zinkle, C. Kinoshita, Defect production in ceramics, J. Nucl. Mater. 251 (1997) 200–217. doi:10.1016/S0022-3115(97)00224-9.

[189] C.J. McHargue, Ion beam modification of ceramics, Mater. Sci. Eng. A. 253 (1998) 94–105. doi:10.1016/S0921-5093(98)00714-X.

[190] S.J. Zinkle, V.A. Skuratov, D.T. Hoelzer, On the conflicting roles of ionizing radiation in ceramics, Nucl. Instruments Methods Phys. Res. Sect. B Beam Interact. with Mater. Atoms. 191 (2002) 758–766. doi:10.1016/S0168-583X(02)00648-1.

[191] T. Stan, Y. Wu, T. Brown, C. Palmstrom, G.R. Odette, F. Allen, P. Hosemann, He IMPLANTATION OF Fe–{110}YTO BILAYERS, 2015.

[192] B. Harald, Epitaxial Growth of Thin Films, in: K. Wandelt (Ed.), Surf. Interface Sci., Wiley, 2013.

[193] R.A. Cowley, A. Bourlange, J.L. Hutchison, K.H.L. Zhang, A.M. Korsunsky, R.G. Egdell, Tilting during island growth of In2O3 on Y-stabilized ZrO2(001) revealed by high-resolution x-ray diffraction, Phys. Rev. B. 82 (2010) 165312. doi:10.1103/PhysRevB.82.165312.

[194] M.J. Demkowicz, R.G. Hoagland, J.P. Hirth, Interface Structure and Radiation Damage

Resistance in Cu-Nb Multilayer Nanocomposites, Phys. Rev. Lett. 100 (2008) 136102. doi:10.1103/PhysRevLett.100.136102.

[195] Z. Di, X.-M. Bai, Q. Wei, J. Won, R.G. Hoagland, Y. Wang, A. Misra, B.P. Uberuaga, M. Nastasi, Tunable helium bubble superlattice ordered by screw dislocation network, Phys. Rev. B. 84 (2011) 52101. doi:10.1103/PhysRevB.84.052101.

[196] S. Zheng, S. Shao, J. Zhang, Y. Wang, M.J. Demkowicz, I.J. Beyerlein, N. a. Mara, Adhesion of voids to bimetal interfaces with non-uniform energies, Sci. Rep. 5 (2015) 15428. doi:10.1038/srep15428.

[197] W.R. Tyson, W.A. Miller, Surface free energies of solid metals: Estimation from liquid surface tension measurements, Surf. Sci. 62 (1977) 267–276. doi:10.1016/0039-6028(77)90442-3.

[198] F.R. de Boer, R. Boom, W.C.M. Mattens, A.R. Miedema, A.K. Niessen, Cohesion in Metals: Transition Metals and Alloys, Elsevier, Amsterdam, 1988.

[199] L. Vitos, A.V. Ruban, H.L. Skriver, J. Kollár, The surface energy of metals, Surf. Sci. 411 (1998) 186–202. doi:10.1016/S0039-6028(98)00363-X.

[200] T. Shikama, R. Knitter, J. Konys, T. Muroga, K. Tsuchiya, A. Moesslang, H. Kawamura, S. Nagata, Status of development of functional materials with perspective on beyond-ITER, Fusion Eng. Des. 83 (2008) 976–982. doi:10.1016/j.fusengdes.2008.07.034.

[201] I.A. Ovid'Ko, A.G. Sheinerman, Nanoscale rotational deformation in solids at high stresses, Appl. Phys. Lett. 98 (2011) 2014–2017. doi:10.1063/1.3587637.

[202] I.A. Ovid'ko, Deformation of Nanostructures, Science (80-.). 295 (2002) 2386. doi:10.1126/science.1071064.

[203] M. Gutkin, I. Ovid'ko, Plastic Deformation in Nanocrystalline Materials, Springer-Verlag Berlin Heidelberg, 2004.

[204] K.Y. Yu, D. Bufford, C. Sun, Y. Liu, H. Wang, M. a Kirk, M. Li, X. Zhang, Removal of stacking-fault tetrahedra by twin boundaries in nanotwinned metals., Nat. Commun. 4 (2013) 1377. doi:10.1038/ncomms2382.

[205] D. Chen, F. Gao, B. Liu, Grain boundary resistance to amorphization of nanocrystalline silicon carbide, Sci. Rep. 5 (2015) 16602. doi:10.1038/srep16602.

[206] C. Sun, D. Bufford, Y. Chen, M. a Kirk, Y.Q. Wang, M. Li, H. Wang, S. a Maloy, X. Zhang, In situ study of defect migration kinetics in nanoporous Ag with enhanced radiation tolerance., Sci. Rep. 4 (2014) 3737. doi:10.1038/srep03737.

[207] J.A. Aguiar, P.P. Dholabhai, Z. Bi, Q. Jia, E.G. Fu, Y.Q. Wang, T. Aoki, J. Zhu, A. Misra, B.P. Uberuaga, Linking Interfacial Step Structure and Chemistry with Locally Enhanced Radiation-Induced Amorphization at Oxide Heterointerfaces, Adv. Mater. Interfaces. 1 (2015) 1300142.

[208] A. Banerjee, S. Raju, R. Divakar, E. Mohandas, G. Panneerselvam, M.P. Antony, Thermal property characterization of a titanium modified austenitic stainless steel (alloy D9), J. Nucl. Mater. 347 (2005) 20–30. doi:10.1016/j.jnucmat.2005.06.009.

[209] T.M. Pollock, D.M. Lipkin, K.J. Hemker, Multifunctional coating interlayers for thermal-barrier systems, MRS Bull. 37 (2012) 923–931. doi:10.1557/mrs.2012.238.

[210] D.R. Clarke, M. Oechsner, N.P. Padture, Thermal-barrier coatings for more efficient gas-turbine engines, MRS Bull. 37 (2012) 891–898. doi:10.1557/mrs.2012.232.

[211] E.M. Bringa, J.D. Monk, A. Caro, A. Misra, M. Duchaineau, F. Abraham, M. Nastasi, S.T. Picraux, Y.Q. Wang, D. Farkas, Are Nanoporous Materials Radiation Resistant?, (2011) 2–6.

[212] C. Cibert, H. Hidalgo, C. Champeaux, P. Tristant, C. Tixier, J. Desmaison, A. Catherinot, Properties of aluminum oxide thin films deposited by pulsed laser deposition and plasma enhanced chemical vapor deposition, Thin Solid Films. 516 (2008) 1290–1296. doi:10.1016/j.tsf.2007.05.064.

[213] L. Beck, Y. Serruys, S. Miro, P. Trocellier, E. Bordas, F. Leprêtre, D. Brimbal, T. Loussouarn, H. Martin, S. Vaubaillon, S. Pellegrino, D. Bachiller-Perea, Ion irradiation and radiation effect characterization at the JANNUS-Saclay triple beam facility, J. Mater. Res. 30 (2015) 1–12. doi:10.1557/jmr.2014.414.

[214] F. García Ferré, E. Bertarelli, A. Chiodoni, D. Carnelli, D. Gastaldi, P. Vena, M.G. Beghi, F. Di Fonzo, The mechanical properties of a nanocrystalline Al2O3/a-Al2O3 composite coating measured by nanoindentation and Brillouin spectroscopy, Acta Mater. 61 (2013) 2662–2670. doi:10.1016/j.actamat.2013.01.050.

[215] W. Mao, Y. Shen, Nanoindentation Study of Pop-in Phenomenon Characteristics and Mechanical Properties of Sapphire (101-2) Crystal, J. Am. Ceram. Soc. 95 (2012) 3605–3612.

[216] A. Leyland, A. Matthews, On the significance of the H/E ratio in wear control: a nanocomposite coating approach to optimised tribological behaviour, Wear. 246 (2000) 1–11. doi:10.1016/S0043-1648(00)00488-9.

[217] Y. Chen, K.Y. Yu, Y. Liu, S. Shao, H. Wang, M. a. Kirk, J. Wang, X. Zhang, Damage-tolerant nanotwinned metals with nanovoids under radiation environments, Nat. Commun. 6 (2015) 7036. doi:10.1038/ncomms8036.

[218] R. Nakamura, M. Ishimaru, H. Yasuda, H. Nakajima, Atomic rearrangements in amorphous Al2O3 under electron-beam irradiation, J. Appl. Phys. 113 (2013) 64312. doi:10.1063/1.4790705.

[219] N. Yu, P.C. McIntyre, M. Nastasi, K.E. Sickafus, High-quality epitaxial growth of γ-alumina films on α-alumina sapphire induced by ion-beam bombardment, Phys. Rev. B. 52 (1995) 17518–17522.

[220] Y. Sina, M. Ishimaru, C.J. McHargue, E. Alves, K.E. Sickafus, Ion beam induced epitaxial crystallization of α-Al2O3 at room temperature, Nucl. Instruments Methods Phys. Res. Sect. B Beam Interact. with Mater. Atoms. 321 (2014) 8–13. doi:10.1016/j.nimb.2013.12.012.

[221] I.A. Ovid'ko, Nanoscale multiplane shear and twin deformation in nanowires and nanocrystalline solids, Appl. Phys. Lett. 99 (2011) 61907. doi:10.1063/1.3620934.

[222] M. Chen, E. Ma, K.J. Hemker, H. Sheng, Y. Wang, X. Cheng, Deformation Twinning in Nanocrystalline Aluminum, Science (80-.). 300 (2003) 1275–1277. doi:10.1126/science.1083727.

[223] S. Veprek, Recent research for new superhard materials: go nano!, J. Vac. Sci. Technol. A 31 (2013) 50822.

[224] P. Auerkari, Mechanical and physical properties of engineering alumina ceramics, Tech. Res. Cent. Finl. (1996) 26.

[225] J.A. Wollmershauser, B.N. Feigelson, E.P. Gorzkowski, C.T. Ellis, R. Goswami, S.B. Qadri, J.G. Tischler, F.J. Kub, R.K. Everett, An extended hardness limit in bulk nanoceramics, Acta Mater. 69 (2014) 9–16. doi:10.1016/j.actamat.2014.01.030.

[226] N. Nishiyama, T. Taniguchi, H. Ohfuji, K. Yoshida, F. Wakai, B.-N. Kim, H. Yoshida, Y. Higo, A. Holzheid, O. Beermann, T. Irifune, Y. Sakka, K. Funakoshi, Transparent nanocrystalline bulk alumina obtained at 7.7GPa and 800°C, Scr. Mater. 69 (2013) 362–

365. doi:10.1016/j.scriptamat.2013.05.017.
[227] M. Kondo, M. Takahashi, T. Suzuki, K. Ishikawa, K. Hata, S. Qiu, H. Sekimoto, Metallurgical study on erosion and corrosion behaviors of steels exposed to liquid lead–bismuth flow, J. Nucl. Mater. 343 (2005) 349–359. doi:10.1016/j.jnucmat.2004.08.037.
[228] P.J. Blau, A multi-stage wear model for grid-to-rod fretting of nuclear fuel rods, Wear. 313 (2014) 89–96. doi:10.1016/j.wear.2014.02.016.
[229] C. Zhang, R.K. Kalia, A. Nakano, P. Vashishta, P.S. Branicio, Deformation mechanisms and damage in α-alumina under hypervelocity impact loading, J. Appl. Phys. 103 (2008) 83508. doi:10.1063/1.2891797.
[230] M. Chen, J.W. McCauley, K.J. Hemker, Shock-Induced Localized Amorphization in Boron Carbide, Science (80-.). 299 (2003) 1563–1566. doi:10.1126/science.1080819.
[231] K.M. Reddy, P. Liu, A. Hirata, T. Fujita, M.W. Chen, Atomic structure of amorphous shear bands in boron carbide., Nat. Commun. 4 (2013) 2483. doi:10.1038/ncomms3483.
[232] A.J. Gratz, L.D. Deloach, T.M. Clough, W.J. Nellis, Shock amorphization of crystobalite, Science (80-.). 259 (1993) 663–666.
[233] Z.J. Lin, M.J. Zhuo, Z.Q. Sun, P. Veyssière, Y.C. Zhou, Amorphization by dislocation accumulation in shear bands, Acta Mater. 57 (2009) 2851–2857. doi:10.1016/j.actamat.2009.02.040.
[234] K. Madhav Reddy, A. Hirata, P. Liu, T. Fujita, T. Goto, M.W. Chen, Shear amorphization of boron suboxide, Scr. Mater. 76 (2014) 9–12. doi:10.1016/j.scriptamat.2013.12.001.
[235] D.E. Grady, Adiabatic shear failure in brittle solids, Int. J. Impact Eng. 38 (2011) 661–667. doi:10.1016/j.ijimpeng.2011.01.001.
[236] R.A. Youngman, T.E. Mitchell, F.W. Clinard, G.F. Hurley, High dose neutron irradiation damage in alpha alumina, 3 (1991).
[237] F.W. Clinard, G.F. Hurley, L.W. Hobbs, Neutron irradiation damage in MgO, Al2O3 and MgAl2O4 ceramics, J. Nucl. Mater. 108–109 (1982) 655–670. doi:10.1016/0022-3115(82)90538-4.
[238] E. Wendler, N. Dharmarasu, E. Glaser, Comparison between the reversal temperature of IBIEC–IBIIA transition and critical temperatures of damage formation in ion irradiated InP and InAs, Nucl. Instruments Methods Phys. Res. Sect. B Beam Interact. with Mater. Atoms. 160 (2000) 257–261. doi:10.1016/S0168-583X(99)00594-7.
[239] A. Chartier, T. Yamamoto, K. Yasuda, C. Meis, S. Matsumura, Frenkel pair accumulation induced crystallization of amorphous MgAl2O4, J. Nucl. Mater. 378 (2008) 188–192. doi:10.1016/j.jnucmat.2008.06.027.
[240] W. Liu, Y. Ji, P. Tan, H. Zang, C. He, D. Yun, C. Zhang, Z. Yang, Irradiation Induced Microstructure Evolution in Nanostructured Materials: A Review, Materials (Basel). 9 (2016).
[241] P. Erhart, A first-principles study of helium storage in oxides and at oxide-iron interfaces, J. Appl. Phys. 111 (2012). doi:10.1063/1.4707944.